Spring 5-2020

Quantification of Interactions between Influenza Hemagglutinin and Host Cell Phosphoinositides by Super-Resolution Microscopy

Matthew T. Parent
University of Maine, matthew.t.parent@maine.edu

QUANTIFICATION OF INTERACTIONS BETWEEN INFLUENZA HEMAGGLUTININ AND HOST CELL PHOSPHOINOSITIDES BY SUPER-RESOLUTION MICROSCOPY

By

Matthew T. Parent

B.S. University of Maine, 2011

A DISSERTATION

Submitted in Partial Fulfillment of the

Requirements for the Degree of

Doctor of Philosophy

(in Physics)

The Graduate School

The University of Maine

May 2020

Advisory Committee:

Samuel T. Hess, Professor of Physics, Advisor

R. Dean Astumian, Professor of Physics

Neil F. Comins, Professor of Physics

C. Thomas Hess, Professor of Physics

Melissa Maginnis, Assistant Professor of Microbiology

QUANTIFICATION OF INTERACTIONS BETWEEN INFLUENZA HEMAGGLUTININ AND HOST CELL PHOSPHOINOSITIDES BY SUPER-RESOLUTION MICROSCOPY

By Matthew T. Parent

Dissertation Advisor: Dr. Sam T. Hess

An Abstract of the Dissertation Presented
in Partial Fulfillment of the Requirements for the
Degree of Doctor of Philosophy
(in Physics)
May 2020

The influenza viral membrane protein hemagglutinin (HA) forms dense nanoscale clusters on host cell plasma membranes (PM), but the mechanisms that direct clustering are not well understood. Previous studies have observed HA associated with actin rich regions of the PM, but there are no known interactions between HA and actin. Phosphatidylinositol (4,5) biphosphate (PIP2), a signaling lipid in the PM, is capable of regulating the actin cytoskeleton, and HA is known to exploit actin comets, initiated by PIP2, to reach the PM of infected cells. PIP2 is also used by other viruses, such as HIV and Ebola, to form clusters of viral proteins on the PM. Using diffraction-limited and super-resolution FPALM methods, we observed that HA and PH domain, a protein marker for PIP2, are closely spatially related at the PM. Clusters of PIP2 are also significantly altered in both density and area in the presence of high levels of HA, while HA clusters are significantly altered in the presence of high levels of PIP2, suggestive of an interaction between the two.

Although HA mutates rapidly, there are 3 cysteines and 1-2 basic residues in the cytoplasmic tail domain (CTD) which remain highly conserved among HA subtypes. These cysteines are known to undergo palmitoylation in the Golgi, a post-translational modification where hydrophobic palmitic acids are attached. Using HA mutants and super-resolution FPALM, we examined the role of both palmitoylation and charge on the clustering properties of HA and spatial association with PIP2. Mutation of the cysteines or basic residues causes significant reductions to cluster densities (relative to average), while mutation of

the charges appears to modulate association with PIP2. The greatest changes were observed when both the cysteines and net charge of the HA CTD were changed, causing a maximal 22.1%±5.8% reduction in cluster radial distribution function (RDF) and a maximal 30.4%±14.6% increase in associated PH domain RDF. Cluster properties, density, perimeter, and circularity were also significantly affected. Even though clusters were not eliminated through CTD mutations, these findings suggest that the CTD of HA does play a role in the clustering of HA and spatial association with PIP2.

ACKNOWLEDGEMENTS

I'd first like to thank my advisor, Dr. Samuel Hess for his guidance, patience, optimism, and encouragement, without which this dissertation would not have been possible. I'd like to thank members of my PhD committee, Dr. Dean Astumian, Dr. Neil Comins, Dr. C. Thomas Hess, and Dr. Melissa Maginnis for their expert advice, time, and support. A special thanks to Jaqulin Wallace, who's love, kindness, and support gave me the strength to persevere. I'd like to thank the members of Hess Lab, past and present, especially Kashif Mehmood, Prakash Raut, Dr. Nikki Curthoys, Dr. Andrew Nelson, Michael Brady Butler, and Dahan Kim. I'd like to express my gratitude to Sensei Stephen Boardway and members of the martial arts community for their friendship and support throughout my time at the University of Maine. I'd also like to thank my parents, Tom and Teresa Parent, and my brothers, Carl and Brian Parent, for their continual support. Finally, I'd like to thank anyone not specifically mentioned, but through their assistance, helped me through my time at the University of Maine.

TABLE OF CONTENTS

LIST OF TABLES

LIST OF FIGURES

CHAPTER 1

INTRODUCTION

1.1. Preface

Parts of this chapter were adapted from the book chapter "Dances with Membranes: Breakthroughs from Super-resolution Imaging" by authors Nikki M. Curthoys, Matthew Parent, Michael Mlodzianoski, Andrew J. Nelson, Jennifer Lilieholm, Michael B. Butler, Matthew Valles, and Samuel T. Hess, published in Lipid Domains, Volume 75, 59–123 in May 22, 2015.

1.2. Introduction

Influenza and other enveloped RNA viruses are a continuing threat to public health. The influenza A virus (IAV), and accompanying complications from infection, are responsible for an estimated 250,000 to 500,000 deaths per year worldwide.[1,2] At risk individuals, such as young children, the elderly, or those with a weakened immune system, are at the greatest danger of mortality from the disease. Even amongst the general population, influenza causes extensive suffering and can lead to more serious secondary bacterial infections such as pneumonia. IAV in particular mutates often, leading to new strains of the virus each year, some of which are especially infectious and capable of causing nationwide epidemics, or in rare cases pandemics. One notable example was the Spanish flu pandemic of 1918, which infected an estimated 500 million people and was responsible for an estimated 40 million deaths worldwide.[3] Although influenza epidemics are infrequent, the high rate of mutation in combination with limited options for treatment makes it a question of when, not if, a new epidemic or pandemic will arise.

Current antiviral therapies are largely ineffective against many influenza strains. Since IAV mutates frequently, drug-resistant strains of the virus are increasingly common, while antiviral development takes years. Resistance to common antiviral drugs, such as amantadine and oseltamivir, has increased >90% in recent years in some IAV sub-types, illustrating the need for new drugs or alternative drug targets.[4] Some studies have shown that treatment with antiviral influenza drugs has little to no effect

on mortality or hospitalization rates for high risk individuals, and, due to potentially severe side effects, they are not generally recommended, even for otherwise healthy individuals.[5]

Vaccines remain one of the most useful tools in preventing influenza infection, but their efficacy varies greatly. Each year, several strains of the influenza virus that are predicted to be the most prevalent in the upcoming year are formulated into a vaccine. However, mutations in IAV are often difficult to predict, and the vaccines do not confer protection against all strains of the virus. In recent history, for example, the 2014-2015 influenza vaccine underperformed considerably, imparting protection from only an estimated 19% of the most common influenza strains during this year's flu season.[6] IAV has the fastest mutation rate of the 3 classifications of influenza viruses and poses the greatest threat to humans and animals since long term immunity to the virus is not currently possible. Despite this, influenza vaccines generally do impart some limited resistance to the virus by boosting the immune system and stimulating antibody production, but treatment options after infection are very limited.

1.3. Influenza A Virus

1.3.1. Influenza Viral Life Cycle

Influenza hemagglutinin (HA) performs essential roles in the life cycle of the IAV. An IAV particle (virion) in its spherical configuration is roughly 80-100nm in diameter and enclosed in a viral envelope formed from the membrane (lipid bilayer) of a host cell.[7] IAV is also capable of forming filaments with roughly the same diameter, but which are up to several microns in length. The envelope is composed of lipid membrane taken from the host cell, and viral membrane proteins: hemagglutinin (HA), neuraminidase (NA), and the ion transport protein M2. Just inside the membrane, matrix protein (M1) forms the backbone to the virion, which encapsulates ribonucleoproteins (RNP) that house RNA polymerase complexes (which copy viral RNA) and the viral RNA (vRNA) genome, which encodes all the viral proteins.[7] Two nonstructural proteins are also present, NS1 and NS2, which interfere with the natural immune response of the host cell and assist nuclear export of the vRNA genome respectively.[8]

As a virus, IAV necessarily requires the use of cellular machinery in order to replicate itself and to infect new hosts.[7] To initiate the infection process, HA on the surface of the influenza virion binds to sialic acid receptors on the plasma membrane of a cell. With high local concentration of HA bound to the cell membrane, the entire virion enters the cytoplasm of the cell inside of an endosome (membrane enclosed compartment). Once there, the cell acidifies the interior of the endosome while M2 enables the acidification of the virion through transfer of protons from the endosome into the interior of the virion. When the pH is sufficiently low, HA undergoes a conformational change and initiates fusion with the endosomal membrane, breaking the virion apart and releasing the RNPs and other components into the cytoplasm.[7] The RNPs are transferred to the cell nucleus, where the virus uses its own viral RNA polymerases to transcribe the viral RNA into messenger RNA (mRNA). The mRNA is transferred back to the cytoplasm where it is used by ribosomes to manufacture proteins on the endoplasmic reticulum or near the nucleus. Once transcribed, membrane proteins are inserted into the membrane with the help of short signaling sequences at the N-terminus of the proteins.[7] Viral membrane proteins are thought to be packaged by the Golgi apparatus for vesicular transport to the plasma membrane, where they cluster together. M1 binds to RNPs and travels with them from the nucleus to potential sites of budding on the membrane. Once viral components assemble, membrane curvature is altered (largely by M1)[9–11] and a viral bud (a portion of intact plasma membrane which is curved outward toward the exterior of the cell) forms on the cell surface. NA cleaves the sialic acid containing receptors on the cell surface,[12] while M2 mediates final scission from the host cell membrane.[13] If all the viral components have assembled properly at the membrane, new virions are infectious and can spread the virus to nearby cells or can be expelled from the host organism through mucus or respiratory droplets to infect others.

HA clustering is necessary for efficient viral fusion and assembly.[14] HA is responsible for binding the IAV virion to sialic-acid containing receptors at the plasma membrane of cells; once binding has occurred, viruses are endocytosed into the endosome, where HA facilitates membrane fusion between

the viral and endosomal membranes. Increased rates of viral-host membrane fusion are directly correlated with increased HA expression levels and lead to increased infectivity.[15] During assembly, HA clusters may mark sites for virion components to assemble and bud. The organization of HA on the cell membrane is also very important, and HA forms high density clusters as it assembles at the plasma membrane of infected cells, even in the absence of other viral components.[16] As with HA expression levels, clustering is also correlated with increased levels of infectivity and viral budding, while diffuse HA expression results in decreases in both infectivity and budding.[14] Additionally, HA clustering may also serve another important role in the viral life cycle by signaling the release of viral RNA (vRNA) and nucleoproteins (NP) from the nucleus of the infected cell, through a pathway involving mitogen-activated protein kinase (MAPK), which is necessary for assembling new infectious virions.[17]

After translation by ribosomes, HA is trimerized and then transported to the membrane through the secretory pathway, likely via vesicular transport.[18] It has been frequently suggested that once HA reaches the membrane, clusters of homotrimers form due to inherent association with lipid rafts.[14,19–22] Lipid rafts are a proposed model of the plasma membrane hypothesizing that some areas of the membrane, titled “rafts”, are enriched in cholesterol and sphingolipids (lipids involved membrane stability and signaling) and form liquid ordered phase regions within an otherwise liquid disordered membrane.[23] Rafts are proposed to be highly variable in size (originally 10-200nm) and are proposed to serve as sites of clustering and protein organization in the plasma membrane. However, the lipid raft model does not adequately describe experimental observations for clustering of HA trimers. Studies using electron microscopy showed surprisingly minor changes in clustering when markers for lipid rafts, cholesterol and sphingolipids, were removed or reduced.[24] Single molecule examinations of HA trajectories in live cells indicate that HA trimers are mobile inside clusters, inconsistent with predictions for Lo domains.[16] Contrary to the raft model, recent experiments also indicate that HA clusters are not enriched with cholesterol or sphingolipids,[25] thus alternative mechanisms of clustering are needed.

1.3.2. Hemagglutinin Structure

The HA protein is coded for by a region of the viral RNA genome that includes 2 non coding regions, 2 packaging signals that help encapsulate the RNA into virions, and a coding region with a start and stop codon that encodes the HA protein itself.[26] Genomic viral RNA is translated into mRNA by the viruses own RNA polymerase and is then translated into protein by host cell ribosomes. Partially translated HA molecules are inserted into the ER membrane with the assistance of a translocon through recognition of a signal peptide, most likely during translation of the mRNA,[27] which is afterwards normally cleaved by a host cell peptidase, resulting in a premature HA protein, HA0. HA0 molecules then form trimers (see figure 1.1), most commonly in the ER or ER-Golgi intermediate compartment,[18,28,29] prior to their transport to the membrane. Translated HA0 molecules can be broken down into a few distinct domains: a transmembrane domain (TMD), an ectodomain, and a short cytoplasmic tail domain (CTD).

HA0 further undergoes several post translational modifications in both the ectodomain and CTD that are important to its function and infectivity. To prevent early fusion with cellular membranes, a host cell enzyme is required to activate HA by cleaving HA0 into 2 subunits: HA1, containing the sialic acid receptor binding site, and HA2, containing the fusion peptide.[30] Although no longer comprised of a single amino acid chain, HA1/HA2 subunits remain together with a disulfide bond to form the mature hemagglutinin protein. Enzymes capable of cleaving HA0 into HA1/HA2 are largely found only in bronchial cells, restricting the extent of infection to these cell types.[31–35] However, some variants of IAV are capable of replicating in a larger variety of cell types, either through mutations in the cleavage site which allow other enzymes to activate HA or by mutations in NA, possibly by enhancing recruitment of plasminogen to virion assembly sites at the plasma membrane,[30] although there is disagreement that NA is the cause of enhanced recruitment.[36] Mutations to the HA0 cleavage site can also affect the virulence of the virus in different animals, due to the relative availability of enzymes able to cleave HA0.[37]

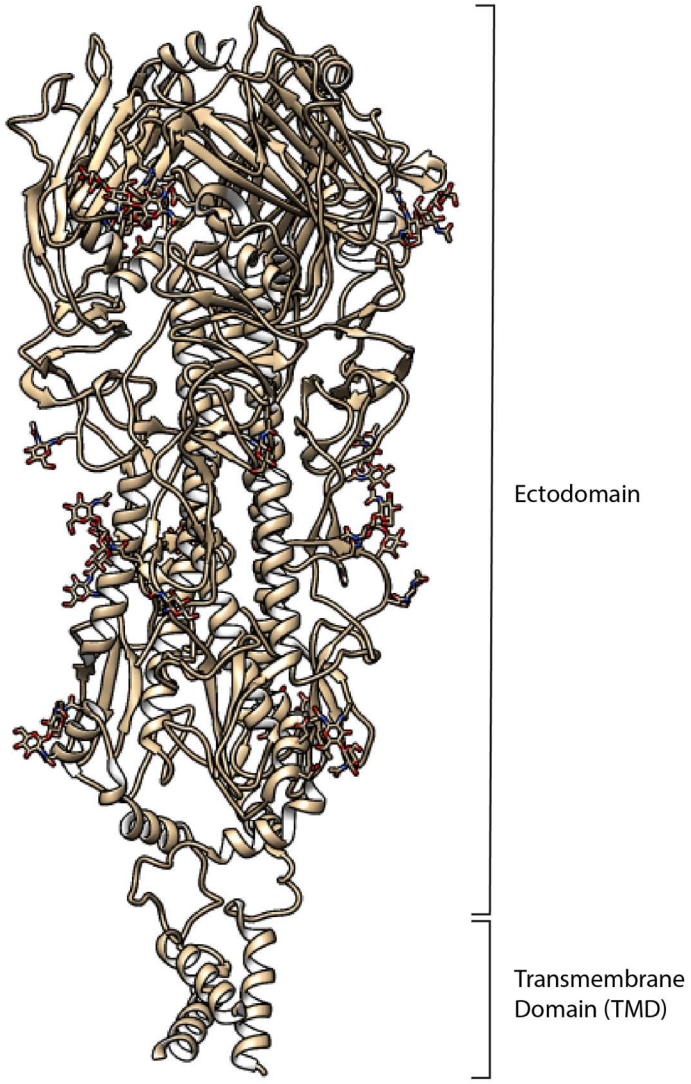

Figure 1.1: Ribbon diagram of an HA (A/duck/Alberta/35/76 [H1N1]) trimer of HA0 with tilted transmembrane region.[38] HA0 consists of an ectodomain which extends into the extracellular space, a transmembrane domain (TMD) which sits in the plasma membrane, and a cytoplasmic tail domain (CTD) (not pictured) which extends into the cytoplasm. The CTD extends into the cytoplasm of host cells and contains 3 cysteines and 1-2 basic residues which are highly conserved among HA subtypes. Protein ribbon diagram was rendered using UCSF Chimera.[39]

The CTD of HA contains 3 cysteines that remain highly conserved across influenza subtypes, which also undergo post translational modification in the Golgi[40] in the form of acylation, a process by which an acyl group is covalently bonded to the CTD of the HA molecule. In native proteins, acylation of can serve many different purposes, including regulation of membrane association and trafficking of proteins between membrane compartments.[41] In the case of influenza HA, acylation occurs primarily on cysteines, either in the cytoplasmic tail as palmitoylation (addition of a palmitate) or in the transmembrane region as palmitoylation or stearoylation (addition of a stearate).[42–44] Both palmitates and stearates contain hydrophobic regions which presumably increase the membrane affinity of the HA CTD. Acylation sites on the tail of the HA protein are known to contribute, in part, to membrane curvature,[45] while mutations to these sites can interrupt associations with M1[45,46] and alterations to the most distal acylation site can inhibit viral growth[46,47] or were found reverted after mutation in live virus.[45,48] However, it is not currently known if these are the only reasons for the highly conserved acylation of these sites.

1.4. Microscopy

1.4.1. Diffraction Limit

Due to the diffraction properties of light, even in a perfect microscope system with perfect lenses, individual fluorescent molecules will appear (in the image plane) spread out in an Airy pattern instead of as a single infinitesimal point. The spread of light from its originating point by diffraction and other distortions from imperfections in the optics can be described by the point spread function (PSF) of the system. Mathematically, the best focused image from a microscope is the convolution of the imaged object with the PSF of the optics. For a point source (delta function), the PSF of the system and the image obtained from the microscope are the same.

Any optical imaging system is fundamentally limited in resolution due to the diffraction of light. The resolving power of a microscope is often given by the Rayleigh criterion (equation 1.1),[49]

$$r_0 = \frac{0.61\lambda}{NA} \tag{1.1}$$

where r_0 is the minimum distance needed between two point-like light sources to be resolved from one another, λ is the wavelength of light detected from the sample, and NA is the numerical aperture of the objective lens of the microscope. For practical purposes, the numerical aperture of a lens is limited to ~1.45–1.65 and using the mean of the visible wavelengths of light (λ = 550 nm), the value of r_0 falls around ~200–230 nm. Although small compared to the size of a cell, this limit in resolution is substantial when compared to the sizes of proteins, viruses, and various other intracellular components.

1.4.2. Fluorescence Microscopy

The discovery and isolation of the green fluorescent protein (GFP) from the *Aequorea Victoria* jellyfish in 1962[50] opened a new avenue for investigating biological systems, although its importance as a microscopy tool was not immediately apparent. In recent years, fluorescence microscopy has been a very popular method for noninvasive and highly specific probing of biological structures and processes. With fluorescence microscopy, proteins or other molecules of interest are tagged with a fluorescent marker, either by genetically encoding a fluorescent fusion protein, employing a ligand with an attached fluorescent molecule, or by use of an antibody with an attached fluorescent marker. Genetically encoded markers tend to be the most specific of these methods, as the protein is produced inside the cell itself, and, provided the attached fluorescent protein does not interfere with the function of the native protein or its transport properties, can behave similarly to native protein.[51,52] Although somewhat less specific, antibodies and ligands are more flexible with the type of fluorescent marker that is used, since they do not require the cell to produce it from a limited set of amino acids.[53]

Confocal laser scanning microscopy (CLSM) is one of the most commonly used forms of fluorescence microscopy in the life sciences.[54] In CLSM, a fluorescently tagged sample is viewed with a microscope as a laser scans across a small (typically planar) region, causing the fluorescent markers to glow. Light emitted from the sample travels back through the microscope optics, is separated from the laser using a dichroic mirror, and then is focused through an aperture and collected by a photomultiplier

tube or other light-sensitive detector. The aperture serves to block light that is out of focus, reducing background, improving spatial resolution, and allowing for z sectioning of the sample.

Localization microscopy provides an alternative that is based on identification of individually resolvable molecules. Although individual molecules will be spread out according to the PSF, it is possible to determine, with great precision, where the originating molecule was located by fitting the PSF or its approximation (Gaussian) to recorded images of the light emitted from each molecule.[55] The precision with which such a fit can be made depends mainly on the number of photons detected from each molecule (N), the pixel size of the camera (a), the standard deviation of the PSF (s), and the background noise (b) according to equation 1.2.[55,56]

$$\langle x^2 \rangle = \frac{s^2 + a^2/12}{N} + \frac{8\pi s^4 b^2}{a^2 N^2} \qquad (1.2)$$

Electron microscopy (EM) provides an alternative to the light microscope and is capable of better than 1nm resolution while remaining "diffraction limited," because electrons with the energies used in EM have a wavelength which is much shorter than the wavelength of visible light photons. EM has been extensively applied to the study of viruses and cellular biology and is an invaluable tool for studying static structures. However, due to the harsh sample sectioning and preparation required, EM is ill-suited to imaging living specimens or exploring protein dynamics despite its impressive resolving capabilities.

1.4.3. Fluorescence Photoactivation Localization Microscopy (FPALM)

Fluorescence Photoactivation Localization Microscopy (FPALM)[57] is a form of localization microscopy which relies on the properties of certain fluorescent probes to temporally spread out the PSFs of individual molecules so that they can be resolved independently. FPALM uses a traditional inverted microscope setup, where two lasers, a readout and an activation laser, enter the microscope from the back aperture and are deflected up towards the sample by a dichroic mirror. The microscope objective collects fluorescence from the sample, which passes through a dichroic mirror and is refocused to an electron multiplying charge coupled device (EMCCD) camera.

FPALM requires the use of any manner of fluorescent label that is capable of photoactivating (transitions from a dark to a bright state), photoswitching (transitions from one color to another), or is otherwise capable of single-step fluorescence intermittency, not unlike photoactivated localization microscopy (PALM)[58] and stochastic optical reconstruction microscopy (STORM),[59] developed around the same time. The activation and readout lasers are used in concert to control the average photoactivation rate and to excite the molecules in the sample. The activation laser, at low intensity, will stochastically photoactivate (or photo-switch) a small subset of molecules (per frame) in the sample which then can absorb photons from the readout laser and get pushed into an excited state, and upon relaxation, fluoresce and emit a photon. Excitation and relaxation cycles continue until the fluorophores are irreversibly photo-bleached and are no longer capable of fluorescing. Since only a small subset of the total molecules are fluorescing at any given time, there is a high probability that, on any given camera frame, molecules will appear far enough apart to be individually resolved.

The process of activation, readout, and bleaching is repeated until a significant number of molecules from the total population have been sampled. Resolvable molecules are then background subtracted, thresholded, and fitted to a Gaussian function (equation 1.3), or another mathematical description of the PSF,[56] using a nonlinear least squares method in MATLAB to determine the center coordinates of the PSF, x and y, as well as other fitting parameters, the offset, C, and peak Gaussian amplitude, I_0.

$$I = I_0 \exp\left[-\frac{(x-x_0)^2+(y-y_0)^2}{r^2}\right] + C \qquad (1.3)$$

By fitting the PSFs to a Gaussian, molecular coordinates can be determined with a precision that is an order of magnitude better (smaller) than the diffraction limited resolution, depending mainly on the number of photons detected from the probe, the background noise, and the effective pixel size of the camera.[55] Using the coordinates of all the localized molecules, a map is then reconstructed of all the localized proteins (see figure 1.2). Since each molecule will be localized with a precision better than the

diffraction limit, and provided there is sufficient sampling of the structures present, the reconstructed protein map will have better than diffraction limited resolution. Since the resolution depends on both the localization precision (σ_{xy}) and the sampling density, or nearest neighbor distance (r_{NN}), we can approximate the resolution of the resulting images (R) according to equation 1.4.[60] or with other measures of resolution.[61,62] Median values are used for σ_{xy} and r_{NN} as an estimate for the resolution of the image as a whole.

$$R = \sqrt{\sigma_{xy}^2 + r_{NN}^2} \tag{1.4}$$

1.4.4. Multi-color FPALM

FPALM with multiple fluorescent species can be achieved by addition of several additional optics to the detection path of the standard FPALM setup, including a dichroic mirror, standard mirrors, and emission filters.[63–65] The dichroic splits the light to produce two channels on the camera that are separated by emission wavelength: a transmitted channel, or "red" channel, and a reflected, or "green" channel (based on the use of a long-pass dichroic mirror which then reflects shorter wavelengths). If the emission spectra of the fluorescent species are far enough apart, they can be separated each into their own channel. However, frequently fluorescent proteins have close or overlapping emission spectra. In these cases, emission spectra can be identified by forming an alpha ratio for each PSF, as seen in equation 1.5.[63]

$$\alpha = \frac{I_T}{I_T + I_R} \tag{1.5}$$

The alpha ratio is formed by comparing the relative amounts of transmitted, I_T, and reflected light, I_R, for each PSF after background subtraction, and provides a measure of the color for each localization. Excited fluorophores from single species tend not to emit at only a single wavelength, so a histogram of alpha ratios are typically observed for even a single molecular species;[63] careful choice of ranges of alpha values must therefore be used to separate the species. For the combination of Dendra2 (Evrogen) and

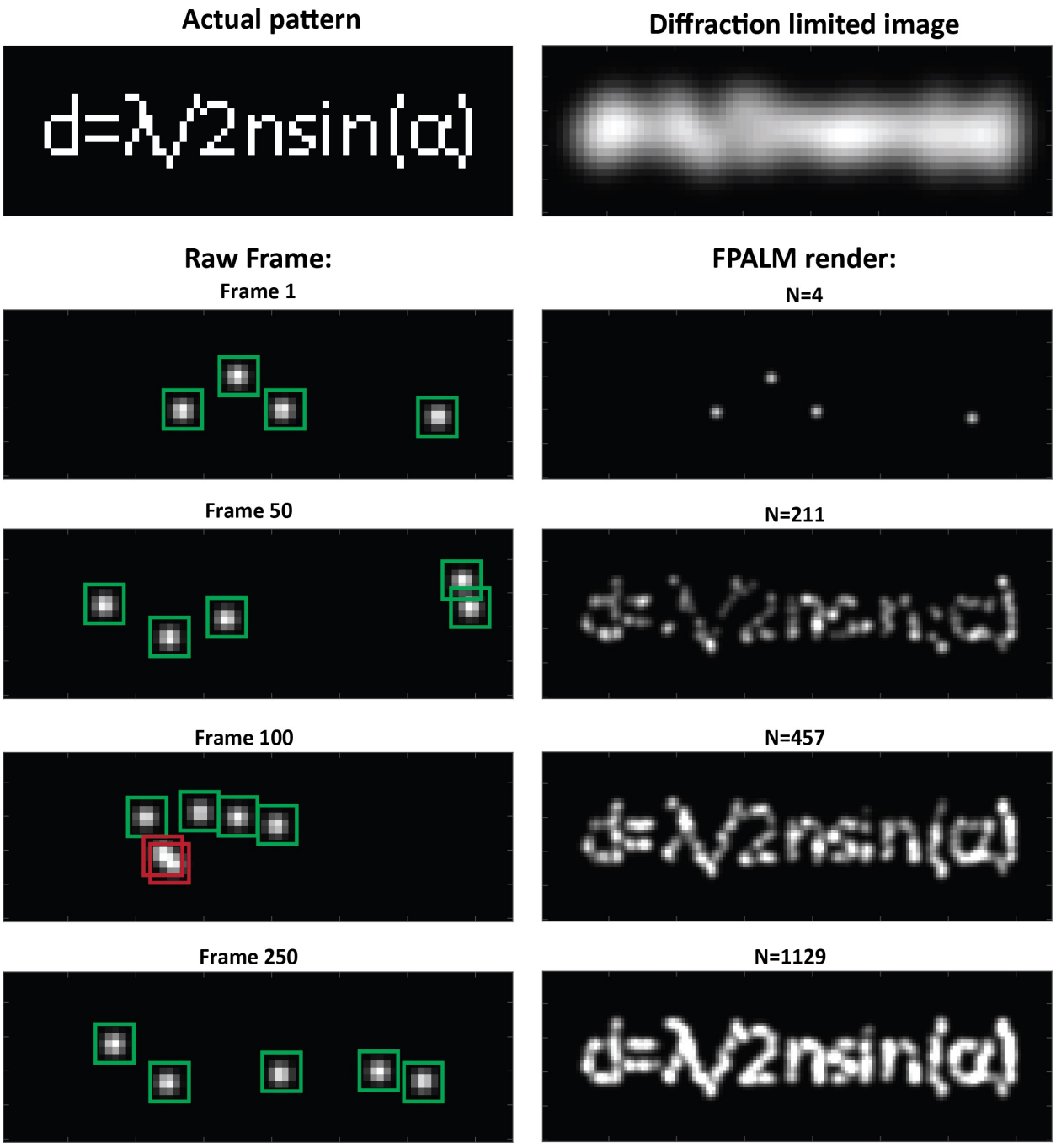

Figure 1.2: Concept of FPALM.[57] A small subset of molecules are randomly activated and readout on each frame, allowing for them to be resolved and localized independently. Once each molecule is localized, it is rendered to produce a higher resolution image than would be possible with all the fluorophores on at once. The leftmost column shows a simulation of raw PSFs with green boxes around individuals which can be resolved and localized. Sometimes PSFs will be too close together to resolve, in this case the molecules are ignored, indicated with a red box. The higher resolution FPALM render of the simulation is shown in the rightmost column, where finer details of the image are distinguishable.

PAmKate[63] fluorophores, alpha histograms appear bimodal or as wide Gaussians. Alphas are selected by examining histograms obtained from single color data and choosing bins which give an expected misidentification rate of 10% or less to minimize bleed-through from one channel into another.[63,66]

A sample of fluorescent beads fixed on a coverslip are used to calibrate and map the two channels to each other and correct for distortions stemming from imperfections in the optics. Channels are selected by hand and automated image registration is performed in MATLAB to find an optimal transformation matrix. The transformation matrix is confirmed by calculating the Pearson Correlation Coefficient (PCC)[67] between the resulting channels.

1.4.5. 3D Astigmatism FPALM

Axial and lateral positions of molecules can be obtained by the addition of a cylindrical lens to a standard FPALM setup just beyond the focal plane of the tube lens.[68] The cylindrical lens introduces an astigmatic aberration, which results in slightly different focal planes for the x and y directions. PSFs stretch or compress laterally in width (x) and height (y) dependent only on the z position of the molecule, allowing for the z coordinate to be determined explicitly. In order to precisely determine the z position, the degree of stretch in x and y needs to be related to the axial position by creating a set of calibration curves. A piezoelectric collar is attached to the microscope objective which is capable of very finely controlled (sub-nanometer precision) axial motion and a set of bright fluorescently labeled beads is taken at z positions from 0-1000nm in steps of 100nm. Beads are fitted to a two-dimensional Gaussian (equation 1.6) using a nonlinear least squares algorithm and widths and heights are determined for each z step.

$$I = I_0 \exp\left[-\frac{(x-x_0)^2}{r_x^2} - \frac{(y-y_0)^2}{r_y^2}\right] + C \qquad (1.6)$$

From this, a two plots of the Gaussian radii (one for both x and y) vs the z position are created and each are fitted with a second order polynomial to create a conversion function from r_x and r_y to z. Z positions are extrapolated by fitting measured radii to the calibration curves in a least squares way.

1.5. Actin

Actin, a cytoskeletal component of the cell, appears to be involved in the membrane organization of viral components[69–71] and specifically of influenza viral components.[72–78] Actin is a protein found in most eukaryotic cells (i.e., cells containing a nucleus) and plays a very important role in cellular motility, contraction, protein transport, signaling, and structure and forms a network of filaments that run throughout the entire cell, including near the plasma membrane.[79] Actin is found in two basic forms, globular (G-actin) and filamentous (F-actin). G-actin is diffuse throughout the cytoplasm in varying concentration and acts as the basic building block for F-actin filaments, which can be formed when G-actin monomers polymerize into long chains, either through nucleation involving formins,[80–83] actin related protein 2/3 (Arp2/3),[84,85] or tandem-monomer-binding nucleators.[86–88] Actin is regulated by a set of actin binding proteins (ABPs) that control filamentous growth and expiration. Filament polymerization can be assisted by the ABP profilin, which can sequester G-actin from the cytoplasm and assist G-actin insertion into filaments.[89] Filaments can also be depolymerized by the ABP cofilin, which either helps destabilize and eliminate filaments[90] or assists in their growth,[91] depending on the relative concentrations of actin and other ABPs nearby.[92] Higher order structures, such as filopodia and actin bundles, can be formed by linking actin filaments together with fimbrin or α-actinin.[93,94] Myosin, an actin binding motor protein, is used to transport vesicles along actin filaments,[95,96] and can organize filaments into contractile structures[97] (for a thorough review of actin and ABPs, see Pollard, 2016[98]).

Using super-resolution imaging techniques, HA clusters have been found to co-localize with actin at the membrane on a variety of length scales (50nm to >1μm).[72,73] Actin appears to restrict the motion of individual HA proteins within clusters, and actin rich regions of the membrane may provide a stable site for clustering and assembly of viral components. The actin cytoskeleton is observed to be changed by the expression of HA[99] and disruption of actin polymerization results in quantifiable changes to the structure of HA clusters (decreasing cluster densities and increasing sizes)[73] which together suggests a functional relationship between HA and actin. However, the precise link between HA and actin remains unclear.

Actin may be used by HA for transport to specific sites on the membrane suitable for clustering, HA may hijack actin after clustering to help maintain cluster stability, or HA may arrive at the membrane diffusely or in clusters, only then to become confined by actin.

Actin has also been implicated in the delivery of HA molecules to the plasma membrane through a mechanism involving rapid actin polymerization, forming actin comets.[100,101] Actin comets describe an observation whereby actin is rapidly proliferated beneath intracellular vesicles which transport proteins and lipids to the membrane. Actin comet formation could be triggered by overexpression of phosphatidylinositol phosphate 5-kinase (PI5K) or the drug pervanadate, each of which increased the synthesis of phosphatidylinositol (4,5) biphosphate (PIP2) and activation of the Wiskott–Aldrich syndrome protein (WASP) and Arp2/3.[100,101] HA-rich vesicles were observed preferentially delivered to the plasma membrane through actin comet formation, suggestive of a link between HA and PIP2,[101] while inhibition of Arp2/3 along with actin depolymerization nearly blocked HA delivery altogether.[100]

Despite the importance of HA clustering to influenza infection, the manner in which clusters form and the precise mechanism behind it is not currently known. A better understanding of HA clustering may lead to innovative drug targets and methods for treating influenza. By interrupting interactions between the host cell and the virus, it could be possible to prevent or slow IAV infection without losing efficacy when viral components mutate.

1.6. Membrane Models

Since HA trimers form dense clusters on the plasma membrane, but there are no known HA-HA trimer interactions, it seems plausible that host cell physiology may actively or passively assist in holding clusters together. As such, it is important to also understand how the membrane is organized to understand the clustering of HA. Previous observations of HA and actin colocalization and dynamics[72,73] and the modulation of phosphatidyl inositol (4,5) biphosphate (PIP2) diffusion by HA[99] are not adequately explained by current membrane models. Although published membrane models are incomplete, they

remain useful tools for understanding different aspects of membrane organization and could be further modified to more accurately match observations.

1.6.1. Singer–Nicolson Fluid Mosaic Model

The fluid mosaic model, first proposed by S.J. Singer in 1971, suggests that the cell membrane consists of a mosaic assembly of globular proteins in a phospholipid bilayer.[102,103] Such a model proposes the free lateral diffusion of proteins in the membrane with a long scale random distribution of proteins in a homogeneous lipid fluid phase bilayer. However, one important departure from this has been central to defining membrane research since the late 1970s: rather than a homogeneous distribution of proteins throughout the membrane, it was proposed that both proteins and lipids were localized to discrete patches. However, to this day it remains to be determined precisely what drives membrane heterogeneity.

In the years following the proposal of the fluid mosaic model, it was theorized that membranes were organized into discrete domains driven by lipid-protein interactions[104] and postulated that the cellular cytoskeleton could modulate the lateral diffusion of membrane molecules.[105] Glycosphingolipids (a lipid component of cell membranes) and their self-association in the Golgi could theoretically form patches with membrane proteins and then be transported to the cell membrane, mediating the sorting of lipids and proteins in polarized cells.[106,107] This heterogeneity was supported by chemical analysis of detergent resistant insoluble extractions from cell membranes containing lipid-protein complexes,[108] and led the way to new membrane models.

1.6.2. Lipid Raft Model

The lipid raft model proposes that certain subsets of lipids are able to self-arrange in the membrane form discrete structured patches, or “rafts”, on the membrane that were believed to be enriched in sphingolipids, cholesterol, and glycosylphosphatidylinositol (GPI) anchored proteins.[23] The affinity of a particular membrane protein for these lipids would determine whether or not a particular

protein was included into a raft and would determine their spatial patterning. Lipids themselves would be partitioned through weak lipid-lipid interactions between headgroups. Furthermore, cholesterol would help fill gaps between lipids to reduce water permeability.[109] Together this would result in phase separated heterogeneity in the membrane where a lipid ordered (Lo) domain (rafts) enriched in sphingolipids, cholesterol, and clusters of GPI anchored proteins and other components would "float" (move laterally as an entity) within a surrounding lipid disordered (Ld) fluid phase enriched in unsaturated lipids and non-raft proteins.[23,110] The raft model was later revised to posit that rafts are likely nanoscale in size and fluctuating, but could be stabilized in larger platforms important to signaling, viral infection, and membrane trafficking.[111] Despite this, the model depends largely on membranes to be capable of self-organizing into distinct domains driven by a specific set of lipids, cholesterol, and proteins.

Much evidence for the ability of membranes to phase separate into Lo and Ld phases was observed using artificial membranes[112–119] or giant unilamellar vesicles (GUVs)[113,115,118,120–129] with varying lipid composition, buffer conditions, and temperature. However, the ability of actual cell membranes to phase separate and form rafts under physiological conditions has not been demonstrated. In fact, influenza hemagglutinin (HA), a characteristic "raft" protein has been shown to form clusters in the absence of cholesterol and without sphingolipid enhancement, both proposed requirements for lipid rafts.[25] Additionally, GPI anchored proteins in live cell membranes have been found to not reside in, or drive the formation of, lipid ordered regions of the membrane.[130] Although membrane rafts may exist on very short timescales or short length scales, it is not clear what the physiological implications of such structures would be.

1.6.3. Lipid Shell Model

The lipid shell model theorizes that there are certain targeting motifs present within proteins that determine their inclusion into particular lipid domains, potentially through direct protein-lipid interactions.[131] The model includes the self-assembly of cholesterol-lipid complexes into which proteins

may associate through electrostatic interactions between the transmembrane domains of proteins and phospholipid headgroups. Unlike the lipid raft model, protein-lipid complexes are not thought to form a distinct lipid phase, but rather act as mobile units within a cholesterol-lipid "shell" that can diffuse throughout the membrane. However, some groups, for example caveolae and "lipid rafts", may have a Lo phase with which lipid shells may preferentially associate with depending on their lipid composition. Interactions between "shelled" proteins and those already in domains may influence their residence time within the domain.

1.6.4. Picket Fence Model

The picket fence model predicts that cytoskeletal actin filaments, in close spatial arrangement with the plasma membrane, provide barriers which compartmentalize regions of the membrane.[132,133] The actin cytoskeleton therefore acts as a "fence", which creates compartments 40-300nm in size,[134] and transmembrane proteins bound to the actin act as "pickets". Proteins are largely free to diffuse within individual compartments on short time scales, while they are required to "hop" the fence to move between adjacent compartments.[134,135] The model was later adapted to include the possibility of lipid rafts, or similar domains, which may themselves diffuse within the actin compartments as a unit.[134] Recent studies using FCS and PALM appear to support the idea that actin compartments are capable of segmenting proteins on the plasma membrane into small domains or otherwise restrict their motion.[136,137]

1.6.5. Active Composite Model

The active composite model was first proposed to explain the distribution of GPI anchored proteins in live cell membranes which were indirectly observed to exist either as monomers or in small, dense, immobile clusters.[138] Such clusters were described to be temporary and undergoing constant remodeling, but never combining to form larger domains. The ratio of monomers to clusters (4:1) was also proposed to be independent of total protein expression levels.[139] The model proposes that the plasma membrane is adjoined by a system of actin filaments arranged in "asters". Such asters would form from a

combination of actin treadmilling and myosin contraction, resulting in the barbed ends of actin filaments pointing towards the center of asters. Outlying actin filaments could then be pulled towards the denser region of asters and proteins could be pulled along with them into the centers of asters, forming nanoclusters at the cores.[140]

1.7. Moving Forward

None of the current membrane models currently proposed adequately explain observations of HA trimer clustering,[16,24,25,73,99] but actin appears to be involved.[72,73] However, there are no known interactions between actin and HA, but an intermediate may be involved which modulates this relationship. Due to the reliance of HA on PIP2 initiated actin comets for transport to the membrane, PIP2 might also be involved at the PM.[100,101] Since clusters of HA on the PM span several length scales,[16,20,24,73] some of which are diffraction limited, we aim to use FPALM[57] to examine the clustering of HA and possible functional links between the HA CTD and PIP2, as well as to explore membrane models that may better explain observations of HA clustering.

CHAPTER 2

METHODS

2.1. Biological Methods

2.1.1. Cell Culture

NIH3T3 mouse fibroblast cells (ATCC, CRL-1658) were cultured in T25 Nunc™ flasks (Thermo Scientific, 136196) in a solution of Dulbecco's Modified Eagle Medium (DMEM) (Lonza, 12-604F) supplemented to 10% calf bovine serum (ATCC, 30-2030), 100µg/mL penicillin-streptomycin (Pen-Strep) antibiotics, and phenol red and kept in an incubator at 37°C and 5% CO_2. Cells were not allowed to reach more than 80% confluency before being passaged to a new flask. Passages were performed by removing old media, prewashing with 0.05% Trypsin-EDTA solution for 30s, followed by a 10-minute incubation with 0.05% Trypsin-EDTA (Gibco, 25300054), counting using a hemocytometer, resuspension into fresh media, then seeding into a new flask at 10-15x10^4 cells. Passage numbers were kept relatively low (less than 25) to reduce adverse effects from prolonged culturing. Cell viability was upheld at >95% and tested on a semi-regular basis by exclusion staining with equal volumes of suspended cells and 0.4% trypan blue (Gibco, 15250061). Viability was determined by counting the fraction of cells that did not retain the stain.

2.1.2. Plasmids

To test the effects of palmitoylation and charge on HA cluster formation, we collaborated with Dr. Joshua Zimmerberg and Dr. Hang Waters of the Eunice Kennedy Shriver National Institute of Child Health and Human Development (NICHD/NIH) to mutate the tail of HA (X-31B, Puerto Rico/8/1934-Aichi/2/1968) with either reversals to the charge of the CTD, mutation of the palmitoylation sites to amino acids with hydrophobic sidechains, and combinations of the two. To eliminate palmitoylation of the HA CTD, cysteines at amino acid positions 555, 562, and 565 were mutated to methionine (M), alanine (A), and tyrosine (Y) respectively to produce the mutant HAMAY. Charge alterations were facilitated by mutating a positively charged arginine (R) in position 561 to glutamic acid (E) to produce HARE, or multiple arginines

in positions 561 and 557 to glutamic acid (E) and glutamine (Q) to produce HARREQ. We also tested the combination of both a charge alteration and removal of the palmitoylation sites with the mutant HAREMAY. All HA mutants were produced as fusion proteins with Dendra2 (Evrogen, green form: 490nm excitation / 553 emission peaks, red form: 507nm excitation / 573nm emission peaks), a photoswitchable fluorescent protein which is an improved version of Dendra.[141]

To image PIP2, we collaborated with Dr. Melissa Maginnis and Kashif Mehmood of the University of Maine, who produced a fusion protein of PH domain from PLC δ with PAmKate,[63] a photoactivatable red fluorescent protein (586nm excitation/628nm emission peaks),to produce PH-PAmKate. PH domain is a commonly used protein marker for PIP2.[142–146]

DH5α *E. Coli* (NEB, C2987H) containing plasmid DNA were streaked onto Agar (1g/100mL) plates and then incubated overnight at 37°C. Colonies were picked and grown in LB media overnight in a shaking incubator at 250rpm and 37°C, then isolated using a plasmid miniprep kit (Omega, D6945-01) according to the manufacturer's spin protocol. A nanodrop spectrophotometer (Thermo Scientific, ND-ONE-W) analyzed each prepared DNA sample to ensure the quality and purity of DNA. Typical 260/280 ratios between 1.7-1.9 and 260/230 ratios between 2.0-2.2 demonstrated sufficient DNA purity; concentrations <500ng/µL indicated poor yield.

2.1.3. Transient Transfection, Antibody Staining, and Fixation

For imaging experiments, cells were plated onto 35mm petri dishes with a No. 1.5 coverglass bottom (MatTek, P35G-1.5-20-C) in complete growth medium (without antibiotics and without phenol red) and seeded at a concentration of 7-8x10^4 cells/plate. After 24 hours of growth, cells were transfected using Lipofectamine 3000 (Invitrogen, L3000008) with a total of 2µg of plasmid DNA, 4µL of P3000, and 7.5µL of Lipofectamine per plate per dish. DNA was typically isolated with an Omega plasmid minikit (Omega, D6945-01). Sham control transfections were performed using only lipofectamine reagents and no DNA to assess the effects of the lipofectamine; no negative effects were observed on cell health, while

minimal background fluorescence was sometimes produced. Cells were covered with aluminum foil to prevent pre-activation of the fluorescent proteins within the incubator or by room lights and left to grow for another 24-36 hours in the incubator. After this time, cells were removed, washed with phosphate buffered saline (PBS) (Sigma-Aldrich, D8537) three times, fixed at room temperature in 4% paraformaldehyde (PFA) (Alfa Aesar, J61899AK) for 10 minutes, and then washed again with PBS three times. Additional washes with PBS were performed if residual background fluorescence from PFA was observed on the coverslip after illumination with laser light.

For antibody staining, cells were transfected, allowed to grow for 24-36 hours, and fixed as above, then washed twice with PBS and incubated with a 1:100 to 1:500 dilution of rabbit anti-HA X-31B (α-HA) antibody for 2 hours. Afterwards, the sample was washed twice with PBS and incubated with an Alexa647 anti-rabbit antibody (5μg/mL) for 2 hours and then washed again three times with PBS. As a control for the antibody stain, the same procedure was applied to cells that were not transfected with the HA plasmid, and negligible amounts of staining were observed compared to the HA transfected plates. The α-HA antibody was formed from the peptide sequence CPKYVKQNTLKLATGMRNVPEKQTR and binds amino acids 321 to 345 of the HA X-31B protein, which is at the very end of the HA1 subunit. No membrane permeabilization agents were used prior to antibody incubation in order to limit the antibody to the buffer and the outside surface of the cell.

Since NIH3T3 cells lie very flat on the surface of the coverslip, and antibodies are relatively large proteins (~10nm in size), very little antibody staining was observed at the side of the membrane in contact with the coverslip (basal surface). As such, the basal surfaces could not be imaged with the antibody in most instances.

2.2. Super-Resolution Imaging

2.2.1. 2-Color FPALM Imaging

2-color FPALM imaging was performed using the setup depicted in figure 2.1. The illumination consists of two lasers, a 558nm readout (CrystaLaser, 100mW), and a 405nm activation (CrystaLaser, 5mW), are combined using a dichroic mirror (Chroma, Z405RDC) and are focused through a lens (ThorLabs, f=350mm) at one focal length from the back aperture of the objective lens (Olympus 60x, 1.45NA oil) mounted on an inverted microscope (Olympus, IX71). The 558nm laser was operated with peak intensity 1.0kW/cm2±0.1kW/cm2 at the center of the field, and the 405nm laser was operated at low (but variable intensity), typically less than 0.02W/cm2, as measured at the sample. The activation laser passes through a half wave plate (Newport, 10RP42-1) and a linear polarizer (Newport, 5511) is used to match the polarization of the activation laser to the readout laser. Then, both lasers are passed through a quarter wave plate (Newport, 10RP54-1B) to obtain elliptical (approximately circular) polarization of the light at the sample. A quad band dichroic mirror (Semrock, Di01-R405/488/561/635) in the turret of the microscope reflects the laser light into the objective, which changes the wavefront curvature to produce nearly parallel illumination of the sample. Fluorescence from the sample is collected by the objective (i.e. an epifluorescence geometry) and passes the fluorescence back through the same dichroic, and through the microscope tube lens, which produces an intermediate image of the focal plane. The intermediate image resides at the focal point of a 2x telescope (f=400mm, f=200mm). After the telescope, the fluorescence reaches an ultra-flat dichroic (Semrock, FF580-FDi02-t3) which is aligned (at near 45°) to reflect wavelengths λ<595nm and pass λ>595 nm, splitting the light into a reflected and transmitted channel. Each channel then passes through a separate emission filter (Transmitted channel: Chroma, ET605/70m; Reflected channel: Semrock, FF01-585/40-25) before reaching an EMCCD camera (Andor, iXon 3) set to acquire at least 10,000 frames, typically at 31Hz with an EM gain of 200 for fixed samples.

An iris aperture, placed in the intermediate image plane just outside the microscope (see above), restricts the imaged region of the sample visible in each channel and ensures their spatial separation on the CCD and within acquired images. For imaging of Alexa 647 samples, a 638nm (CrystaLaser, 100mW)

was added and aligned to the 558nm and 405nm lasers and operated at 0.8kW/cm^2±0.1kW/cm^2 peak intensity at the sample.

Point spread functions were recorded in lossless stacked tiff format and then processed for localization and other data analysis using MATLAB code. The MATLAB code performs background subtraction using a rolling ball[147] or temporal median algorithm,[148] then thresholds individual frames. Pixels above the threshold are sorted by highest pixel value, and then a 7x7 area, the "grab", is selected, centered upon each high pixel. The grab is then fitted to a Gaussian (Equation 1.3) using the nlinfit function, and the fitting parameters (x position, y position, offset, radius, amplitude) and errors are all extracted. In order to reduce the number of false positives, tolerances are applied (after localization processing) to the fitting parameters for each localization. Gaussian radius, localization precision, number of photons detected, and fractional errors in the radius and Gaussian amplitude are all required to be within certain ranges; localizations that fall outside of the range for any parameter (suggesting a poor fit) are excluded from further analysis.

To screen for expression of desired fluorescently labeled molecules of interest, cells within the sample chamber were visualized first using a mercury arc lamp (Olympus, U-RFL-T) which was filtered with an emission filter (476/10). For cells transiently expressing Dendra2-HA (Zimmerberg lab, NIH), we searched for cells that were expressing moderate amounts of protein, as estimated by the brightness of the Dendra2 green form. Cells expressing very large amounts of Dendra2-HA were avoided, as these cells often displayed signs of extensive blebbing or detachment from the coverslip surface.

2.2.2. 3D FPALM Imaging

3D FPALM was conducted by using a typical FPALM setup accompanied by the addition of a cylindrical lens (f=1000mm)[68] in the detection path and a piezoelectric axial focus collar on the objective (Physik Instrumente (PI), Karlsruhe, Germany, PD72Z1x), as seen in figure 2.2. The cylindrical lens was adjusted in the detection path until the PSF was visibly stretched to approximately 10 pixels in width (in

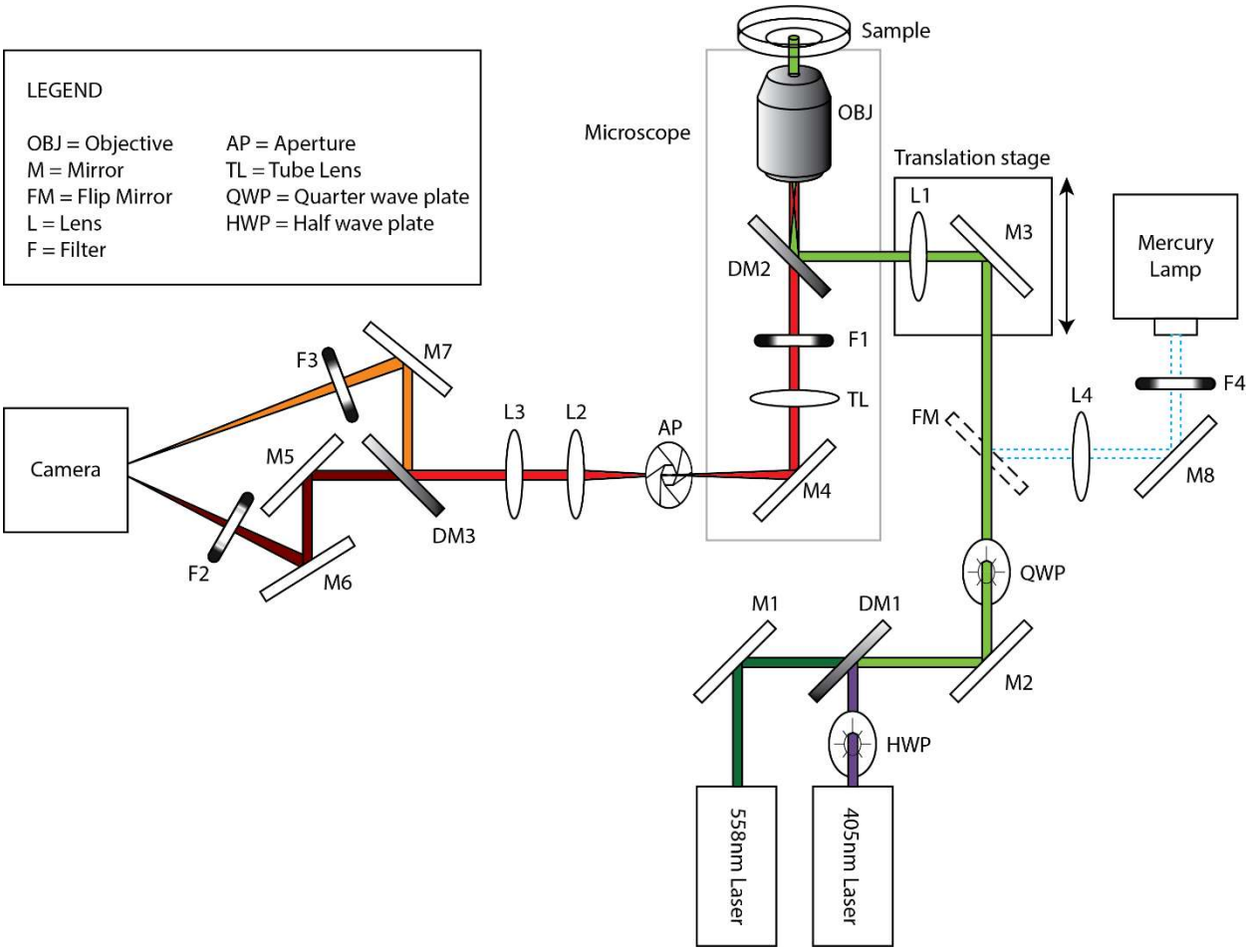

Figure 2.1: Experimental setup for multicolor FPALM. (Following methods described in Gunewardene et al[63]) On the laser path, 405nm and 558nm lasers are combined at DM1 and focused by L1 to the back focal plane of a 60X, 1.45NA objective to produce a column of light at the sample. A translation stage containing M3 and L1 can then be translated to enter a TIRF alignment. The lasers pass through a shared quarter wave plate to produce circularly polarized light at the sample. An additional half wave plate is used for the 405nm laser so that both lasers enter the quarter wave plate with similar polarizations. A flip mounted mirror is used to switch between mercury lamp and laser illumination. When the sample is excited, light is collected by the objective and passes through DM2, through an emission filter F1, and is focused by TL to the focal plane of L2. To allow more space for the 2-color optics and for additional magnification, a 2X telescope formed by L2 and L3 is placed between the microscope and the camera. From there the emitted light from the sample is split by DM3 (a 585nm long pass dichroic) to produce a "green" and a "red" channel on the camera. Additional emission filters F2 (605/70nm) and F3 (585/40nm), restrict the light from each channel to reduce background from cell autofluorescence. An aperture, placed at the focal plane of TL, restricts the size of the camera image and prevents the two channels from overlapping each other. For certain photoswitchable samples, such as Dendra2, a mercury lamp with filter F4 (488/10nm) can be temporarily added to the path using a flip mounted mirror to discriminate between cells which are well transfected for imaging. Note that the microscope box is vertically aligned (90 degrees rotated) relative to all other components.

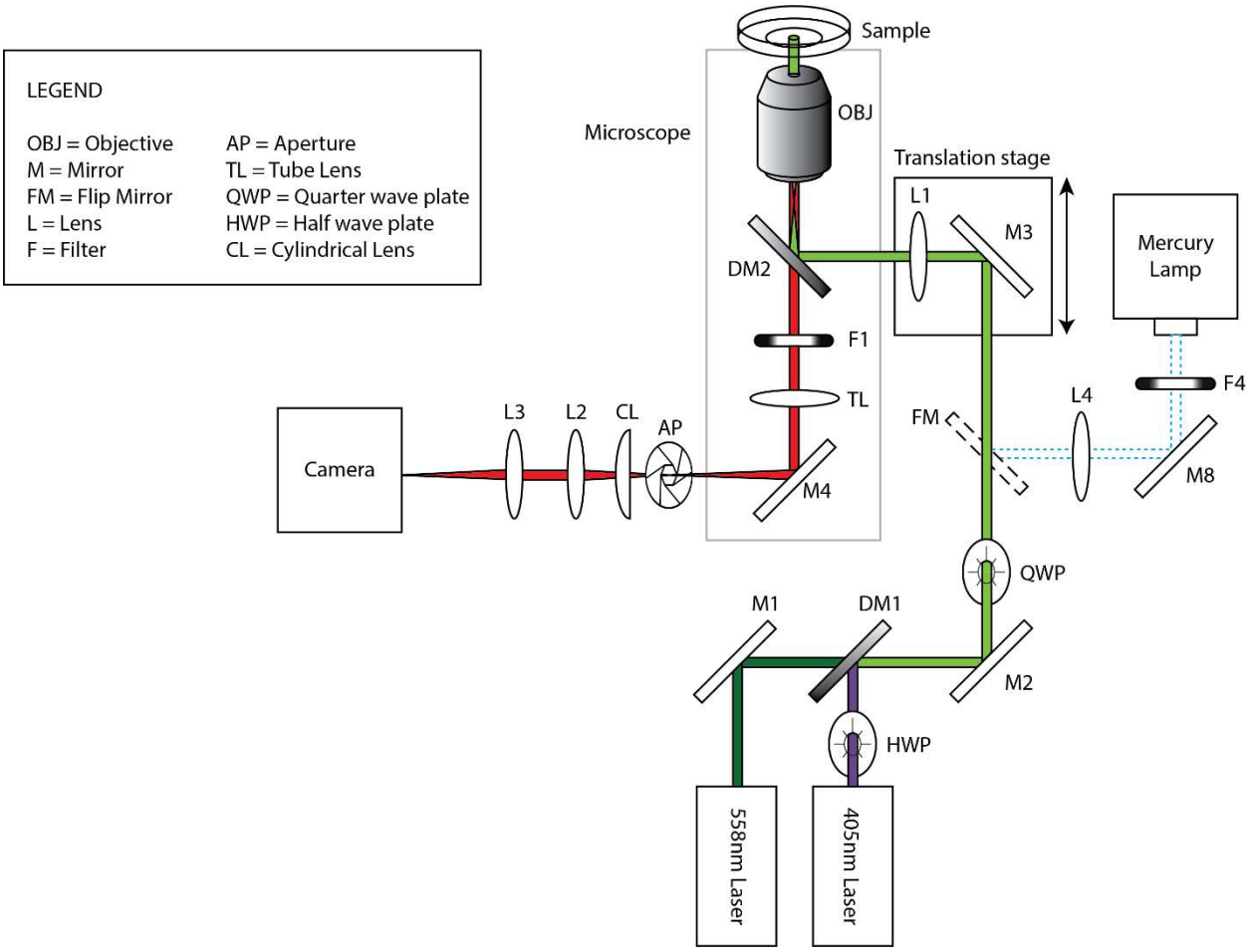

Figure 2.2: Experimental setup for 3D FPALM.[68] The addition of a cylindrical lens (CL) with a long focal length (f=1000mm) near the focal plane of the tube lens introduces an astigmatism to the PSFs collected by the objective. Due to the astigmatism, PSFs defocus asymmetrically depending on whether they are above or below the focal plane of the objective, allowing 3D information to be obtained. A piezo collar, attached to the microscope objective, is used for calibration of the 3D system. Note that the microscope box is vertically aligned (90 degrees rotated) relative to all other components.

the x and y directions) when the molecule was ±0.5µm from the in-focus plane. A sample of Tetraspeck™ fluorescent beads (Invitrogen, T7279, 0.1µm beads with 4 fluorescent dyes attached that emit between ~430nm and 680nm) were used in conjunction with the piezoelectric collar to acquire calibration image sets (typically 100 frames at 31Hz, acquired at >5 different axial positions of the objective separated by 200nm).

2.2.3. Background Estimation

Before fitting FPALM data, background subtraction is performed either through a rolling ball algorithm[147] with a radius of 6 pixels or using a temporal median filter (TMF) with a frame window of 100 frames.[148] Rolling ball background estimation can be conceptually imagined as if each pixel in a frame had a height specified by its intensity. The background is determined by "rolling" a ball underneath this, line by line, where the height the ball reaches at any given point is subtracted from the image. So long as the radius of the ball is large enough that it cannot "roll" into the PSFs, useful data will be preserved while eliminating background. Rolling ball background estimation functions best when the background changes smoothly but it fails to eliminate sharp edges or point-like background objects. Algorithmically, this is approximated by a morphological opening, which is the erosion and then dilation of the image with a circle.

TMF[148] relies on a "frame window," a set of sequential frames each separated by a fixed time step, centered temporally on a given analysis frame. Using the entire frame window, the median intensity is determined for each pixel and subtracted from the given analysis frame (i.e. as background). Unchanging features that appear bright in more than half of the frame window frames will be removed, while transiently bright PSFs remain. TMF can accurately predict the background shape but may become too aggressive when molecules appear in simultaneous frames for longer than half the frame window.

2.2.4. Laser and Camera Alignment

Samples were illuminated using a Total Internal Reflection Fluorescence (TIRF) geometry.[149] TIRF alignment begins first with a typical widefield alignment, where the laser beam is sent through the sample as a column. Microscope alignment is performed on an inverted microscope in two parts: the laser beam path and detection path. For laser path alignment, first a calibration scale is mounted to the microscope objective and the microscope condenser is used in conjunction with a mercury lamp to produce Köhler illumination, defocusing the illumination light at the sample plane. Köhler illumination is accomplished by adjusting the condenser lens until the lamp aperture is in focus and centered in the eyepiece field of view while the calibration scale is focused. Using the lamp, the scale is projected out through the back aperture of the microscope. First, the lens L1 (see figure 2.1) is removed from the laser beam path, such that the scale is projected successively along mirrors in the laser beam path and centered by adjusting the previous mirror. A piece of paper is inserted into the path, and pressed against the mirror surface, so that the scale is visible at each mirror (one mirror at a time). Once the scale is centered on all the mirrors, the readout laser is aligned with the center of the scale by adjusting the last 2 adjustable mirrors in the readout laser path, making sure that it remains centered all the way back to the back aperture of the microscope. The activation laser is then aligned to the readout laser by adjusting the last 2 mirrors in the activation laser path and minor adjustments are made to ensure that it is colinear with the readout laser.

Before completing the laser beam alignment, the detection path is aligned. The telescope is aligned by placing L2 (f=200mm) at approximately one focal distance from the focal plane of the TL to produce parallel light. L3 (f=400mm) is then placed one focal distance from the camera to refocus the image to the camera and the aperture is adjusted until in focus with the scale image in the center. For multicolor imaging, mirrors M6 and M7 may need to be moved to create equal path lengths for both detection channels (so that both channels correspond to the focal plane within the sample).

Once the detection path is aligned, the scale and objective are both removed, allowing the lasers to illuminate a spot on the ceiling. Noting carefully where the spot is located on the ceiling, the beam

expanding lens, L1, is replaced and adjusted until the laser spot is in the same location it was before the lens was inserted. The microscope objective is then placed back into the path and L1 is adjusted once more until the laser illuminates the same spot on the ceiling. To ensure that the laser is simultaneously centered in the back aperture and in the field of view, a fluorescent slide or sample of rhodamine in PBS is mounted to the objective. The laser excites a spot in the slide or rhodamine which allows the beam profile to be viewed on the camera. In order to obtain a beam that is centered in the back aperture and entering the microscope perpendicular to the objective lens, the beam profile is adjusted by "walking" the laser beam. "Walking" the laser is done by alternately adjusting L1 and M2 (vertical direction only, alternating from one mirror to the other, or horizontal direction only, alternating from one mirror to the other) until the laser spot is centered simultaneously on the ceiling above the microscope and in the fluorescent slide/rhodamine sample.

After the laser is aligned as best as possible, TIRF is accomplished by translating L1 and M3 together on a translation stage (see figure 2.1), keeping the direction of the beam parallel to the optical axis, but translating the position of the beam toward the outer edge of the objective, which causes the beam to increasingly tilt as it emerges from the objective. Once a steep enough output angle is reached, the beam undergoes total internal reflection at the boundary between the sample and the coverslip on which it is resting. Since the beam reflects entirely at the boundary, this produces an evanescent field which can excite molecules in the sample, but which does not penetrate more than a few hundred nanometers past the sample-coverslip boundary (see Axelrod, Traffic 2001[150]). As a check for TIRF, a fixed cell sample with a membrane marker may be used. The beam is tilted until the sample becomes dark, then is tilted until molecular PSFs are just visible.

2.2.5. Bleed-through Correction

Since there is non-negligible overlap of emission spectra for simultaneous imaging of certain probe combinations used (e.g. Dendra2 and PAmKate), bleed-through correction is essential for proper

separation of colors.[66] At room and physiological temperatures, far red tails on the emission spectra of most fluorescent proteins makes absolute separation of colors very difficult, even if emission maxima are well separated. Even small bleed-throughs that are unaccounted for can cause significant changes to measures of spatial correlation and density, such as Pearson Correlation Coefficients, the radial distribution function (RDF), and pair cross correlation.[66]

To correct for bleed-through, first molecules are separated into 2 species (species A and B) as best as possible using their alpha ratios (equation 1.5).[66] Localized molecules then binned onto a fine grid (here grid boxes are 20nm per side) and convolved with a 50nm Gaussian to produce spatial density plots for species A and B. Since some fraction of species A will be misidentified as species B and concurrently, some of species B will be misidentified as species A, the uncorrected value of each grid box depends on the grid boxes for each species. The uncorrected grid values for each species can be written using the following equations:

$$n_A^{Meas} = n_A^{Corr} - k_{AB} n_A^{Corr} + k_{BA} n_B^{Corr} \tag{2.1}$$

$$n_B^{Meas} = n_B^{Corr} - k_{BA} n_B^{Corr} + k_{AB} n_A^{Corr} \tag{2.2}$$

Where n_A^{Meas} and n_B^{Meas} are the uncorrected values, $n_A^{Corr}$and $n_B^{Corr}$are the bleed-through corrected values, and $k_{AB}$and k_{BA} are the rates of bleed-through from species A to species B and species B to species A respectively. Solving these as a system of equations for the corrected values, we obtain the bleed-through corrected values for each species:

$$n_A^{Corr} = \frac{n_A^{Meas} - k_{BA} n_A^{Meas} - k_{BA} n_B^{Meas}}{1 - k_{AB} - k_{BA}} \tag{2.3}$$

$$n_B^{Corr} = \frac{n_B^{Meas} - k_{AB} n_A^{Meas} - k_{AB} n_B^{Meas}}{1 - k_{AB} - k_{BA}} \tag{2.4}$$

Estimations of bleed-through rates were found by imaging single color cell samples using the same multi-color setup and on the same day as multi-color experiments. These molecules are localized in the same manner as multi-color data, and colors are selected for using the alpha ratio of each localization.

The percentage of molecules that are misidentified out of the whole of the selected molecules is used as the bleed-through rate. Bleed-through rates depend on the choice of alpha values to include and are chosen such that the bleed-through rate is <10% for both Dendra2 and PAmKate.

2.2.6. Drift Correction

Following the method of Mlodzianoski et al,[151] drift correction was applied to fixed samples by binning molecules onto a grid (spacing 100nm) into chunks of 10,000 molecules. Chunks are then cross correlated with each other for all points i and j according to equation 2.5, where C is the cross correlation at the point (i,j), M is the image width, N is the image height, X and Y are the matrices of two binned successive chunks, and i and j are offsets in x and y respectively.

$$C(i,j) = \sum_{m=1}^{M} \sum_{n=1}^{N} X(m,n)\, Y(m-i, n-j) \quad (2.5)$$

Each successive chunk is cross correlated, then peak-peak offsets of the cross correlation were determined and plotted. Drift was computed using the lowest order polynomial (2 or less) that best fit the offsets and were applied directly to localized coordinates on a per frame basis.[151]

2.2.7. Bead Calibration Sample Preparation

Bead calibration samples were prepared using Nunc™ 8-well chambers with #1.5 coverglass bottom. First, the wells were rinsed 3x with PBS to remove possible fluorescent contaminants from the coverglass surfaces. 200µL of poly-L-lysine was then applied to each chambered well and incubated at room temperature for 2 hours so that the poly-L-lysine has time to evenly coat the surface of the glass. After this incubation, the poly-L-lysine was removed, and the chambered wells were rinsed 3x with PBS. Tetraspeck™ fluorescent microspheres (Invitrogen, T7279, 0.1µm beads with 4 fluorescent dyes attached that emit between ~430nm and 680nm) were vortexed for 30s to remove clumps and then diluted with distilled water (total volume 100µL) to make dilutions from 1:25 to 1:100, which then were added to subsequent chambers on the Nunc™ chambered coverslips. The microspheres were then left to incubate in the dark at room temperature for 2 hours, allowing enough time for some of the microspheres to

adhere to the layer of poly-L-lysine previously applied to the glass surfaces. After incubation, the chambered coverslips were then washed again 3x with PBS and covered with a few drops of FluorSave™ reagent (MilliporeSigma, 345789), which helps prevent the dyes from photobleaching. The sample is then left to dry for 1-3 hours and stored in aluminum foil to prevent photobleaching.

2.2.8. Glucose Oxidase Imaging Buffer

For imaging Alexa 647 organic dye, a glucose oxidase buffer (GLOX) was needed to allow the organic dye to blink for super-resolution imaging. GLOX was prepared the day of imaging based on the protocol for dSTORM[152] and according to the following reagent concentrations: 10µg/mL Catalase from bovine liver (Sigma-Aldrich, C9322), 50µg/mL glucose oxidase from Aspergillus niger (Sigma-Aldrich, G2133), 10mM Tris-HCL, 10mM MEA, and 10% glucose diluted into PBS.

All reagents were prepared individually and combined only just prior to imaging. New GLOX buffer was made every hour of imaging, as the effects of the GLOX buffer were noticeably reduced after this time.

2.3. Confocal Imaging

Confocal imaging was performed with two different commercial microscopes, an Olympus FV-1000 (using an UPLSAPO 100X, 1.40NA oil objective, 195µm pinhole) and a Zeiss LSM 510 (using a Plan-Neofluar 40x/1.30NA oil objective, 156µm pinhole). Laser power was kept relatively low (<1.5mW) to avoid excessive bleaching of the fluorescent samples and high voltage was adjusted to maximize signal while avoiding saturation of pixels. In either setup, 488nm and 635nm lasers are used with a quad-band dichroic for sample excitation. For the Dendra2 channel, a band-pass filter from 505-525nm was used and for the Alexa647 a 655-755nm band-pass filter was used. Bleed-through was tested by exciting a multicolor sample with either the 488nm or 635nm lasers with both channels on and was found to be negligible compared to signal.

2.4. Analysis Methods

2.4.1. Pearson Correlation Coefficients

To quantify the level of whole cell correlation between PH domain and Dendra2-HA, we used Pearson Correlation Coefficients (PCC).[67] Localizations for PCC analysis were tolerance-applied, duplicate removed, color separated, and rendered by binning molecules into a grid and convolving them with a 50nm radius circle to help account for localization precision. Since Pearson coefficients are measured relative to the mean value for the cell, data acquired from each cell was masked manually to exclude localizations from the empty space outside the cell, as the empty space can contribute to false correlation. Pearson coefficients were calculated according to equation 2.6, where G_i and R_i represent the intensity for the i-th box in the green and red binned images respectively.

$$PCC = \frac{\sum_{i=1}^{n}(G_i-\bar{G})(R_i-\bar{R})}{\sqrt{\sum_{i=1}^{n}(G_i-\bar{G})^2}\sqrt{\sum_{i=1}^{n}(R_i-\bar{R})^2}} \quad (2.6)$$

PCCs result in a single value between -1 and 1 for each cell that indicates the degree of spatial correlation between two species. A PCC of 1 indicates complete correlation between the two species, PCC=0 indicates no correlation, and PCC=-1 would indicate complete anti-correlation.

2.4.2. Manders' Colocalization Coefficients

Manders' co-localization coefficients (MCC) for FPALM data were calculated after tolerancing, drift correction, bleed-through correction, and rendering by convolving localizations with a circle of radius 50nm, as before. The Manders' co-localization coefficients are defined for each color channel, green and red, as described by equations 2.7 and 2.8.[153]

$$MCC_G = \frac{\sum G_{colocal}}{\sum G_{all}} \quad (2.7)$$

$$MCC_R = \frac{\sum R_{colocal}}{\sum R_{all}} \quad (2.8)$$

MCC is the sum of the intensity of all the pixels that are colocalized with a second color, divided by the sum of all the intensities of the first color. The MCC is defined for both color channels independently, with each measured relative to the sum of pixels containing their own color.

Consequently, the MCC values need not be the same for each color; for example, all the measured green pixels may colocalize well with red pixels, but red pixels may exist in locations other than with the green pixels. Unlike Pearson's Correlation Coefficients, MCCs measure only whether the two channels overlap and do not take into account the relative variation of the two.[154]

2.4.3. Cluster Identification

To identify clusters, molecules are first separated by color into two groups, "green" and "red," (which typically identify the colors of the two species of molecules being studied, even if their emission spectra are of different colors) using alpha histograms, then are corrected for species bleed-through, for x-y stage drift, for duplicate removal, and for tolerances to reduce false positives. Molecules are then rendered by creating a grid with a 20nm spacing and then binning molecules onto it to create a density map.[155] To account for localization precision of the molecules, the density map is then convolved with a uniform normalized circle of 50nm radius (kernel size 5 pixels). The cell area was estimated using the summed area of all the binned molecules and the cell average density was calculated by counting the number of molecules localized and dividing by the occupied area in the grid. Clusters for each species are determined by thresholding 3 times above the average cell density (see Kriegel et al[156] for a review of density-based clustering). Cells observed to be expressing fewer than 10% of the total molecule count of either species (post bleed-through correction) were not considered in the analysis.

2.4.4. RDF Calculations

Radial distribution functions (RDFs) were calculated from FPALM data after tolerancing, drift correction, bleed-through correction, and rendering by convolving FPALM localizations with a circle of 50nm radius. RDFs were calculated according to equation 2.9, as well as for the underlying PH domain, where $N(r)$ is the sum of pixel values within a ring of radius r±10nm from the center of mass of each identified cluster, $A(r)$ is the area occupied by the ring at radius r±10nm (the number of boxes in the ring

times the bin size squared), and ρ_0 is the average cell density (sum of all pixel values in the cell divided by the total cell area), such that $\rho(r) = g(r)\rho_0$.[157]

$$g(r) = \frac{N(r)}{\rho_0 A(r)} \quad (2.9)$$

RDFs were calculated starting the from centroid of each cluster and radiating outward with 20nm width rings in a radially symmetric manner from 0.01μm to 1.0μm from the cluster center and then averaged together for all clusters in each cell.

To avoid edge effects, RDFs were not allowed to be calculated from boxes that fell outside the area of the cell, but in order to include data from clusters on the cell edges, partial RDF rings were allowed and calculated from those boxes falling only within the cell area. To correct for inaccurate measurements of the average cell density, a small correction factor (typically <1.15) was applied to ρ_0 on a per cell basis using values near the 1μm edge of the RDF, to cause the RDF to reach 1 at distances far from the cluster center.

2.4.5. Cluster Properties

Cluster properties were extracted from rendered localizations after cluster identification. The cluster properties area, circularity, and perimeter were extracted directly from masks of clusters (i.e. all contiguous pixels above the applied density threshold) using the regionprops command in MATLAB. Circularity is defined by equation 2.10, where the circularity of a perfect circle is 1, but the circularity increases as the shape becomes more ellipsoidal.

$$C = \frac{4\pi A}{P^2} \quad (2.10)$$

Densities were calculated afterwards by applying cluster masks to the original renders to extract intensities and then dividing by each clusters area.

2.4.6. Software and Significance Testing

All analysis code for localization, cluster identification, trajectory analysis, duplicate removal, and RDF calculation was generated in MATLAB and executed in version 2016b or later. Significance testing for

RDFs and cluster properties were performed using GraphPad Prism 8.3.1 using data imported from MATLAB analysis files.

CHAPTER 3

EVIDENCE FOR INTERACTIONS BETWEEN HA AND PIP2

3.1. Preface

Parts of this chapter were adapted from the paper "Influenza Hemagglutinin Modulates Phosphatidylinositol 4,5-Bisphosphate Membrane Clustering" by authors Nikki M. Curthoys, Michael J. Mlodzianoski, Matthew Parent, Michael B. Butler, Prakash Raut, Jaqulin Wallace, Jennifer Lilieholm, Kashif Mehmood, Melissa S. Maginnis, Hang Waters, Brad Busse, Joshua Zimmerberg, and Samuel T. Hess, published in Biophysical Journal, Vol. 116, 893-909, March 5, 2019.[99] This chapter is meant to serve as a synopsis of the published work, highlighting findings that are relevant to results to be presented later.

3.2. Introduction

The nanoscale clustering of lipids and proteins in the plasma membrane (PM) is crucial to numerous fundamental cellular processes, however, there is considerable disagreement in the field about the precise mechanisms involved.[158] Several proposed models include confinement by the actin cytoskeleton,[132,134] protein targeting to ordered lipid raft domains,[23] and arrangement into lipid shells.[131] Such models are difficult to confirm, since they are purported to be highly dynamic and occurring on very short length scales.[131,138] Furthermore, clustering of proteins appears to also be important to viral processes, such as the clustering of influenza viral proteins on the PM.[14,159] HA forms clusters spontaneously on the membranes of host cells, even in the absence of other viral proteins.[16,24,73] Since a high density of HA is required for efficient viral entry, budding and infectivity, clustering is vitally important to the IAV life cycle,[14,72] yet there is not agreement on the mechanism of clustering or which lipids co-cluster with HA.[25,160–162]

Since HA is known to rely on actin comets mediated by phosphatidylinositol (4,5) biphosphate (PIP2) for transit from the Golgi to the PM[100,101] and HA has shown remarkable co-localization with actin rich membrane regions,[72,73] we hypothesized that PIP2 might serve as a functional link between HA and

the actin cytoskeleton. HA contains several highly conserved palmitoylation sites and positive residues in its cytoplasmic tail domain (CTD) which are known play a role in PIP2 interactions[163–165] and membrane association[163,164] in other proteins. PIP2 binds and regulates many actin binding proteins (ABPs) which modulate the actin cytoskeleton,[166] regulates a variety of cellular processes,[166,167] and is capable of modulating adhesions between the PM and cortical actin to control function.[168] PIP2 has also been observed to form clusters on the PM,[169,170] although not all studies show agreement in this respect.[145,171] Nanoscale membrane clustering has previously been hypothesized to be due to interactions between actin, myosin, membrane proteins, and lipids and has been implicated in IAV infection.[72,73,140,172,173]

3.3. Results

To determine if the relationship between HA and PIP2 carries over to the plasma membrane, we began by expressing a marker for PIP2, pleckstrin homology domain from phospholipase C δ (PLC δ) as a fusion protein with cyan fluorescent protein (CFP),[174] in NIH3T3 cells and observed that PIP2 formed clusters on the PM in the absence of viral proteins (data not shown), which is consistent with previous studies that show that PIP2 forms clusters on the membrane.[169,170] We next tested whether there was spatial correlation between HA expressed at the PM and PIP2. CFP-PLC δ PH domain was transfected into NIH3T3 cells stably expressing HA (A/Japan/305/57) (HAb2 cells),[15] and was further labeled with a monoclonal antibody to HA, along with a secondary antibody with attached Alexa 647, and imaged using confocal microscopy. PH domain and HA show extraordinary colocalization at the membrane of cells (figure 3.1) on a diffraction limited scale. Since HA and PH domain colocalized strongly at the PM using a diffraction limited technique, we also wondered if this colocalization would extend to the nanoscale. FPALM imaging was conducted with two biological configurations, using NIH3T3 cells expressing Dendra2-HA (X-31B, Puerto Rico/8/1934-Aichi/2/1968) and PH-PAmKate, and using HAb2 cells expressing PH-Dendra2 and tagged with an anti-HA antibody (Fc125) with an attached Alexa 647 organic dye. In both super-resolved cases, colocalization can be frequently observed. To quantify the level of spatial

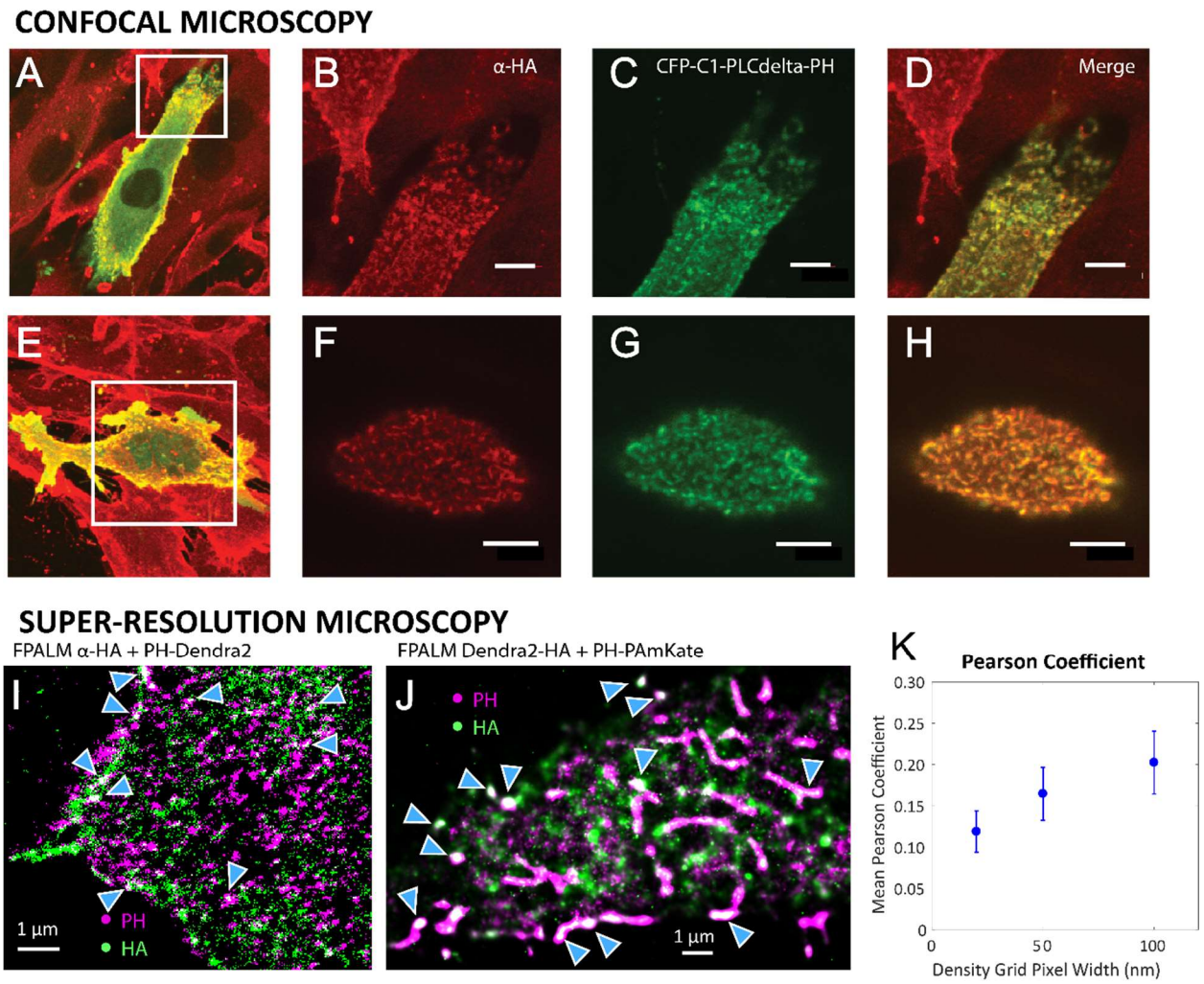

Figure 3.1: Confocal and super-resolution microscopy of HA and PLC δ PH domain show colocalization at varying length scales. (A)-(H) HAb2 cells were transfected with CFP-C1-PLCδ-PH domain (green) and labeled with Fc125, an antibody to HA, along with an Alexa 647 secondary antibody (red). Regions of overlap appear in the diagram as yellow. (A) and (E) show the confocal projections of all axial slices taken while (B)-(D) and (F)-(H) show magnified regions of each channel and the channel merge. (I) and (J) are selected renders from super-resolved FPALM data of HA and PH using two different labeling methods. (K) Pearson coefficient for super-resolved FPALM data that has been binned into a density map from both plasmid and antibody labeling (N=20) for 3 selected bin sizes. The Pearson coefficient remains slightly positive, indicating a positive correlation between HA and PH domain.

correlation between PH-PAmKate and Dendra2-HA, we also calculated the Pearson coefficient by directly binning the molecules onto grids with spacings of 20nm, 50nm, and 100nm. In each case, the Pearson coefficient remained positive, indicating a positive correlation between Dendra2-HA and PH-PAmKate.

Due to the dependence of influenza infectivity on HA densities and clustering,[14,15] we also examined the densities and areas of PH domain and HA clusters to see if they would vary when high or low amounts of HA or PIP2 are present, respectively. Clusters of either species were identified by thresholding 4 times above the average density of the cell. Cluster densities and areas were determined using the regionprops command in MATLAB then plotted against each other, and in each case, clusters formed with a range of sizes and densities, with most clusters remaining in a region $<0.04\mu m^2$ and <10 times the average cell density. HA clusters tended to occupy a larger range of densities than PH domain, as indicated by the wider band (figure 3.2). The plots in figure 3.2 are broken into four categories: Clusters of PIP2 with high and low amounts of HA and clusters of HA with high and low amounts of PIP2, where "high" is considered to be 5 times above the cell average and "low" is less than 0.05 times the cell average. The mean densities and areas were then calculated for each of the 4 conditions, the results of which are seen in table 3.1. HA cluster density is observed to increase significantly in area in regions with High PIP2, while PIP2 clusters significantly increase in density and area in regions with high HA.

To examine whether spatial gradients of HA and PH domain are related, we calculated the average density profile of clusters of HA and PH domain in two ways: 1) an erosion based method (figure 3.3 D), starting from the edges of clusters and eroding one row of grid pixels per step to the centers of clusters, and 2) using a radial distribution function (figure 3.3 E) which is radially symmetric from the center of mass coordinate of each cluster. With either method, a decreasing trend in the PH domain underlying HA clusters is readily apparent and parallels that of the HA.

	PIP2			HA		
	Low HA	*High HA*	*Significance*	*Low PIP2*	*High PIP2*	*Significance*
Mean Density (relative to avg)	6.1 ±0.6	7.6 ±0.8	****	11 ±5.0	7.0 ±0.5	ns
Mean Area (μm^2)	0.0145 ±0.0020	0.0257 ±0.0060	****	0.0105 ±0.0005	0.0231 ±0.0014	**
Number of clusters	1065	666	-	1140	1233	-

Table 3.1: Table of PIP2 and HA in regions of high or low HA and PIP2. Dense clusters of HA or PIP2 (>4 times cell average) were compared to in regions of high (>5 times cell average) and low (<.05 times cell average) PIP2 or HA respectively. Significance testing for differences between groups was done using the Mann-Whitney U-test, where significance star ratings are as follow: p<.05 (*), p<.01 (**), p<.001 (***) and p<.0001 (****).

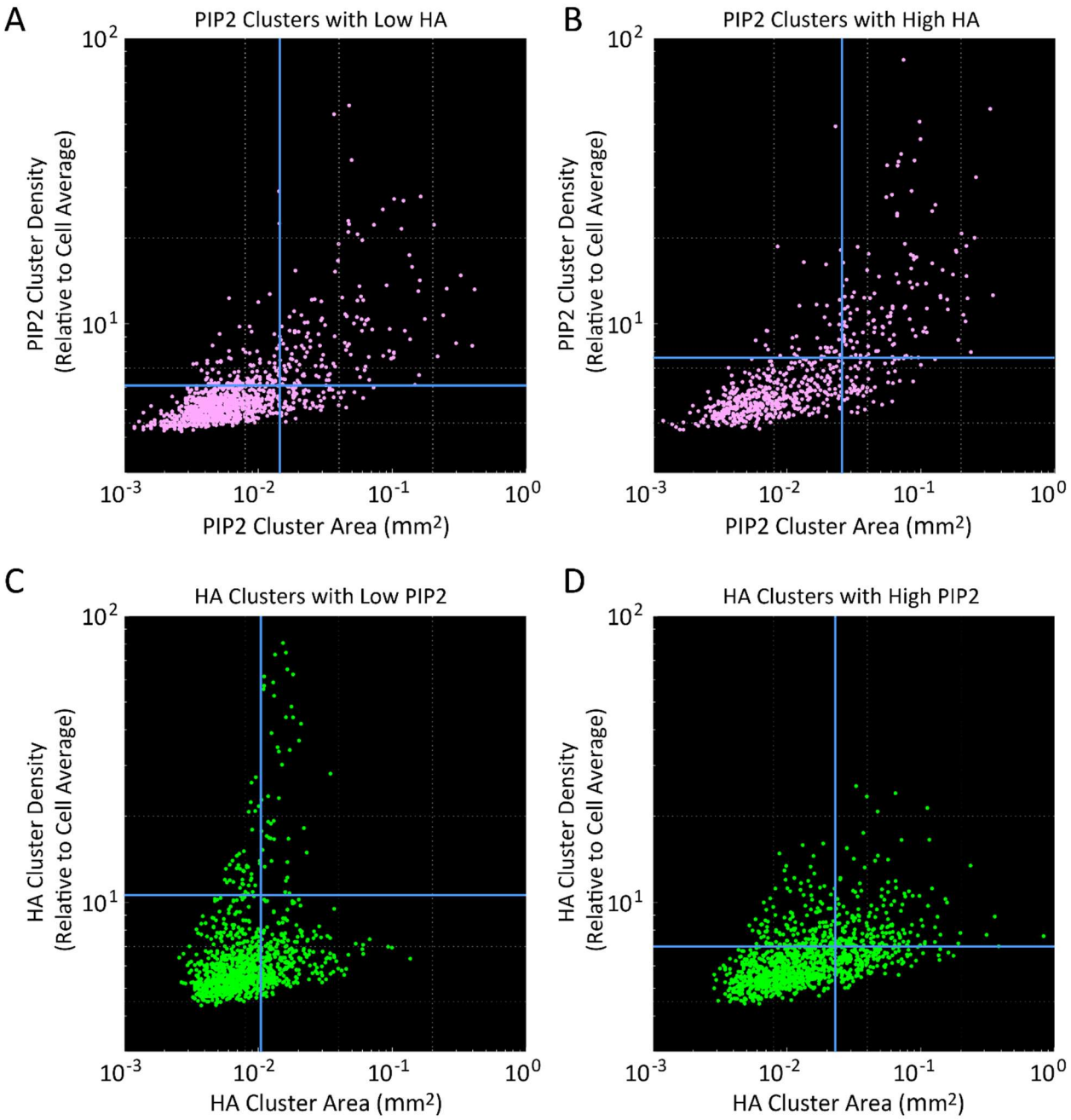

Figure 3.2: Density vs area for clusters of PIP2/HA in the presence of low or high densities of HA/PIP2. (A)-(B) Plotted density vs area for clusters of PIP2 (magenta) in regions with high (>5 times cell average density) and low (<.05 times cell average density) HA. The mean densities, 6.1±0.6 and 7.6±0.8, and mean areas, 0.0145±0.0020 and 0.0257±0.0060, with low and high HA are plotted in blue lines. (C)-(D) Plotted density vs area for clusters of HA (green) in regions with high (>5 times cell average density) and low (<.05 times cell average density) PIP2. The mean densities, 11±5.0 and 7.0±0.5, and mean areas, 0.0105±0.0005 and 0.0231±0.0014, with low and high PIP2 respectively are plotted in blue lines. PIP2 clusters are significantly denser and larger in regions of high HA, while HA clusters significantly larger in areas of high PIP2.

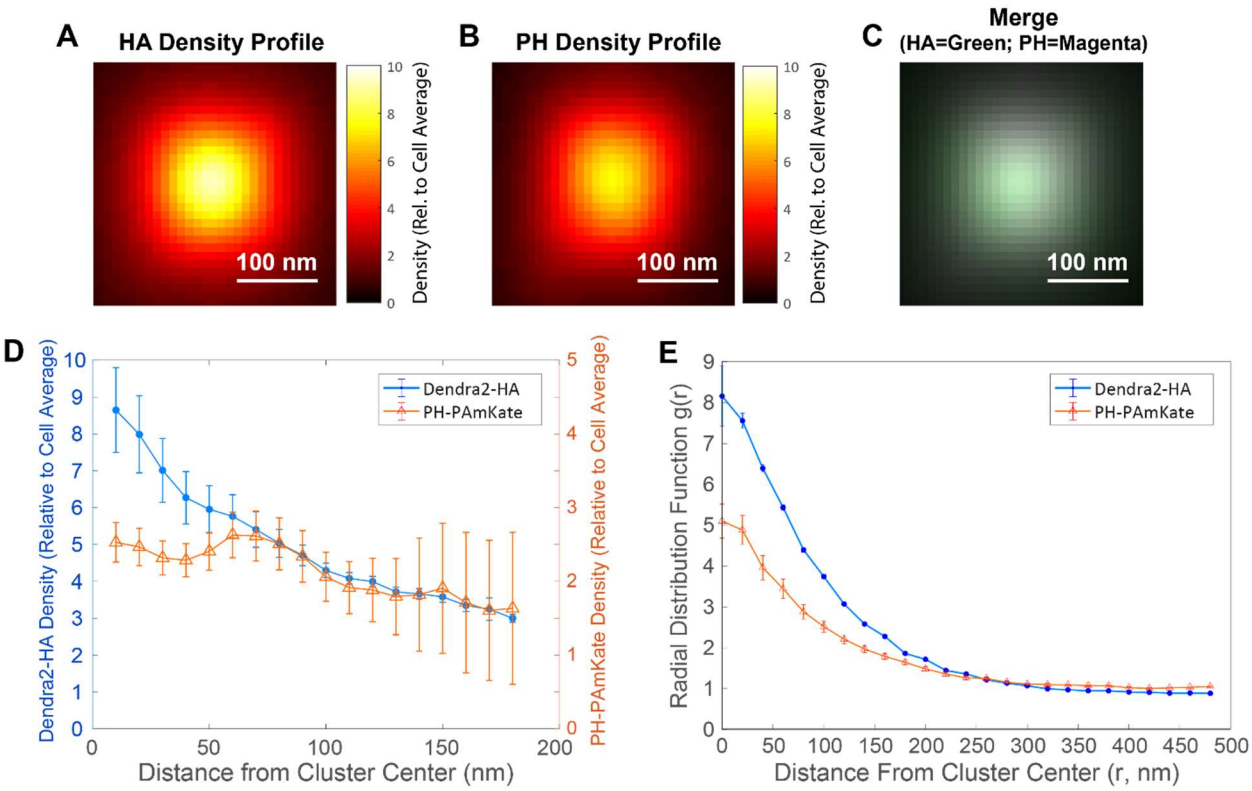

Figure 3.3: HA and PH domain display similar spatial distributions within clusters. (A)-(C) Average density profiles of Dendra2-HA (A) and PH-PAmKate (B) clusters (containing at least 20 molecules), as well as the merge of the two (C) with each clusters center of mass aligned at the origin. Density profiles share similar spatial dependence in clusters, as noted by the overlap in the merge. (D) Average density (relative to average) of HA clusters (n=4010 clusters among 15 cells and 2 biological replicates) and underlying PH domain as measured in annular shells of 10nm. (E) Radial distribution function for clusters of HA and underlying PH domain (n=1969 clusters among 15 cells and 2 biological replicates) as measured from the center of mass of clusters radiating outward with rings of 20nm. Both density profiles and RDFs for HA and PH domain parallel each other and decay together as a function of distance from the centers of clusters. Error bars indicate standard error of the mean.

3.4. Discussion

Using both super-resolution and diffraction-limited methods, HA and PH domain are closely spatially associated at the PM. Regions of colocalization are frequently observed, although not all HA clusters colocalize well with PH domain. Evidently PIP2 colocalization is not a requirement for HA clustering but is spatially associated often enough to warrant further investigation. At shorter length scales, using super-resolution microscopy, the Pearson Correlation Coefficient (PCC) remains slightly positive, indicating a minor correlation between HA and PH domain. However, a small PCC is somewhat expected since PIP2 clusters in the cell for other reasons, even without HA present,[169,170] which is expected to reduce the PCC. Nonetheless, PH domain is frequently observed within dense clusters of HA using a variety of labeling methods and among two subtypes of HA (A/Japan/305/57 and X-31B). Although they are frequently found together in clusters, this alone does not suggest a direct interaction between HA and PIP2, as they may cluster together with a common interaction partner; however, these findings are suggestive of an interaction.

Examination of clusters of HA and PH domain together also display results indicative of an interaction or common interaction partner. Clustering and high densities of HA are known to be important for efficient viral fusion,[14,15,175,176] so if PIP2 enhanced HA clustering, it might contribute to producing more infectious virions. In the presence of high amounts of PIP2, HA cluster areas are increased nearly two-fold, while sustaining similar densities with low PIP2. Additionally, in regions of high HA densities, the clustering properties of PIP2 are altered, where a high amount of HA is correlated with larger and denser PIP2 clusters. Thus, the presence of high densities of HA affect the clustering properties of PIP2 and high densities of PIP2 affect the clustering properties of HA, indicative of an interdependence of clusters of HA and PIP2 on each other. Plots of density vs area for both HA and PIP2 (figure 3.2) also show a slight upward trend as a function of area, suggesting that there is a minimum (and increasing) density needed for larger clusters. Spatial profiles of HA and PH domain were also examined and found to parallel each other within

clusters. As measured from the center of clusters, HA and PIP2 peak at the center of HA clusters and decay outward together. Although PIP2 decays at a different rate and typically reaches a lower peak value, on average PIP2 does not extend past the edges of HA clusters, suggesting that when they are together, PIP2 and HA may be laterally confined within the same regions.

With such a diversity of clusters with and without PIP2, questions remain about how PIP2 is recruited into clusters and whether HA has any direct interactions with PIP2. Some current models for PIP2 recruitment, synthesis, and modulation may help explain some of this diversity. For example, PIP2 may exist in preexisting platforms or un-clustered at the PM,[177] which could be recruited into HA clusters in a time-dependent manner, leading to modulation and reorganization of the actin cytoskeleton.[167] HA clustering on the membrane is also known to induce changes in actin organization,[73] but there are no known interactions between HA and actin or actin binding proteins. PIP2 could modulate these changes. Remarkably, the cytoplasmic tail domain of HA contains 2-3 cysteines and 2 basic residues which are highly conserved among influenza A subtypes.[178] Other viruses, such as HIV and Ebola, are known to recruit PIP2 through a variety of basic residues present on their cytoplasmic tails,[179–186] and polybasic regions of proteins are also known to recruit PIP2 at the PM.[164] This evidence inspired us to further investigate the role of the HA CTD in a putative interaction between HA and PIP2.

CHAPTER 4

MECHANISM OF HA AND PIP2 CO-CLUSTERING

4.1. Introduction

In 1991, DNA sequences obtained from reverse transcription of 13 influenza A HA subtypes were observed to have several conserved homologous regions.[187] Since the virus is highly prone to mutation, regions that remain unchanged among the 18 subtypes must consequently play an essential role in the viral lifecycle and therefore are key areas for study. Of particular interest is the cytoplasmic domain (CTD) of HA, which contains at least 2 cysteine residues that remain consistent among the A subtypes.[42,178,188,189] These cysteine sites are known to undergo palmitoylation, a form of reversible post-translational protein modification wherein a palmitic acid is covalently attached to the protein via an acyl group link. Palmitic acids can be transferred spontaneously in some *in vitro* systems[190,191] but this process is usually assisted by a membrane associated enzyme known as a palmitoyl acyltransferase (PAT). Since palmitic acid is a fairly hydrophobic molecule, when these palmitic acids are attached, and their net charge is neutralized, they effectively act to "pin" the cysteine residues of the CTD to the plasma membrane. In general, palmitoylation serves a variety of functions for native proteins, such as enhancing membrane association and regulation of protein function.[192]

Previous studies on HA tail palmitoylation have shown that the palmitoylation is essential for influenza infectivity[45,46,190] and, in particular, the site most distant from the transmembrane domain appears to be the most important for this.[46,47] The tail has long been thought to be a binding site for other viral components, such as the matrix protein (M1), which forms a layer on the inside of assembled virions and induces membrane curvature to assist in viral budding, or neuraminidase (NA), which assists in cleaving newly formed viruses during budding.[48,193,194] The palmitoylation of the HA CTD also has been shown to alter membrane curvature,[45] which may reduce the energy barrier during the formation of viral

buds. Because of the invariant nature of the cysteines on the CTD and their seeming importance to infectivity, these make promising targets for a "universal therapy" against flu.[195]

Although there are no known structural motifs absolutely required for cysteine palmitoylation, certain patterns are common for cysteine residues that are palmitoylated. Palmitoylation is much more likely to occur on cysteine residues that are adjacent to the transmembrane domain (TMD) of a membrane protein and are almost always accompanied by nearby positive charges,[196,197] a pattern which is consistently followed by HA subtypes, with nearly all containing positive charges in the CTD.[42] Since the CTD of HA consistently contains at least 1 positive residue amongst the numerous subtypes (3 positive residues per trimer), this may act as an interaction site for the negatively charged signaling lipid phosphatidyl inositol (4,5) biphosphate (PIP2), which has been previously observed to be co-localized with HA.[99] Natively, PIP2 comprises only about 1% of the total lipid composition of the plasma membrane[165] but serves a diverse range of important functions for the cell, especially in signaling at the cell surface, regulation of membrane trafficking, and the cytoskeleton.[198] PIP2 is capable of binding many actin binding proteins (ABPs) and affecting their function; for example, PIP2 inhibits profilin (promotes actin assembly),[199] inhibits cofilin[200] and villin[201] (both of which can sever actin filaments), promotes dissociation of capping proteins gelsolin and CapZ,[166] and can activate Ezrin, Radixin, and Moesin (ERM) proteins,[199] which can link the actin cytoskeleton to the plasma membrane. Considering HA clusters are frequently observed together with actin rich membrane regions of the membrane,[72,73] ABPs and actin proteins are found in virions,[173] and GloPIP diffusion is modulated by the presence of HA,[99] PIP2 may serve as a link between influenza and the actin cytoskeleton.

To date, no known PIP2 binding domains have been identified on the influenza HA protein. However, other viruses are known to exploit PIP2 to form clusters on the plasma membrane of infected cells. The most prominent examples are the HIV gag[179,184,185] and Ebola VP40[179–181] structural proteins, which both interact with PIP2 at the plasma membrane. Platforms of the HIV gag protein on the plasma

membrane are completely lost upon depletion of PIP2, and PIP2 is required for successful HIV assembly.[202] HIV gag proteins have been shown to directly interact with PIP2 through a variety of basic residues present in the matrix domain, nearest the inner leaflet of the PM.[182,183] In the case of the Ebola virus, VP40 is thought to interact with PIP2 through cationic side chains of the VP40 protein in order to stabilize clusters.[180] Influenza may follow a similar pattern to allow effective clustering of its proteins on the plasma membrane for assembly prior to viral budding.

HA MUTANT	TMD|CTD AMINO ACIDS	CTD NET CHARGE (@pH 7)	ACYLATION?
HAwt	MWACQ|RGNIRCNICI	+2	Y
HAMAY	MWAMQ|RGNIRANIYI	+2	N
HARE	MWACQ|RGNIECNICI	+0	Y
HAREMAY	MWAMQ|RGNIEANIYI	+0	N
HARREQ	MWACQ|QGNIECNICI	-1	Y
HATailless	MWACQ|	+0	Y*

Table 4.1: Summary of HA CTD mutant alterations. 5 amino acids from the transmembrane region and the 10 amino acids of the cytoplasmic tail domain are shown separated by a vertical line. Amino acid changes from HAwt are shown with a light blue background, while unchanged amino acids of interest are indicated in red. *Although the HATailless mutant has no remaining cytoplasmic tail, an acylation site still exists just inside the transmembrane region, which typically undergoes stearoylation.

To test the effects of palmitoylation and charge on HA clustering at the plasma membrane and co-clustering with PH domain, we acquired mutants of Dendra2-HA with altered CTD sequences, with either changes to palmitoylation sites, net charge (at physiological pH), or a combination of the two, as can be seen summarized in table 4.1. HA wild type (HAwt) from influenza A virus, X-31B (Puerto Rico/8/1934-Aichi/2/1968) was mutated to form HAMAY, where the two cysteines in the CTD, at amino acid positions 562 and 565, and one in the TMD at amino acid position 555 were replaced with amino acids containing hydrophobic sidechains: methionine (M), alanine (A), and tyrosine (Y), which are

incapable of being palmitoylated. To test the effects of CTD charge, we collaborated with Josh Zimmerberg (NIH) and Hang Waters (NIH), who generated the mutants HARE and HARREQ, where the positively charged arginine (R) in the CTD was mutated to the negatively charged glutamic acid (E), or where both CTD arginines were mutated to the neutral glutamine (Q) and glutamic acid respectively. A combination of charge and palmitoylation alterations were tested using HAREMAY, which contains the arginine replacement with glutamic acid as well as replacement of the cysteines. And finally, we acquired a mutant which contains no CTD, the HATailless mutant.

4.2. Results

4.2.1. HA CTD Mutant Clustering

To examine the effects of the cytoplasmic tail domain (CTD) of HA on its physical clustering properties and potential interactions with PIP2, plasmids for the fusion proteins Dendra2-HA (A/X-31B [Puerto Rico/8/1934-Aichi/2/1968]), Dendra2-HA CTD mutants HAMAY, HARE, HAREMAY, HARREQ, HATailless (Hang Waters, Zimmerberg Lab, NIH), and PH-PAmKate (Kashif Mehmood, Maginnis Lab, University of Maine) (pleckstrin homology [PH] domain from phospholipase C δ [PLC δ]),[99] were grown in E. Coli and purified. Dendra2-HA and CTD mutant constructs, along with PH-PAmKate, were then transiently expressed in NIH3T3 mouse fibroblast cells, fixed with 4% PFA for 10 minutes, and then imaged with super-resolution multicolor FPALM.[57] A TIRF illumination geometry[149] was employed to allow for selective illumination of the basal surface of each cell and to reduce out of focus background and cell autofluorescence.

Dense clusters of Dendra2-HA spanning a diverse range of sizes (~30nm-1000nm diameters) and shapes were observed on the cell membranes, in agreement with previous cases of HA overexpression (figure 4.1).[16,72,73] Qualitatively similar clustering was also observed for all five of the Dendra2-HA CTD mutants. PH-PAmKate formed clusters on its own and with the HA, while regions along the cell edges were often found enriched with PH-PAmKate. Compared to HA wild type (HAwt), FPALM renders of Dendra2-

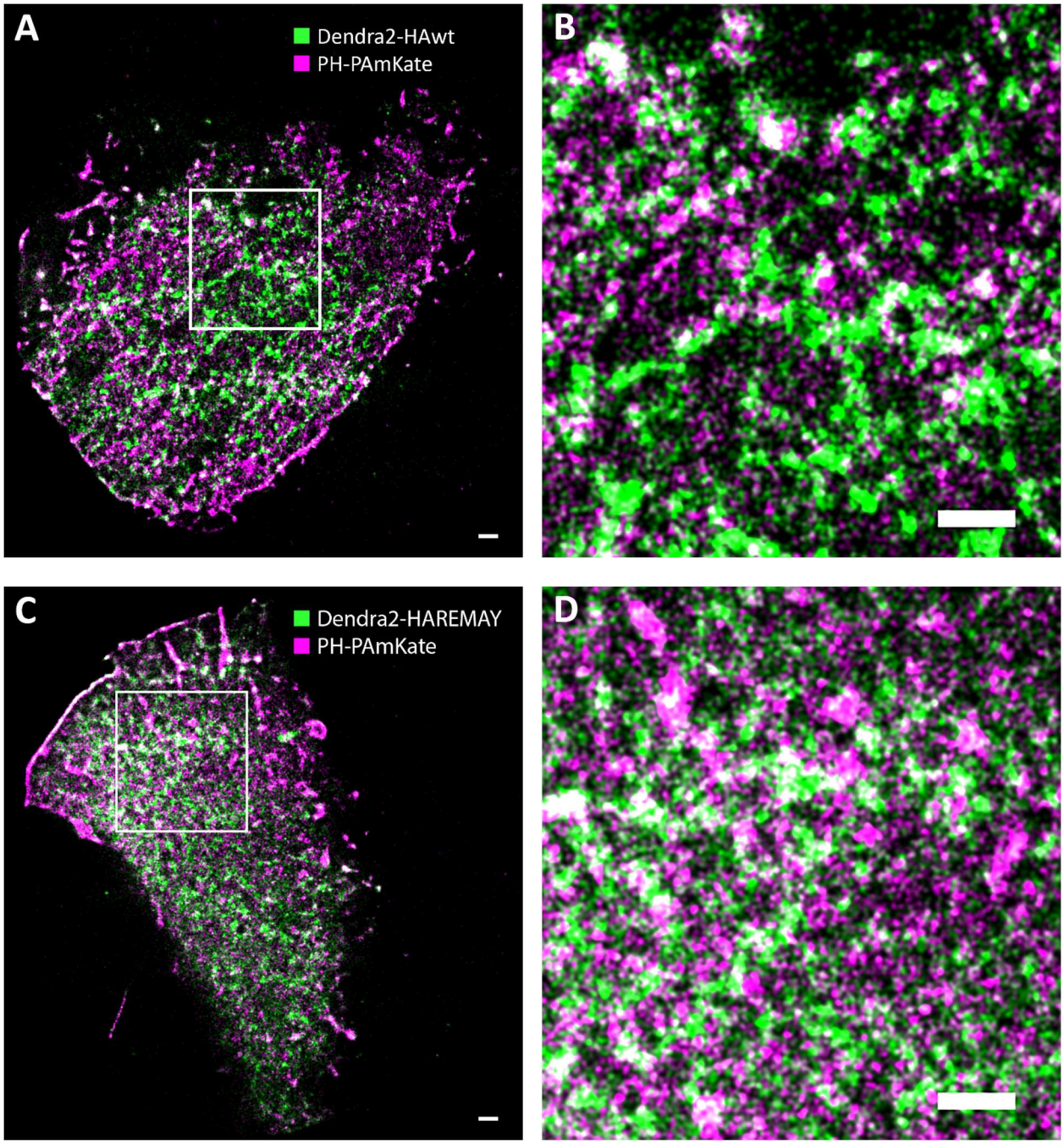

Figure 4.1: FPALM renders of Dendra2-HA and PH-PAmKate in fixed NIH3T3 cells. FPALM data of Dendra2-HA (A) and Dendra2-HAREMAY (C) were convolved with a normalized Gaussian with a localization precision dependent radius. Close up views are visible for the boxed region in panels (C) and (D). HAwt clusters appear tightly clustered on the membrane of the cell with some colocalization (white) between HA and PH domain. HAREMAY CTD mutant also shows similar clusters but qualitatively contains more areas of colocalization. Scale bars are 1 µm in length in each panel.

HAREMAY were visually most different, sometimes displaying less well-defined clusters and more frequent colocalization with PH-PAmKate (figure 4.1).

At first, to examine if any differences between HAwt and the CTD mutants were noticeable throughout the entire cell, we calculated the Pearson correlation coefficients and the Manders' colocalization coefficients (equations 2.7 and 2.8) between HA and PH domain for cells expressing each mutant, as seen in figures 4.2 and 4.3. Although Pearson Coefficients were not significantly different amongst each other, all mutants displayed a slightly positive Pearson coefficient. Among the mutants, Manders' colocalization coefficients were significantly different from wild type only for the double charge mutant HARREQ, showing a 10.6%±3.4% decrease in Dendra2-HARREQ MCC with PH-PAmKate and a 17.1%±4.6% increase in PH-PAmKate colocalization with Dendra2-HARREQ. All HA CTD mutants and HAwt exhibited between 0.69-0.81 MCC with PH domain, despite the low Pearson coefficient.

To characterize the spatial distributions of HA and HA mutants within clusters, we then calculated radial distribution functions (RDFs) for identified clusters of Dendra2-HAwt and Dendra2-HA CTD mutants. For the RDF calculation, drift-corrected, tolerance-applied FPALM localization coordinates for Dendra2-HA and PAmKate-PH were binned onto separate, spatially coincident grids, each with 20nm spacing. Each grid (taken as a grayscale image in Matlab) was then convolved with a uniform circular kernal (i.e. tophat profiled with 50nm radius and integrated intensity of 1), to account for localization precision. Clusters were then identified from the kernal-convolved renders by selecting all regions above a threshold of 3 times the cell-averaged Dendra2-HA density (ρ). Based on the high variability of small protein clusters, those occupying an area smaller than $0.01\mu m^2$ were not considered for the RDF calculation. Cells with low relative expression of either color (less than 10% of the total) or low expression ($\rho<200$ molecules/μm^2) were also omitted from the analysis. After binning molecules and removing cells with poor expression levels, 185 total cells remained with 15,545 total clusters pooled from at least 3 biological replicates (table 4.2). A minimum number of 3 replicates was used to help temper effects from experiment to experiment

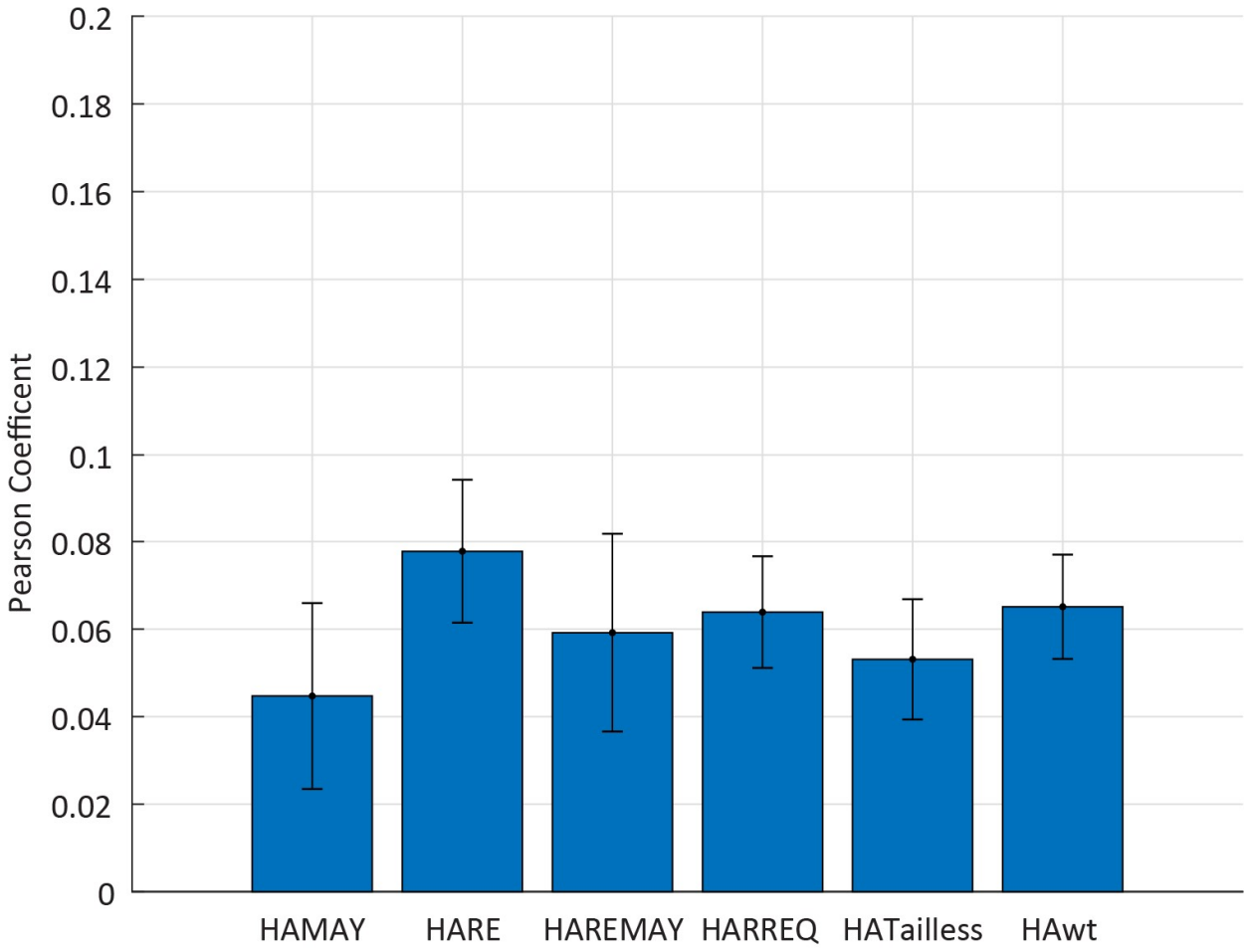

Figure 4.2: Pearson coefficients for Dendra2-HA and PH-PAmKate. Pearson coefficients were calculated after rendering molecules by convolving localizations with a normalized 50nm circle and cell areas were masked automatically using a dilation of the localized molecules. The Pearson coefficients remain slightly positive, indicating a small correlation between HA and PH throughout the entire cell in all the HA mutants. However, there are no significant differences between mutants according to the one-way ANOVA test.

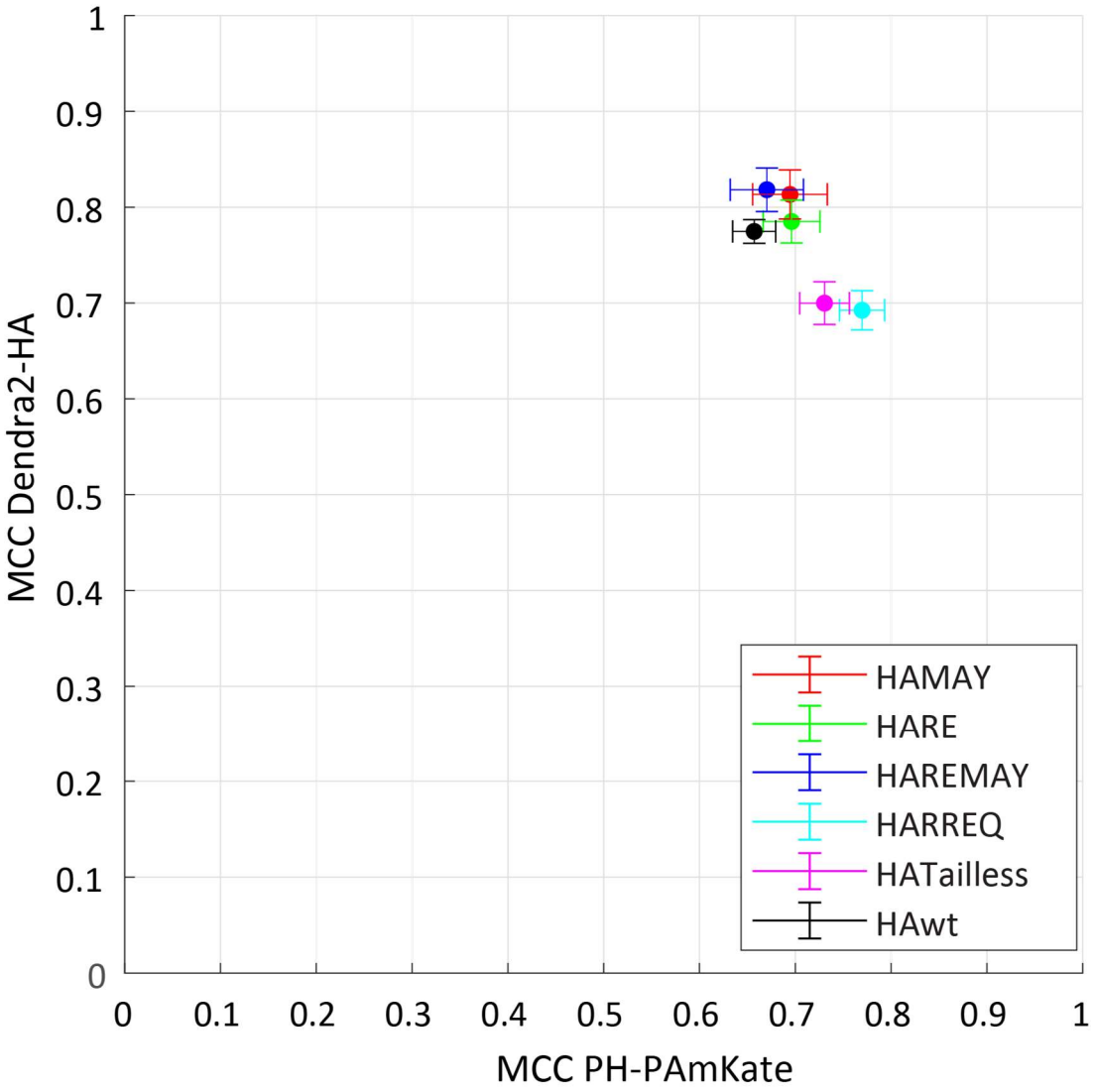

Figure 4.3: Manders' colocalization coefficients (MCC) for Dendra2-HA and PH-PAmKate. MCCs were calculated after rendering molecules by convolving localizations with a normalized 50nm circle and cell areas were masked using an automatic algorithm. Only HARREQ is significantly different ($p<.05$) from HAwt in both MCCs according to the one-way ANOVA test. HARREQ shows a 10.6%±3.4% decrease in colocalization of Dendra2-HA with PH-PAmKate and a 17.1%±4.6% increase in PH-PAmKate colocalization with HARREQ.

HA MUTANT	HAMAY	HARE	HAREMAY	HARREQ	HATailless	HAwt
TOTAL # OF CELLS	22	24	25	30	29	55
TOTAL # OF CLUSTERS	4267	4783	3670	6133	5791	9754
MEAN # CLUSTERS/CELL	194.0 ±12.2	199.3 ±15.2	146.8 ±13.0	204.4 ±12.6	199.7 ±12.4	177.4 ±8.6
MEAN # CLUSTERS/μm^2	0.635 ±0.020	0.618 ±0.018	0.599 ±0.022	0.679 ±0.024	0.633 ±0.023	0.615 ±0.019
BIOLOGICAL REPLICATES	3	3	3	3	3	6

Table 4.2: Table of cells and clusters analyzed per HA mutant. All HA mutants were imaged in at least 3 separate biological replicates and thousands of clusters were identified for each mutant species. Cells expressing less than 10% of either Dendra2-HA or PH-PAmKate (after bleed-through correction) were removed from the data. No significant differences were observed in the mean number of clusters per cell or the clusters per cell compared to HA wild type, according to the one-way ANOVA test.

variability of the cells. For Dendra2-HARREQ, there is a significant 10.4%±4.7% increase ($p<.05$) in the number of clusters identified per square μm of cell area, but the other mutants remain insignificantly changed from HAwt in this respect.

Figure 4.4 shows the result of the RDF calculation with HA wild type and all mutants plotted on the same graph. HA RDFs were observed to be highest in the centers of the clusters, rising to about 4.5-6 times the cell average density, then dropping to about half of the peak density after ~90nm. RDFs are all monotonically decreasing, with the most rapid decrease occurring between 70nm-110nm, before flattening out and slowly approaching 1 (average cell density) at long distances from the cluster center. When compared to HAwt, the central RDF value consistently decreases as mutations are introduced to the CTD. To test if these observed differences were significant, we used the Kruksal-Wallis one-way ANOVA test for each mutant compared to HAwt (see figure 4.5). RDFs for all of the HA mutants show significantly reduced values in their RDFs within 100nm of the cluster center, while maintaining similar RDF shapes overall, although HAREMAY displays the largest and most significant central reduction of

22.1%±5.8% ($p<.001$). HARE, HAMAY, and HARREQ are grouped together, and remain 13.7%±6.1% to 18.6%±6.7% lower in density than the wild type for all regions near the RDF center.

From previous work,[99] we suspected that interactions with the signaling lipid PIP2 may play a role in the clustering behavior of HA, either directly or indirectly.[99] Since the CTD of HA is the only part of the HA molecule that extends outward into the cytoplasm and typically remains close to the inner leaflet, we hypothesize that the tail is a likely candidate for such an interaction. To see if PH domain distributions were altered when changes were introduced to the CTD, we also calculated RDFs for the PH domain underlying the previously identified HA clusters. Figure 4.6 shows the results of the RDF calculations for PH-PAmKate, plotted all on the same graph. The PH domain RDFs peak at their central values, similar to the HA RDFs, but drop to about half of their peak value within 170nm instead of 90nm, suggesting that PH domain remains enriched past the edges of the HA clusters. HAwt, HATailless, HARREQ, and HARE all follow similar patterns, consistently dropping monotonically to 1. In contrast to that, both the MAY mutants, HAMAY and HAREMAY, are not monotonic, although the difference from HAwt is not significant according to the ANOVA test. Figure 4.7 shows the RDF results for PH individually compared to PH domain underlying HAwt. RDFs for PH-domain are not significantly altered from the HAwt RDFs for HAMAY. However, HAREMAY, HARREQ, HARE, and HATailless mutants all show significant differences. In the case of HAREMAY and HARE, there is a significant enrichment with PH-domain in the center of the RDF from 10-110nm, and a maximum of 30.5%±14.6% and 15.4%±15.3% increase from HAwt, respectively. A significant, maximal decrease in the RDFs was observed in the central region for HARREQ of 16.6%±11.6% and HATailless of 13.8%±10.5%.

To ensure that the result remained despite any uncontrolled day to day variability in the experiments, we also averaged the RDFs among individual biological replicates instead of by cell. Although the standard error noticeably increases when averaging by biological replicate, the overall shape and pattern of the RDFs remain unchanged, as can be seen in figure 4.8.

Changes to the algorithm which determines cell area and density (and therefore clusters chosen for analysis) does cause some minor fluctuations to the RDFs of tail mutants HARE, HARREQ, and HAMAY, but the curves always remain between those for HAwt and HAREMAY. The HAwt and HAREMAY mutants are largely insensitive to this parameter, suggesting the result for HAREMAY is much less likely to be due to analysis method. Including very small clusters (<0.01μm^2) increases the variability of the RDF, eventually to the point that differences cannot be seen above the noise. We exclude these very small clusters on the basis that some "clustering" will appear to happen even with completely randomized localizations, but larger clusters are much less likely to appear solely by chance. Additionally, unique molecules localized in multiple consecutive frames are duplicate corrected, since overcounting is a known potential issue with single-molecule localization methods which can produce artifacts in the data.[203]

Although the radial distribution function provides information on how the density of an average HA cluster changes with distance from the center of mass, we wanted to examine other properties of the clusters to better characterize any changes not immediately apparent from the RDFs. Using the same criteria for identifying clusters as for the RDFs, we selected individual clusters using a binary image mask in MATLAB and then analyzed them with the regionprops command.

Cluster densities and areas identified from each cluster and for each mutant are individually plotted on a log-log plot to demonstrate cluster to cluster variance within any HA and HA mutant type (figure 4.9). HAwt and mutants all show remarkable variance in cluster density and area, while also consistently forming a band with clusters spread out more in area than in density. Noticeably, all charts show similarly increasing cluster area as density increases (i.e., positive slope to the density vs area). Clusters of HAREMAY, in particular, appear in a smaller region of the chart with a sharper band, while HAwt shows the widest variation.

From the regionprops data of the HA/HA mutant clusters, we also calculated several physical properties, including mean cluster density, area, perimeter, and circularity. HAMAY, HARREQ, and

HAREMAY mutants all displayed some significant differences from HAwt in one or more cluster property (figure 4.10). A significant 20.1%±5.5% decrease in cluster density, 16.9%±5.0% increase in cluster perimeter, and a 12.8%±2.6% increase in circularity was noted for the HAREMAY mutant, the only mutant to exhibit changes in 3 of the 4 properties examined. HAMAY and HARREQ also exhibited significantly reduced densities from HAwt, although always less than the change seen for HAREMAY. In each of the 4 properties examined, as well as the RDFs for both HA and PH domain, the HAREMAY mutant exhibits the largest and most significant differences from HAwt.

A summary of all the clustering properties and RDF changes can be seen in figure 4.11 and table 4.3.

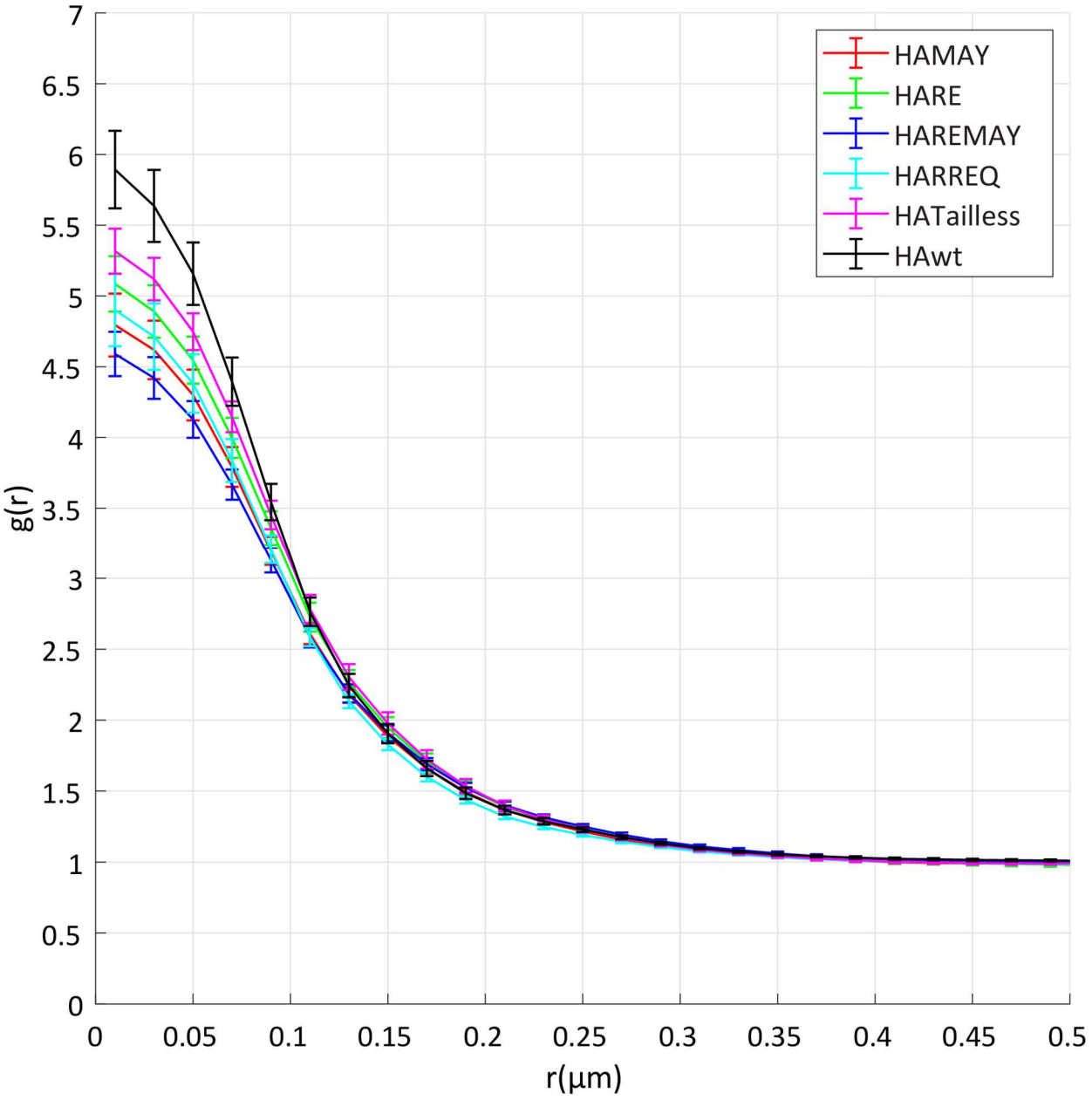

Figure 4.4: RDFs of HA and HA mutant variant clusters averaged by cell. Palmitoylation mutants and charge altered mutants all show reductions in their central RDF values compared to HAwt. HA CTD mutants show general similarities in their RDF curve shapes, all displaying dense central regions that monotonically decrease radially outward from the cluster. HA mutants become more depleted in the central region (less than 0.1μm) as changes are introduced to the CTD. Error bars indicate the standard error of the mean.

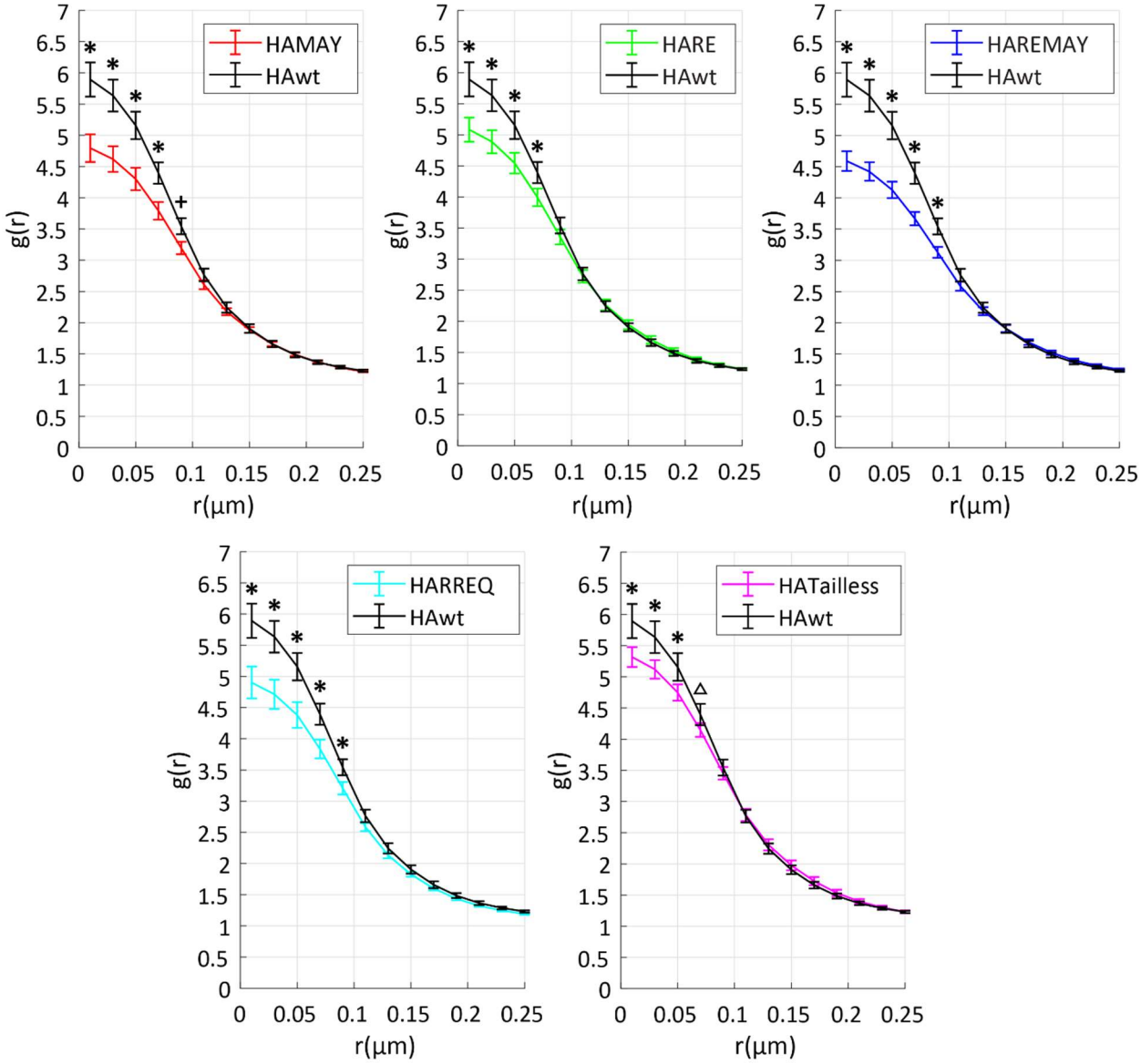

Figure 4.5: RDFs for HA mutants compared to HAwt. RDFs were calculated after FPALM localizations were rendered by convolving individual molecules with a normalized circle of radius 50nm. HAMAY, HAREMAY, and HARREQ mutants all show a significant decrease in the central bump of the RDFs out to 90nm according to the two-way ANOVA test, indicating that these clusters have reduced peak cluster density compared to wild type HA clusters. Values after 90nm are not significantly different between any of the mutants and HAwt. An asterisk indicates p<.001, a plus sign indicates p<.01, and a triangle indicates p<.05. Error bars indicate standard error of the mean.

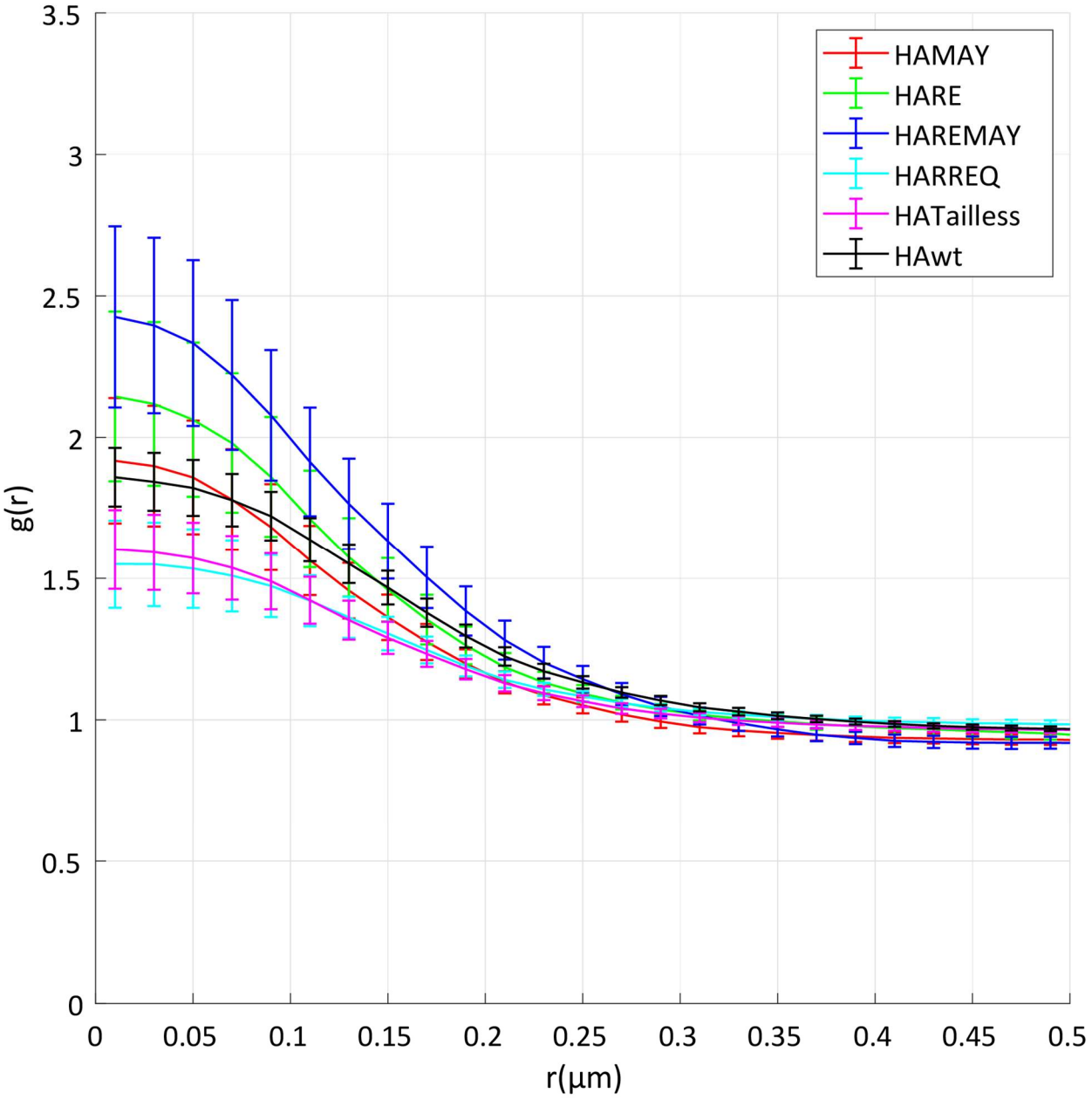

Figure 4.6: RDFs of PH domain underlying HA clusters averaged by cell. RDFs for PH domain under HA clusters remain higher than the cell average and steadily decrease out to 0.3µm. HAREMAY displays the largest difference in shape, rising to nearly 2.5 times the cell average at the centermost point. Error bars indicate standard error of the mean.

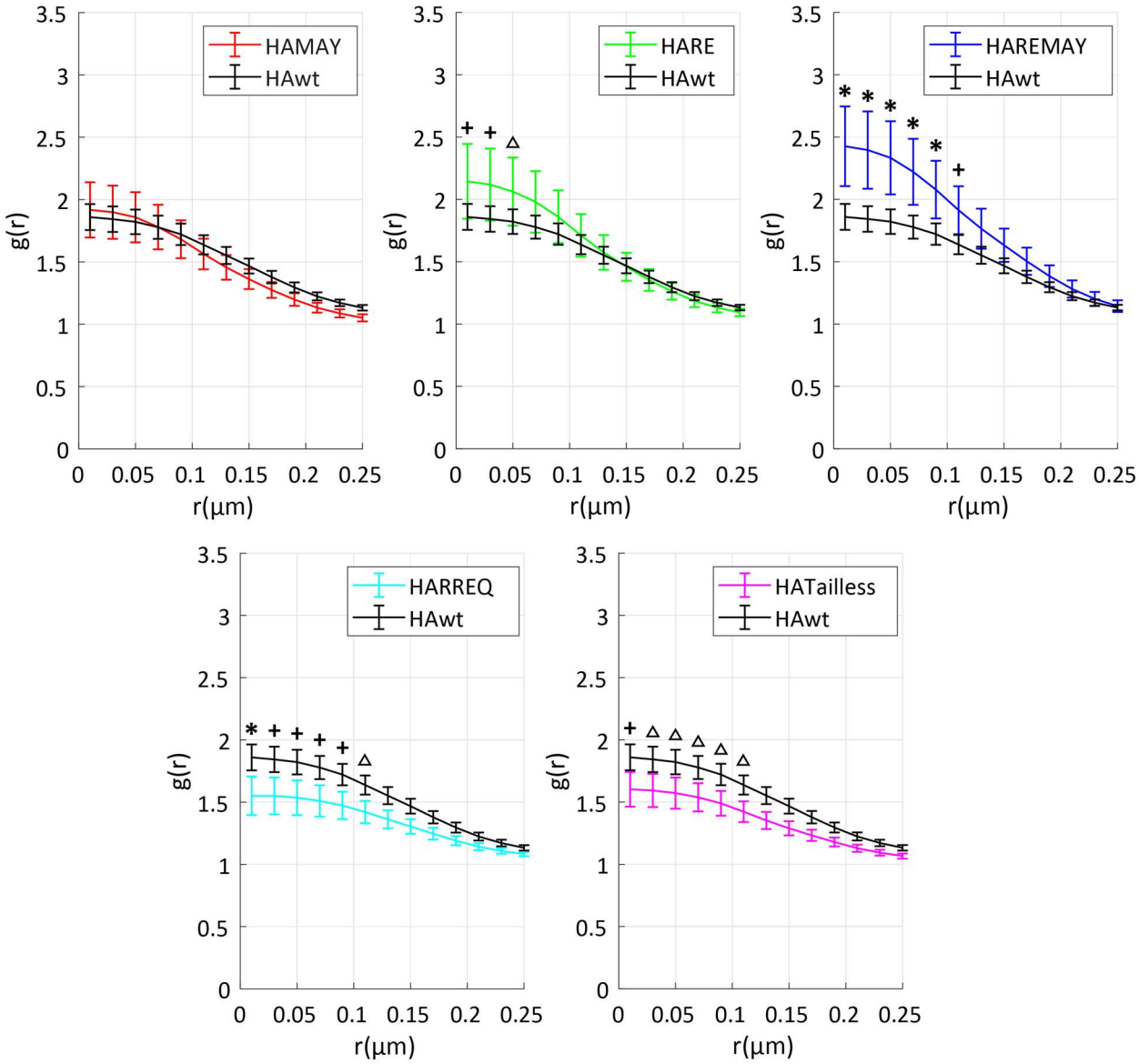

Figure 4.7: PH domain RDFs underlying clusters of HA and HA mutants. For HARREQ and tailless, a small depletion in the curve is observed while HARE shows a small enhancement in PH domain underlying HA. HAREMAY shows the largest change, with a significant 30.5%±14.6% to 16.9%±11.6% increase in the RDF in the region from 0 to 110nm. An asterisk indicates p<.001, a plus sign indicates p<.01, and a triangle indicates p<.05. Error bars indicate standard error of the mean.

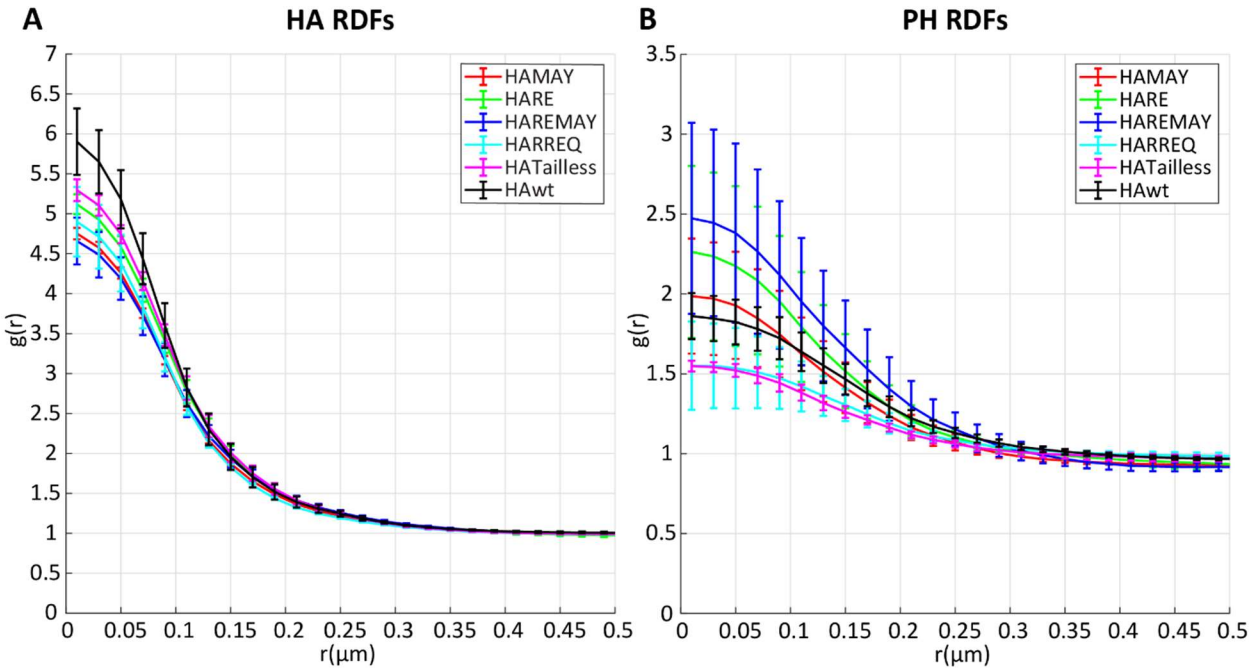

Figure 4.8: RDFs for HA clusters (A) and underlying PH domain (B) averaged by biological replicate. When averaged by biological replicate, the standard error increases but the shape and relative order of the RDFs remains intact, indicating that the results are unlikely to be caused by day to day experimental variations. Error bars indicate standard error of the mean.

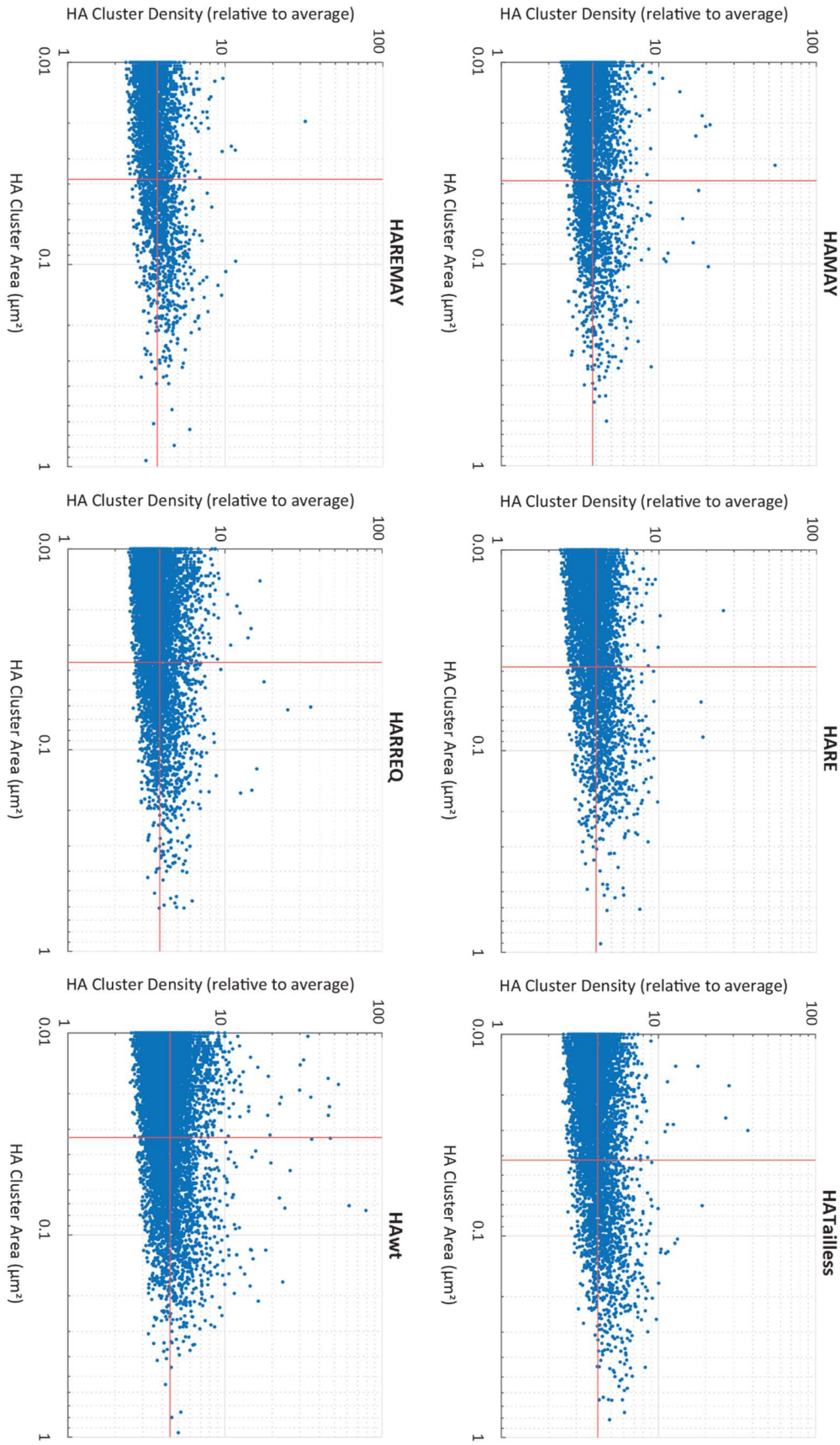
HAMAY
HARE
HATailless
HAREMAY
HARREQ
HAwt
HA Cluster Density (relative to average)
HA Cluster Area (µm²)
100
10
1
0.01
0.1
1

Figure 4.9: Log-log plot of cluster densities versus cluster areas for HA and HA mutants. Clusters have a wide variety of densities for each mutant, with most of the clusters occupying the space below 8 times the cell average. Cluster areas, similarly, display marked variation but the majority of clusters are below $0.2\mu m^2$. HAREMAY appears the most dissimilar from the others, with a tendency for clusters to exhibit lower densities over a similar range of areas and occupying a narrower band of densities. Red lines indicate the average values for density and area.

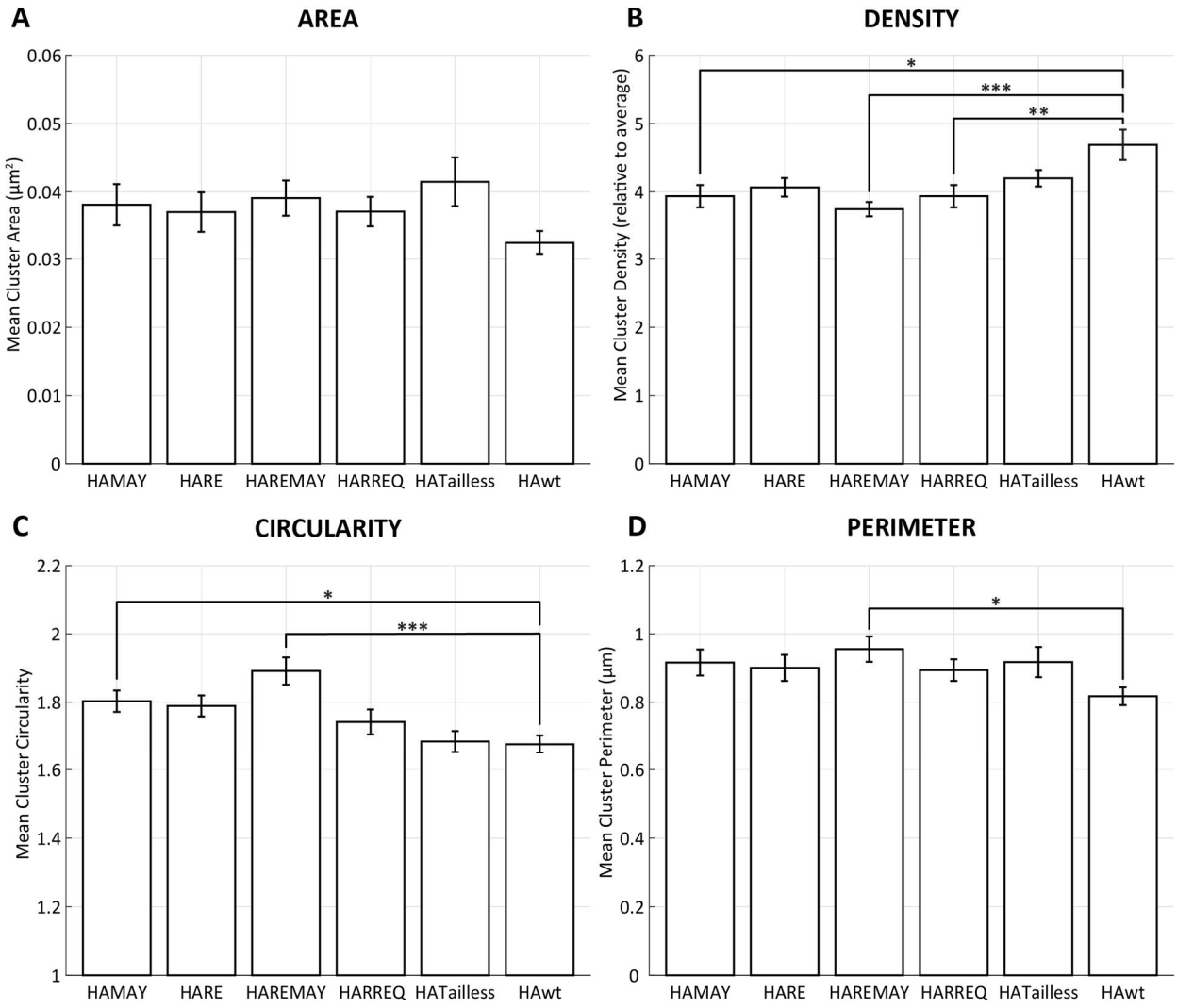

Figure 4.10: Selected cluster properties for Dendra2-HA and Dendra2-HA mutants. Clusters were identified by binning molecules onto a grid and convolving with a circle (radius 50nm) and thresholding 3 times above the cell average. (A) Mean cluster areas for HA and HA mutants. No significant differences were found between the mutants and wild type HA. Mean cluster area overall averages to $0.0375\mu m^2 \pm 0.0158\mu m^2$. (B) Mean cluster densities. Significant decreases in density were observed between HAwt and HAMAY (16.0%±6.3% decrease), HAREMAY (20.1%±5.5% decrease), and HARREQ (16.1%±6.3% decrease). The largest decrease occurs in the mutant with a mix of changes to the CTD, both charge and palmitoylation. (C) Mean cluster circularities. Both palmitoylation variants, HAMAY (7.5%±2.3% increase) and HAREMAY (12.8%±2.6% increase), displayed significant increases in cluster circularity, indicating that the removal of palmitoylation increased the elliptical nature of these clusters. (D) Mean cluster perimeters. Cluster perimeters remained largely unchanged, except for the HAREMAY variant which displayed an increased cluster perimeter (16.9%±5.0%). ANOVA was used for all significance testing where $p<0.05$ (*), $p<0.01$ (**), and $p<.001$ (***). Error bars indicate standard error of the mean.

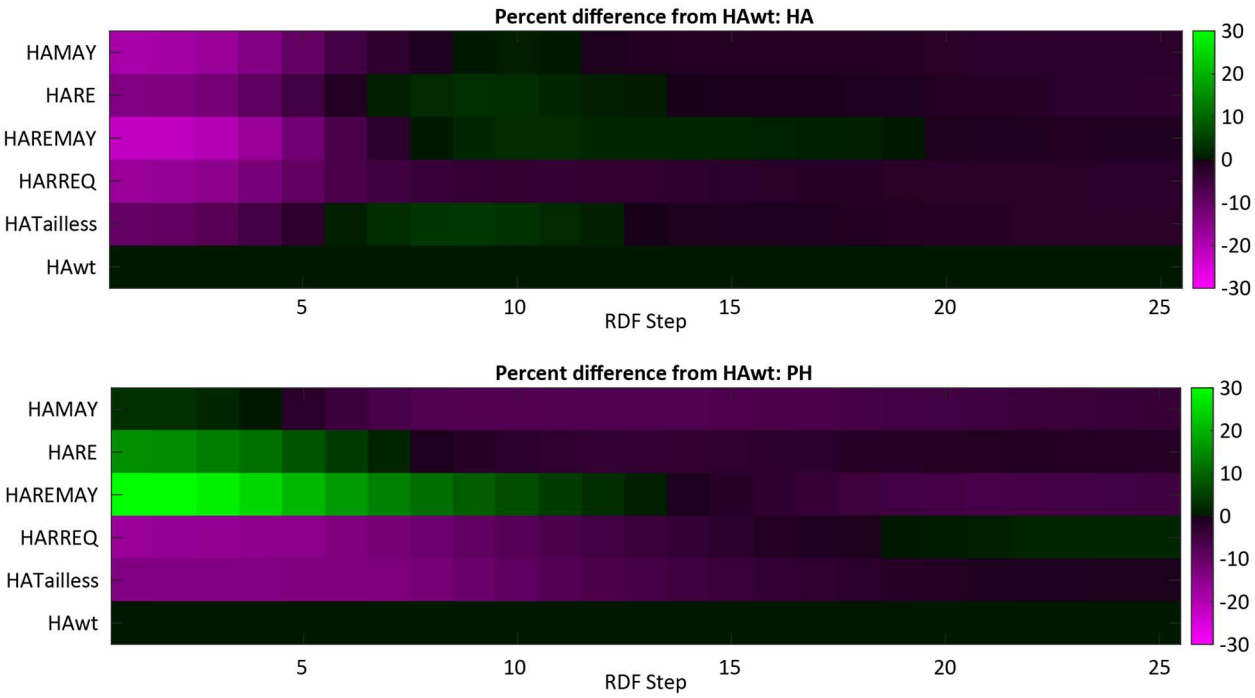

Figure 4.11: Summary of RDF differences from HAwt. Green represents a percentage increase from HAwt, magenta represents a percentage decrease, while black represents no change. HAREMAY contains the most obvious differences in both PH and HA RDFs from HAwt. Each RDF step is 20nm.

SUMMARY OF HA & HA MUTANT MEAN CLUSTER PROPERTIES

HA MUTANT	MEAN DENSITY (rel. to average)	MEAN AREA (μm^2)	MEAN PERIMETER (μm)	MEAN CIRCULARITY
HAMAY	3.935	0.03810	0.9161	1.803
HARE	4.065	0.03702	0.9005	1.789
HAREMAY	3.745	0.03907	0.9553	1.891
HARREQ	3.934	0.03709	0.8939	1.742
HATailless	4.197	0.04147	0.9173	1.685
HAwt	4.687	0.03251	0.8173	1.677

Table 4.3: Summary of cluster properties of HAwt and HA mutants. Significant differences are noted using a colored coded backdrop where black indicates a significant decrease and blue indicates a significant increase as compared to HAwt in dark gray, according to the Kruskal-Wallis one-way ANOVA test. Of the cluster properties tested, HAREMAY shows the most significant, and largest, changes from HAwt.

4.2.2. Labeling Methods

Since we wanted to examine the effects of the CTD on HA clustering and PIP2 interactions, the fluorescent protein gene was placed 5' of the HA gene in the plasmid instead of at the CTD at the 3' end of the gene. However, the location of the HA signal peptide at the beginning of the HA protein has been shown to mediate the trafficking of HA to the plasma membrane, and to affect overall membrane expression levels, as the signal peptide is normally cleaved during membrane insertion. To examine whether the position of the signal peptide relative to the fluorescent protein label played any role in our observations of HA clustering, we compared membrane expression of Dendra2-HA and HA-Dendra2 with HA labeled using a known antibody against HA-X31B. We also compared the level of colocalization between antibody-labeled HA and HA labeled as either (Dendra2-HA) or (HA-Dendra2) using both confocal and FPALM microscopy.

Uninterrupted signal peptide, as is presumably found in HA expressed using the HA-Dendra2 plasmid, shows better overlap of the protein with the α-HA Alexa647 antibody using confocal (figure 4.12 A), while Dendra2-HA shows fewer regions containing both signals. However, since confocal microscopy is not as sensitive as FPALM, we also tested whether Dendra2-HA and α-HA Alexa647 colocalized using FPALM (figure 4.12 B). After localization and tolerancing, the data were binned onto a grid with 50nm box spacing and masked around the cell area. We then used Manders' Colocalization Coefficients (MCC) to characterize the colocalization between Dendra2-HA and α-HA Alexa 647 as seen in figure 4.13. MCCs show similar results for the Dendra2-HA and HA-Dendra2 colocalization with α-HA Alexa 647 but a significantly larger value for the colocalization between α-HA Alexa 647 and HA-Dendra2.

Since we transiently expressed Dendra2-HA and PH-PAmKate, we also examined effects of expression level with the colocalization of Dendra2-HA and PH-PAmKate. Tolerance-applied localized coordinates were converted into a grid plot with 10nm bin spacing and convolved with a normalized 25nm radius Gaussian to produce a render. Pixels containing greater than 4 times the average cell density of

both HA and PH domain were counted as a fraction of all the pixels rendered and plotted versus the average PH localizations per μm^2 and were fitted using a least-squares algorithm (figure 4.14). As HA expression increased, a noticeable drop occurs in the fraction of high HA pixels that were colocalized with PH domain, indicating potential competition between the two for PIP2. The least-squares was fit according an equilibrium model that includes two binding reactions: HA binding to free PIP2, and PH-PAmKate binding to free PIP2, which allows the determination of the ratio of the binding constant (rate of association) of HA with PIP2 and PH with PIP2. Since the binding constant for PH with PIP2 is a known quantity,[144] the effective binding constant between HA and PIP2 can be extracted using the fit parameters and was found to be $2.86\mu m^2 \pm 0.41\mu m^2$.

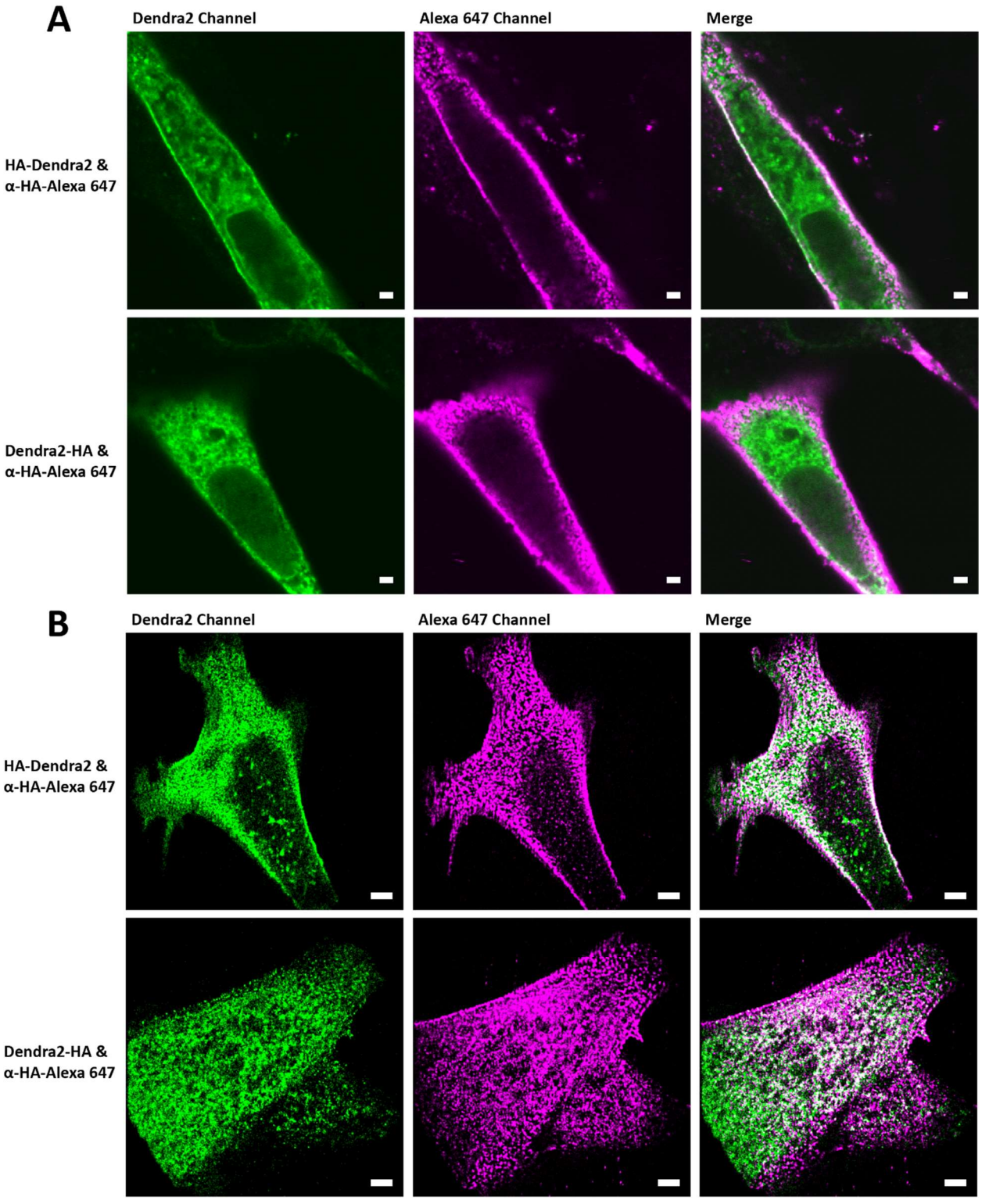
A
Dendra2 Channel
Alexa 647 Channel
Merge
HA-Dendra2 &
α-HA-Alexa 647
Dendra2-HA &
α-HA-Alexa 647
B
Dendra2 Channel
Alexa 647 Channel
Merge
HA-Dendra2 &
α-HA-Alexa 647
Dendra2-HA &
α-HA-Alexa 647

Figure 4.12: Renders of HA-Dendra2 and Dendra2-HA with α-HA Alexa 647. (A) Confocal renders of HA-Dendra2 and Dendra2-HA with α-HA Alexa 647. HA-Dendra2 displays better membrane expression than Dendra2-HA, indicating that it is more efficient at reaching the membrane with the signal peptide intact. However, both contain some degree of colocalization with α-HA Alexa 647 at the membrane. (B) FPALM super-resolved renders of HA-Dendra2 and Dendra2-HA with α-HA Alexa 647. Since the antibody does not efficiently label the basal membrane, images were acquired in thin sections of the cell or towards the apical membrane. Both HA-Dendra2 and Dendra2-HA display similar levels of colocalization with α-HA Alexa 647. Scale bars are 2μm.

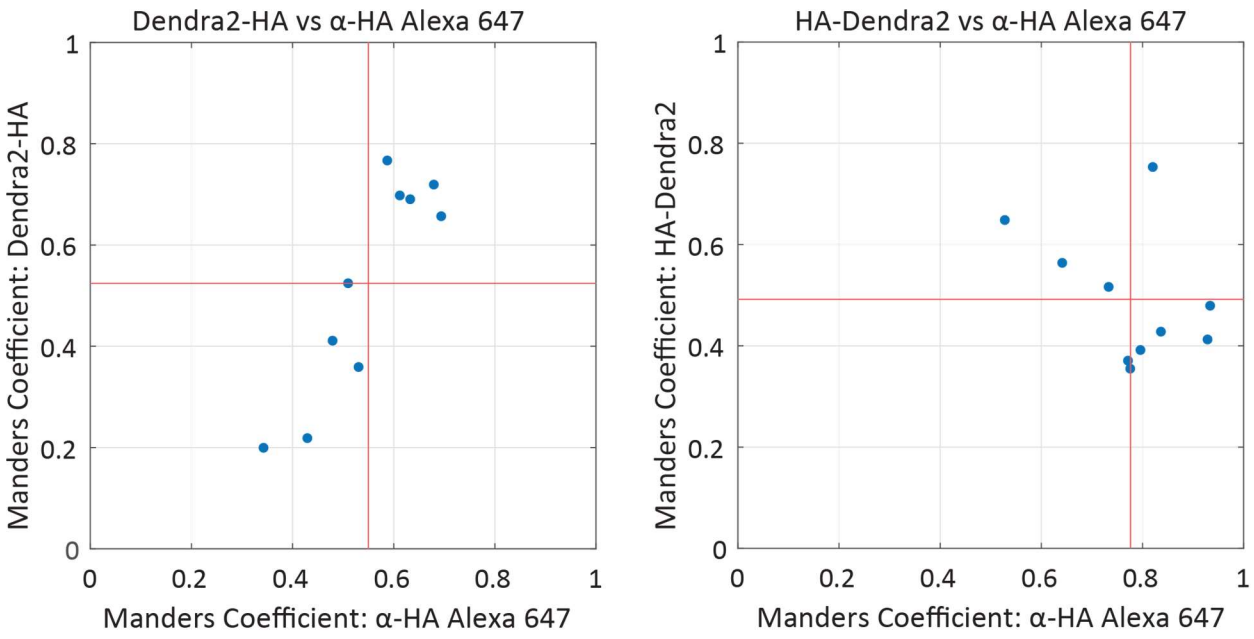

Figure 4.13: Manders colocalization coefficients (MCC) for Dendra2-HA and HA-Dendra2 vs α-HA Alexa647 FPALM renders. Mean values are indicated by the red lines on the chart. MCCs for Dendra2-HA and α-HA Alexa 647 are 0.52±0.07 and 0.55±0.04 respectively (N=10), while the coefficients for HA-Dendra2 and α-HA Alexa 647 are 0.49±0.04 and 0.78±0.04 respectively (N=10). Manders' correlation coefficient for Dendra2-HA is significantly lower than that for HA-Dendra2, likely due to the placement of the signal peptide, wherein some cases the signal peptide is being cleaved and detaching the Dendra2 from the HA.

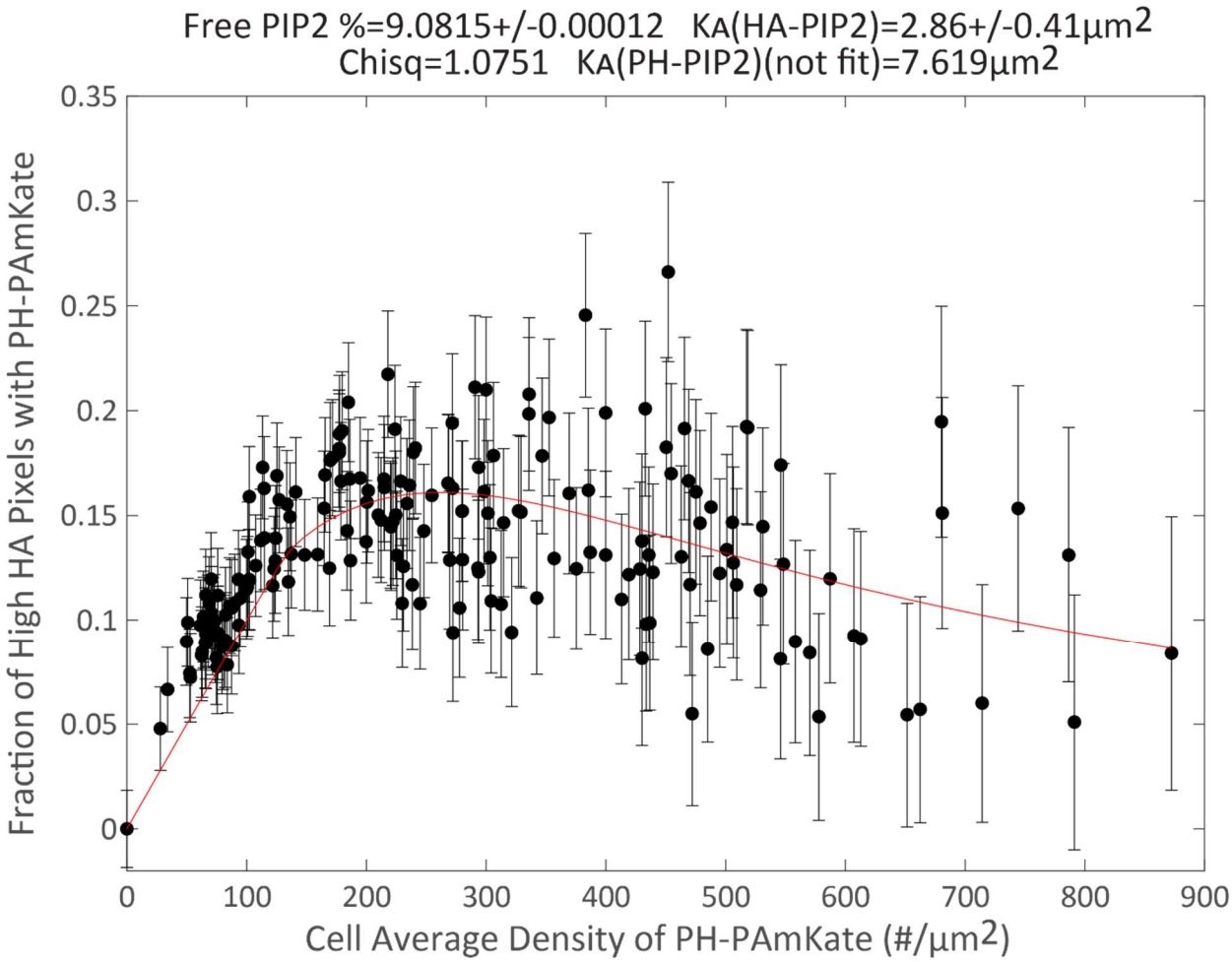

Figure 4.14: Dependence of the level of nanoscale colocalization between Dendra2-HA and PH-PAmKate as a function of the average PH-PAmKate expression level within the cell. The colocalization between Dendra2-HA and PH-PAmKate was determined from analysis of localization microscopy (FPALM) datasets imaged with TIRF and acquired in NIH3T3 fibroblast cells (n=194 cells). Localized molecular coordinates were converted into a grid plot with 10 nm x 10 nm pixels, where the pixel intensity was proportional to the number of localized molecules of a given type within that pixel; grids were then convolved with a Gaussian (width 25 nm approximately equal to the localization uncertainty, and integrated area equal to unity). The vertical axis shows f, the fraction of (10x10 nm) grid pixels with high Dendra2-HA (density greater than 4 times the cell average) which also contained PH-PAmKate (density greater than 4 times the cell average). The red line is a least-squares curve fit using a chemical equilibrium model which includes two simultaneous binding reactions: HA with free PIP2, and PH-PAmKate (PLCδ) with free PIP2. The model allows the determination of the ratio of the binding constant of HA with PIP2 to the binding constant for PH with PIP2, and the estimated fraction of PIP2 which is free (not bound by other proteins) within the plasma membrane. Since the binding constant for PH is known,[144] this analysis allows the determination of an effective binding constant for HA with PIP2. Chemical equilibrium model (not shown) and figure were developed by Dr. Samuel Hess (University of Maine) and reproduced with permission.

4.3. Discussion

4.3.1. HA CTD Mutations Alter Clustering Properties

Influenza A virus remains an ongoing public health threat with few reliable methods of treatment after infection.[5] Since the virus mutates at a rapid pace, typical preventative measures, such as vaccines, provide imperfect protection, and a universal treatment method is lacking. More information is required to better understand how the virus interacts with host cell components and to better exploit these interactions to disrupt infection.

IAV is known to require cellular components to cluster on the cell membrane in order to efficiently assemble and form viral buds;[14] however, the mechanism by which HA clusters form is currently controversial and not well understood. Yet, there have been several proposed models, including preferential partitioning of HA into lipid ordered domains (Lo), i.e. "raft" targeting, through the transmembrane and CTD regions,[19,20,204–206] induction of heterogeneities in composition through membrane curvature,[45,207,208] and reduced protein mobility from actin enrichment near the membrane.[72,73,99] However, HA is not consistently associated with lipid ordered domains in model membranes[209] and recently HA has been found to not associate with markers for lipid ordered domains at all (cholesterol, sphingolipids).[25] As such, it is unlikely that HAs clusters form solely because of association with lipid ordered regions of the membrane, and therefore new models or modifications to existing membrane models are required to explain HA clustering. Actin is also known to be capable of restricting both protein and lipid mobility when anchored to the membrane[137] and therefore, actin remains a suitable candidate for modulation of protein clustering.

The CTD comprises only 10 out of 566 total amino acids in HA (HA X-31B) but shows remarkably conserved palmitoylation sites (cysteines) throughout HA subtypes and consistently contains nearby positive charges, often arginines.[210] Since the influenza virus is under continual evolutionary pressure to mutate, the conserved portions of viral proteins are inferred to be vital to the viral replication cycle. It is

also known that the influenza virus replication is significantly inhibited by removal of certain palmitoylation sites.[42,45,46] Previous studies of HA tail palmitoylation have also shown that there is a reduction in membrane curvature when HA palmitoylation sites are removed, increasing the energy barrier for viral budding and making it more difficult for the virus to leave the cell.[45] However, it is unknown if these are the only reasons that influenza viruses prefer HA CTD palmitoylation.

Additionally, HA has been observed to colocalize with actin-rich membrane regions of the membrane with both conventional[72] and super-resolution microscopy,[73] and IAV is known to rely on the actin cytoskeletal network for efficient viral assembly of its proteins into new virions,[72,76] as well as for delivery of HA to the plasma membrane.[100,101] The positively charged residues on the tail may serve to associate the HA with certain membrane components, such as negatively charged phosphoinositide lipids, some of which are known to be involved with actin signaling. Several host cell components found in influenza virions are also part of the PIP2/PIP3 signaling interactome, such as beta-actin and ABPs cofilin-1 and profilin which are indicative of a possible interaction between viral components and phosphoinositides.[173,211] Due to Debye charge screening from free ions[212] and the abundance of charged biomacromolecules and lipids near the membrane, potential interactions between HA and inner leaflet lipids are most likely to be found in the HA CTD or otherwise very close nearby.

Previous studies using diffraction-limited and super-resolution methods have shown positive correlation of PIP2 and HA in fixed cells, while the presence of HA modulates the diffusion of GloPIP (BODIPY labeled PIP2 molecules) in living cells, suggestive of an interaction between the two.[99] Other studies have demonstrated the role of PIP2 in controlling plasma membrane association of proteins with polybasic residues and/or acylation sites.[164] We hypothesized that removal or charge reversal of positively charged regions in the CTD would reduce recruitment of PIP2 to sites of HA clustering and, if a contributing factor to clustering, would result in reduced HA cluster densities. Additionally, if the palmitoylation is important for clustering, removal of the palmitoylation sites should result in altered clustering of the HA

proteins. Since the CTD of HA contains 2-3 palmitoylation sites which are consistently accompanied by 1-2 positively charged residues,[210] coupled with the fact that HA is trimerized before reaching the membrane,[18,213] HA clusters may associate with negatively charged PIP2 headgroups through nonspecific charge-charge interactions, not unlike some other membrane proteins with polybasic amino acid residues.[164] Palmitoylation of the cysteines and the positive residues in the HA CTD may further act to stabilize the tail region close to the membrane and assist in facilitating such a nonspecific charge-charge interaction with PIP2. A non-specific interaction between the HA CTD and PIP2 (or other negatively charged lipids) could be weak, especially at distances comparable to or longer than the Debye screening distance (0.7nm in PBS for example[214]). A relatively weak, non-specific interaction would be expected to have the ability to modulate cluster properties, but not entirely disperse them.

Removal of the HA CTD palmitoylation sites (HAMAY), reversal of the tail charge (HARREQ), and a combination of these (HAREMAY) was not able to stop HA from forming clusters on the plasma membrane, although the kinds of clusters formed were significantly different from wild type HA. No significant changes were observed in the Pearson correlation coefficient (equation 2.6) between Dendra2-HA and PH-PAmKate, initially suggesting that the charges and palmitoylation sites did not affect colocalization between HA and PH-domain. However, the Pearson coefficient remains slightly positive for HA wild type, in agreement with previous observations,[99] and also for all HA mutants examined. PIP2 has also been observed to cluster in the cell membrane of cells not expressing viral proteins for other reasons,[170] so we may not expect the Pearson coefficient to be large in this case. Even though the two species display low Pearson correlation coefficients, we tested if they are spatially colocalized using the Manders' correlation coefficient (equations 2.7 and 2.8).[153] Manders' colocalization coefficients were also not significantly different between mutants, except for the HARREQ mutant, which showed a decrease in Dendra2-HA with PH-PAmKate, which suggests that PH-domain is slightly less likely to associate with Dendra2-HA for this mutant (on average over the entire cell).

The HARREQ mutant has a CTD with a net -1 charge at physiological pH. A significant 16.6%±11.6% reduction in the concentration of PH-PAmKate was observed in the vicinity of HARREQ clusters, suggesting that PIP2 is somewhat depleted in HA clusters when the positive residues are not present. Additionally, the HARREQ clusters are significantly reduced in density by 16.1%±6.3% (as measured from regionprops) and reduced in density in the central region of the RDF by 16.8%±7.1%, indicating that altering the charges, while leaving the palmitoylation sites intact, had some disruptive effect on HA clustering. HATailless shows a similar reduction in both PH domain and HA RDFs. Since PIP2 has a large variety of interaction partners within the cell,[211] we might not necessarily expect HA clusters to be entirely devoid of PIP2 if an interaction between them were disrupted. In the case of HAREMAY, we notice a 30.5%±13.5% increase in the relative density of PH-domain present in clusters coinciding with a 22.1%±3.5% decrease in HA densities compared to HAwt, which appears contradictory of a PIP2-HA interaction through the CTD. However, PH-domain is only capable of binding free PIP2,[142,143,146] so the noted increase in PH domain suggests rather that the PIP2 in HAREMAY clusters is more available to bind PH-domain, and therefore has a lower probability of being bound to other proteins within the cluster. If PIP2 interacts with the HA CTD positive residues, we might expect an increase in PH domain labeling as more of the PIP2 becomes available for binding.

Since clusters of HA are known to be far more efficient at fusion when clustered,[14] we also examined the clustering properties of the various mutants. When examining the types of clusters formed by HA and the association of clusters with PH-domain, some significant reduction in cluster densities and changes in PH domain densities under the clusters were observed. The largest differences between wild type and mutant clustering were measured when both the charge and palmitoylation sites were altered (HAREMAY), but smaller differences were found with either palmitoylation removal (HAMAY) or tail charge reversal (HARREQ). Evidently, any change at all to the charges or palmitoylation sites on the tail

causes some reduction in the central RDF region and clustering, therefore, depends somewhat on the CTD.

None of the current membrane models adequately explains HA cluster stability on the membrane or why alterations to the tail charges and/or palmitoylation sites resulted in reductions to clustering densities. Modifications to the tail clearly caused some reductions in clustering, with varying effects on the amount of underlying PH domain. Since changing the tail reduced the relative densities of clusters, it must play some role in the clustering of HA at the membrane, indicating it is unlikely that HA is purely clustered because it is targeted to certain membrane regions through the transmembrane domain. There is evidence to suggest that HA arrives at the membrane, already packed tightly into vesicles,[208] and arrives primarily through actin comet formation initiated by the WASP/PIP2 pathway.[101] HA therefore, may arrive at the membrane in clusters, with actin just underlying the membrane that would act to keep the clusters together by acting as a diffusion barrier.

However, actin filaments in the cell are highly dynamic and require constant treadmilling to maintain steady state, along with a set of actin binding proteins that help to regulate and maintain the filaments.[215] If actin helps hold HA clusters together, but there are no known interactions between HA and actin, this seeming contradiction could be explained by an intermediate, which might also be able to keep actin filaments intact. PIP2 has known binding activity to a host of ABPs, including cofilin, profilin, gelsolin, α-actinin, among other actin organizers and stabilizers.[199,200] Given the association of HA with PH-domain, we propose a model (Figure 4.15) where PIP2 is weakly drawn to the charged tails of clustered HA proteins, which in turn provide a protective effect on clusters by sequestering ABPs that would normally prompt disassembly of the actin filaments.

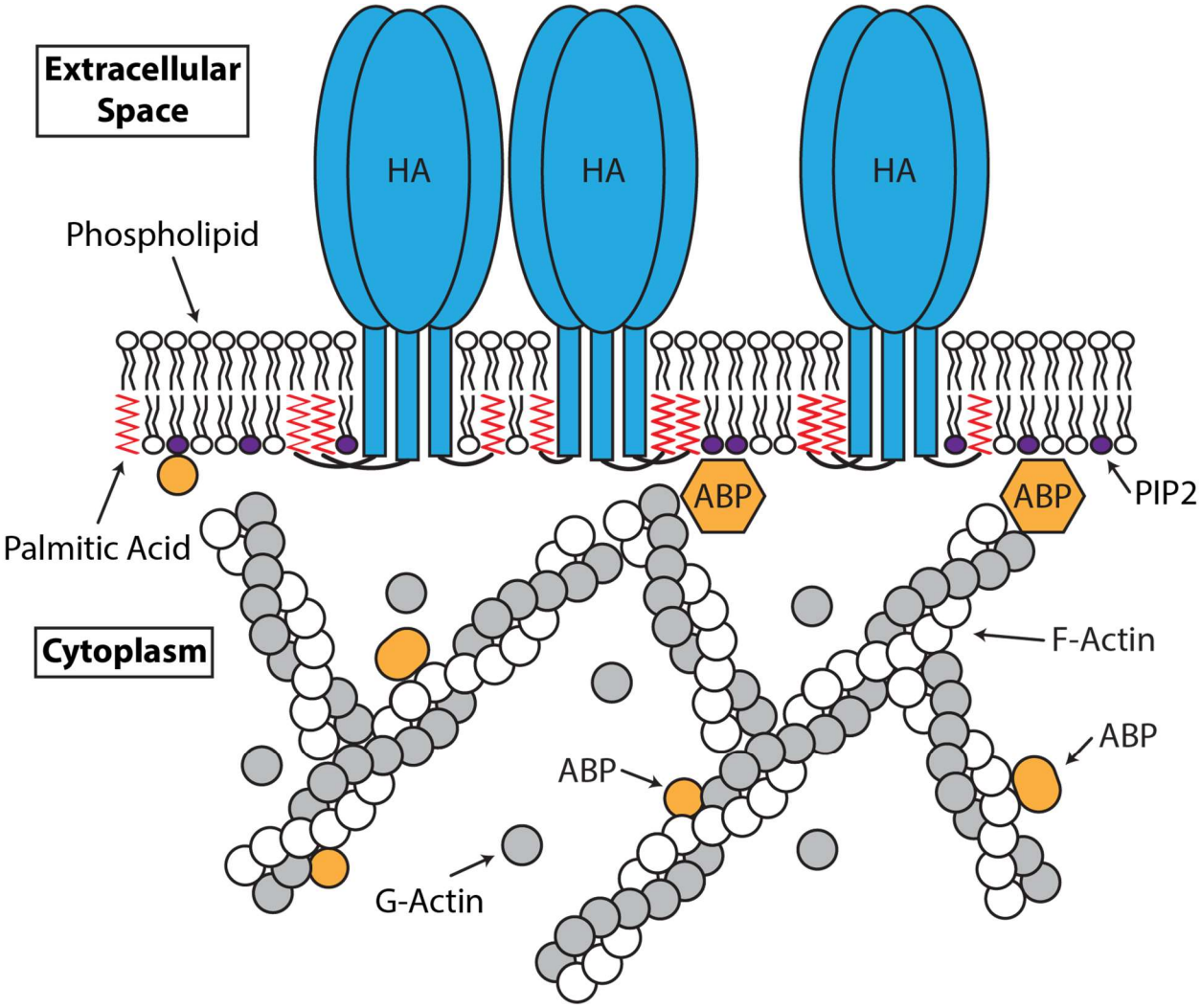

Figure 4.15: Model of HA and PIP2 co-clustering. HA colocalizes with regions of the membrane that rich in actin, which may serve as a diffusion barrier helping to keep clusters together. HA is known to arrive at the apical membrane, largely through actin comets initiated by PIP2. In this model, PIP2 is drawn to the positive residues on the palmitoylated CTD, which sequesters nearby ABPs and provides a protective effect on the actin cytoskeleton, preventing its disassembly.

4.3.2. Dendra2-HA Labeling

Since the C-terminal CTD of HA is only 10-11 amino acids in length, we decided to place the fluorescent protein label on the N-terminus of the HA protein to reduce its potential to interfere with the functionality of the tail. However, the protein contains a short 20-30 amino acid cleavable signal peptide that targets the protein to a translocon and assists with insertion of HA into the plasma membrane.[216] HA polypeptides not containing signal peptide remain largely cytoplasmic,[217] indicating that the signal peptide is essential for the membrane targeting of HA. In natural HA expression, the signal peptide resides at the N-terminus and is cleaved as part of membrane insertion. In our system, the signal peptide resides at the C-terminus of the Dendra2 protein, which itself contains no signal sequence. A study of signal peptide location on HA membrane expression found that when an N-terminus transmembrane region is present, it interferes with signal recognition and membrane insertion of proteins,[218] although our system has no preceding transmembrane region. At least one other group found no significant reliance on the position of the HA signal peptide, so long as the signal peptide sequence remained present and intact.[219]

To test if our construct was expressing properly at the membrane, we compared two fusion protein constructs where the Dendra2 gene was either N (HA-Dendra2) or C (Dendra2-HA) terminus of the HA gene and co-labeled with an antibody against the same strain of HA (X-31B). Through confocal imaging, greater membrane specific expression was observed for the HA-Dendra2 construct than the Dendra2-HA construct, although both constructs showed extensive labeling by the α-HA antibody. Pearson and Manders' coefficients for confocal data also showed significantly larger values for the HA-Dendra2 construct than the Dendra2-HA construct, which is indicative of more efficient co-labeling for the construct where the signal peptide is at the N-terminus of the protein.

However, since the sensitivity of the confocal microscope is lower than for FPALM, we decided to further examine the two constructs using FPALM microscopy. In contrast to the confocal results, FPALM datasets for the two pairs showed very similar Manders' coefficients for HA-Dendra2 with anti-HA and

Dendra2-HA with anti-HA (0.52 vs 0.49), but significantly larger value for anti-HA with HA-Dendra2 than Dendra2-HA (0.78 vs 0.55). The result from Manders' colocalization coefficients suggests that Dendra2-HA and HA-Dendra2 both have a similar chance of being found with anti-HA antibodies when co-labeled, but the anti-HA antibodies are less likely to be found with Dendra2-HA than with HA-Dendra2.

To explain why we see anti-HA more frequently colocalized with HA-Dendra2 than with Dendra2-HA, while maintaining similar Manders' coefficients for the reverse, it is possible that some fraction of the Dendra2 is being cleaved from HA when the signal peptide is located between the Dendra2 and HA proteins. This would result in two populations of HA at the membrane, one tagged with Dendra2 and one that is not. Presumably, since we see Dendra2-HA about as often with anti-HA as anti-HA with Dendra2-HA, the two populations mix together, allowing for a reasonable sampling of HA.

In future experiments involving the CTD, it may be advisable to move the sequence encoding the signal peptide to be 5' (upstream) of the fluorescent protein. In this configuration, the signal peptide may still be cleaved and facilitate typical insertion of the fusion protein into the membrane. Alternatively, different labeling methods may be facilitated, such as antibody staining or use of HaloTag[220] proteins, although these labeling methods carry drawbacks of their own.

4.3.3. PIP2 Labeling

As a lipid, PIP2 is not easily targeted directly by endogenous expression, so we used Pleckstrin Homology (PH) domain from phospholipase C δ (PLCδ) as a marker for PIP2. PH domain reversibly binds to the head group of the PIP2 lipid, as well as to the cleaved head group of PIP2, IP3.[142,143] Some concerns have been noted about using PH domain as a direct probe for PIP2 and the PH domain label has a number of imperfections that must be taken into account.[146,221] Firstly, PH domain will bind only the available, free PIP2 that it can physically reach on the PM. Although PIP2 is known to reside in cellular compartments, such as the Golgi and nucleus, PH domain has not been observed associated with these. Secondly, PIP2 and IP3 both compete for binding PH domain and previous studies have shown that IP3 binds PH domain

with higher affinity than PIP2, which can result in mislabeling of PIP2 when IP3 is nearby. In fact, PH domain from PLC δ binds IP3 with several times higher affinity than PIP2,[142,143] but IP3 is primarily a cytosolic component with nothing to anchor it to the membrane.

In plots of high HA density versus PH expression (figure 4.13), HA colocalization shows a clear downward trend as more PH domain is expressed suggestive of competition between HA and PH domain for PIP2 while in clusters. The effective binding constant was also be extracted from the fitting parameters and was found to be 2.86μm^2±0.41μm^2, smaller than the association constant for PH with PIP2. In this case, HA would bind to PIP2 about ~2.7 times weaker than PH, allowing PIP2 free to bind other interaction partners for which it has higher association constants.

4.4. New Questions

Since changes to the cytoplasmic tail had significant effects on the clustering of HA proteins, questions arise about the nature of the connection between HA clustering and the composition of the CTD. Removal of the CTD entirely or alterations to the net charge of the tail and removal of palmitoylation sites did not entirely disrupt clustering, so it is unlikely that clustering is caused solely by interactions stemming from the CTD. However, in the HAREMAY mutant, there remains one positive residue at position 565, and in the tailless mutant, an acylation site still exists just inside the TMD, so further mutations at these sites may also be worth examining. Additionally, the clustering was not wholly unaffected by these CTD changes either, suggesting that HA has multiple mechanisms that assist with clustering.

Other viral components also likely play a synergistic role in the formation of clusters, and the CTD may help coordinate interactions between other viral components. For example, NA, when expressed with HA, can accelerate the apical targeting of both proteins, but only when their CTD tails are intact.[222] The influenza viral matrix protein M1 might be involved in clustering during actual infection (where all viral proteins are overexpressed) and is known to form a helical layer on the inner membrane of IAV

particles.[223] M1 also potentially binds to the tail regions of HA and NA,[48,193,194] which is expected to have a stabilizing effect on clusters, thus clusters of viral proteins may only need to persist long enough for M1 to bind and stabilize existing clusters.

CHAPTER 5

CONCLUSION AND FUTURE DIRECTIONS

5.1. Conclusion

The influenza viral membrane protein HA forms dense nanoscale clusters on host cell PM. These clusters are closely associated with actin rich membrane regions of the PM,[72,73] but the mechanisms governing cluster formation and stability are not well understood. Actin comets have also been implicated in delivery of HA to the apical surface of infected cells,[100,101] a process initiated by PIP2. PIP2 is involved in actin regulation[199] and is exploited by proteins of other viruses, such as Ebola VP40[179–181] and HIV gag,[182–185] to assist in clustering of their membrane proteins. Diffraction limited and super-resolved multicolor FPALM images of HA and PH domain, a marker for PIP2, show a close spatial association between the two, while RDFs show that HA and PH domain follow each other spatially in clusters. Densities and areas of PH domain clusters are significantly larger and denser in the presence of high density clusters of HA, while HA clusters are significantly larger in the presence of high levels of PIP2.

HA is capable of mutating rapidly, but there are 3 cysteines and 1-2 basic residues in the CTD which remain highly conserved among HA subtypes. These cysteines are known to undergo palmitoylation, where a palmitic acid is attached to the CTD of HA, effectively pinning the tail into the membrane. Palmitoylation has been observed to assist with inducing membrane curvature[45] and , but it is unknown if serves other functions. Using a series of mutations on the CTD of HA which induce changes to either palmitoylation (HAMAY), net charge (HARE, HARREQ), or a combination of the two (HAREMAY, HATailless), we examined the effects of CTD charge and palmitoylation on the clustering properties of HA and associations with PIP2. Radial distribution functions for clusters of HA and underlying PH domain were calculated for each set of mutants and compared to wild type. Any change to the CTD resulted in significant reductions to the RDFs, but the largest changes occurred when both charge and palmitoylation were altered (HAREMAY). Changes were also observed in the PH RDFs underlying clusters of HA, where

HAREMAY and HARE mutants displayed significantly greater PH RDF values and HARREQ and HATailless were significantly decreased.

Examinations of cluster properties indicate that cluster density was significantly reduced for HARREQ, HARREQ, and HAMAY. HAREMAY also displayed changes in cluster circularity and perimeters, indicating that changes to the CTD impacted the types of clusters formed by HA. Although clusters were not eliminated by mutation of the CTD, the densities of clusters were reduced, and the types of clusters formed were altered.

5.2. Future Directions

Although changes to the HA CTD did not disrupt clustering entirely, there were significant reductions in clustering (relative to cell average) and alterations of the spatial association with PH domain. However, PH domain is only capable of binding free PIP2,[144,146] making it an indirect measure of PIP2 levels near HA clusters. More direct measurements of PIP2, through GloPIP or other prelabeled lipid, may be preferred in future experiments. Additionally, other phosphoinositides and negatively charged lipids exist in the PM, which may also be attracted to the positively charged regions of the HA tails. Other lipids in the PM also contain a negatively charged headgroups and may be involved in HA clustering. For example, phosphatidylinositol (3,4,5) triphosphate (PIP3), is known to be involved in actin regulation[224–226] and interacts with cell components isolated from purified IAV.[173]

Ca2+ oscillations have also been observed during influenza virus infections that are important for signaling RhoA, Rho kinase, phosphatidylinositol 4-phosphate 5-kinase (PIP5K) and phospholipase C.[227] Ca2+ ions are also known to be able to modulate the lateral distribution of PIP2 in the PM.[228] Since there appears to be a connection between PIP2 and HA, and a connection between Ca^{2+} and PIP2, this may warrant further investigation using calcium ionophores, which increase intracellular calcium levels and trigger PIP2 cleavage by PLCδ, or cationic compounds which may interfere with PIP2 binding HA or other membrane proteins.

CPC is a cationic compound cetylpyridinium chloride (CPC) found in consumer products, and with known antimicrobial properties. Preliminary findings treating HA-expressing NIH3T3 cells with CPC show that HA cluster densities are reduced by a factor of up to 6 times (Prakash Raut, personal communication), while the canonical PIP2-binding protein, Myristoylated Alanine-Rich C-Kinase Substrate (MARCKS) shows a CPC-dependent reduction in concentration at the plasma membrane under similar conditions (suggesting a reduction in free PIP2 in the plasma membrane) (Gosse Lab, personal communication). Since CPC is cationic, it is likely that CPC is binding partners of MARCKS in the membrane, rather than MARCKS itself, which is positively charged. MARCKS is known to sequester PIP2 through electrostatic interactions,[163,229,230] and although CPC likely has other disruptive effects at the membrane, the removal of MARCKS is highly suggestive that PIP2 interactions are disrupted by the addition of CPC. Further experiments are needed to determine if the HA cluster disruption is due entirely to CPCs interference with PIP2 or if other negatively charged players are also involved.

BIBLIOGRAPHY

1. Ginsberg, J. *et al.* Detecting influenza epidemics using search engine query data. *Nature* (2009) doi:10.1038/nature07634.

2. Fireman, B. *et al.* Influenza vaccination and mortality: Differentiating vaccine effects from bias. *Am. J. Epidemiol.* (2009) doi:10.1093/aje/kwp173.

3. Taubenberger, J. K., Reid, A. H., Janczewski, T. A. & Fanning, T. G. Integrating historical, clinical and molecular genetic data in order to explain the origin and virulence of the 1918 Spanish influenza virus. in *Philosophical Transactions of the Royal Society B: Biological Sciences* (2001). doi:10.1098/rstb.2001.1020.

4. Dharan, N. J. *et al.* Infections with oseltamivir-resistant influenza A(H1N1) virus in the united states. *JAMA - J. Am. Med. Assoc.* (2009) doi:10.1001/jama.2009.294.

5. Michiels, B., van Puyenbroeck, K., Verhoeven, V., Vermeire, E. & Coenen, S. The Value of Neuraminidase Inhibitors for the Prevention and Treatment of Seasonal Influenza: A Systematic Review of Systematic Reviews. *PLoS ONE* (2013) doi:10.1371/journal.pone.0060348.

6. CDC. Summary of the 2014-2015 Influenza Season. https://www.cdc.gov/flu/pastseasons/1415season.htm (2015).

7. Norkin, L. *Virology: Molecular Biology and Pathogenesis*. (ASM Press, 2009).

8. Klemm, C., Boergeling, Y., Ludwig, S. & Ehrhardt, C. Immunomodulatory Nonstructural Proteins of Influenza A Viruses. *Trends in Microbiology* (2018) doi:10.1016/j.tim.2017.12.006.

9. Gomez-Puertas, P., Albo, C., Perez-Pastrana, E., Vivo, A. & Portela, A. Influenza Virus Matrix Protein Is the Major Driving Force in Virus Budding. *J. Virol.* (2000) doi:10.1128/jvi.74.24.11538-11547.2000.

10. Dahmani, I., Ludwig, K. & Chiantia, S. Influenza A matrix protein M1 induces lipid membrane deformation via protein multimerization. *Biosci. Rep.* (2019) doi:10.1042/BSR20191024.

11. Latham, T. & Galarza, J. M. Formation of Wild-Type and Chimeric Influenza Virus-Like Particles following Simultaneous Expression of Only Four Structural Proteins. *J. Virol.* (2001) doi:10.1128/jvi.75.13.6154-6165.2001.

12. Palese, P., Tobita, K., Ueda, M. & Compans, R. W. Characterization of temperature sensitive influenza virus mutants defective in neuraminidase. *Virology* (1974) doi:10.1016/0042-6822(74)90276-1.

13. Rossman, J. S., Jing, X., Leser, G. P. & Lamb, R. A. Influenza Virus M2 Protein Mediates ESCRT-Independent Membrane Scission. *Cell* (2010) doi:10.1016/j.cell.2010.08.029.

14. Takeda, M., Leser, G. P., Russell, C. J. & Lamb, R. A. Influenza virus hemagglutinin concentrates in lipid raft microdomains for efficient viral fusion. *Proc. Natl. Acad. Sci.* **100**, 14610–14617 (2003).

15. Ellens, H. *et al.* Fusion of Influenza Hemagglutinin-Expressing Fibroblasts with Glycophorin-Bearing Liposomes: Role of Hemagglutinin Surface Density. *Biochemistry* (1990) doi:10.1021/bi00493a027.

16. Hess, S. T. *et al.* Dynamic clustered distribution of hemagglutinin resolved at 40 nm in living cell membranes discriminates between raft theories. *Proc. Natl. Acad. Sci. U. S. A.* (2007) doi:10.1073/pnas.0708066104.

17. Marjuki, H. *et al.* Membrane accumulation of influenza A virus hemagglutinin triggers nuclear export of the viral genome via protein kinase Cα-mediated activation of ERK signaling. *J. Biol. Chem.* (2006) doi:10.1074/jbc.M510233200.

18. Copeland, C. S. *et al.* Folding, trimerization, and transport are sequential events in the biogenesis of influenza virus hemagglutinin. *Cell* (1988) doi:10.1016/0092-8674(88)90381-9.

19. Fiedler, K., Kurzchalia, T. V., Simons, K. & Kobayashi, T. Glycosphingolipid-Enriched, Detergent-Insoluble Complexes in Protein Sorting in Epithelial Cells. *Biochemistry* (1993) doi:10.1021/bi00076a009.

20. Scheiffele, P., Rietveld, A., Wilk, T. & Simons, K. Influenza viruses select ordered lipid domains during budding from the plasma membrane. *J. Biol. Chem.* (1999) doi:10.1074/jbc.274.4.2038.

21. Shvartsman, D. E., Kotler, M., Tall, R. D., Roth, M. G. & Henis, Y. I. Differently anchored influenza hemagglutinin mutants display distinct interaction dynamics with mutual rafts. *J. Cell Biol.* (2003) doi:10.1083/jcb.200308142.

22. Ge, M. & Freed, J. H. Two conserved residues are important for inducing highly ordered membrane domains by the transmembrane domain of influenza hemagglutinin. *Biophys. J.* (2011) doi:10.1016/j.bpj.2010.11.014.

23. Simons, K. & Ikonen, E. Functional rafts in cell membranes. *Nature* (1997) doi:10.1038/42408.

24. Hess, S. T. *et al.* Quantitative electron microscopy and fluorescence spectroscopy of the membrane distribution of influenza hemagglutinin. *J. Cell Biol.* (2005) doi:10.1083/jcb.200412058.

25. Wilson, R. L. *et al.* Hemagglutinin clusters in the plasma membrane are not enriched with cholesterol and sphingolipids. *Biophys. J.* (2015) doi:10.1016/j.bpj.2015.02.026.

26. Breen, M., Nogales, A., Baker, S. F. & Martínez-Sobrido, L. Replication-competent influenza a viruses expressing reporter genes. *Viruses* (2016) doi:10.3390/v8070179.

27. Chao, C. C., Bird, P., Gething, M. J. & Sambrook, J. Posttranslational translocation of influenza virus hemagglutinin across microsomal membranes. *Mol. Cell. Biol.* (2015) doi:10.1128/mcb.7.10.3842.

28. Yewdell, J. W., Yellen, A. & Bächi, T. Monoclonal antibodies localize events in the folding, assembly, and intracellular transport of the influenza virus hemagglutinin glycoprotein. *Cell* (1988) doi:10.1016/0092-8674(88)90426-6.

29. Russ, G., Bennink, J. R., Bächi, T. & Yewdell, J. W. Influenza virus hemagglutinin trimers and

monomers maintain distinct biochemical modifications and intracellular distribution in brefeldin A-treated cells. *Mol. Biol. Cell* (1991) doi:10.1091/mbc.2.7.549.

30. Chaipan, C. *et al.* Proteolytic Activation of the 1918 Influenza Virus Hemagglutinin. *J. Virol.* (2009) doi:10.1128/jvi.02205-08.

31. LeBouder, F. *et al.* Annexin II Incorporated into Influenza Virus Particles Supports Virus Replication by Converting Plasminogen into Plasmin. *J. Virol.* (2008) doi:10.1128/jvi.00246-08.

32. Bottcher, E. *et al.* Proteolytic Activation of Influenza Viruses by Serine Proteases TMPRSS2 and HAT from Human Airway Epithelium. *J. Virol.* (2006) doi:10.1128/jvi.01118-06.

33. Bottcher-Friebertshauser, E. *et al.* Cleavage of Influenza Virus Hemagglutinin by Airway Proteases TMPRSS2 and HAT Differs in Subcellular Localization and Susceptibility to Protease Inhibitors. *J. Virol.* (2010) doi:10.1128/jvi.00140-10.

34. Goto, H. & Kawaoka, Y. A novel mechanism for the acquisition of virulence by a human influenza A virus. *Proc. Natl. Acad. Sci. U. S. A.* (1998) doi:10.1073/pnas.95.17.10224.

35. Lazarowitz, S. G., Goldberg, A. R. & Choppin, P. W. Proteolytic cleavage by plasmin of the HA polypeptide of influenza virus: Host cell activation of serum plasminogen. *Virology* (1973) doi:10.1016/0042-6822(73)90296-1.

36. Tse, L. V., Marcano, V. C., Huang, W., Pocwierz, M. S. & Whittaker, G. R. Plasmin-Mediated Activation of Pandemic H1N1 Influenza Virus Hemagglutinin Is Independent of the Viral Neuraminidase. *J. Virol.* (2013) doi:10.1128/jvi.00210-13.

37. Zhang, Y. *et al.* A Single Amino Acid at the Hemagglutinin Cleavage Site Contributes to the Pathogenicity and Neurovirulence of H5N1 Influenza Virus in Mice. *J. Virol.* (2012) doi:10.1128/jvi.07142-11.

38. Benton, D. J. *et al.* Influenza hemagglutinin membrane anchor. *Proc. Natl. Acad. Sci. U. S. A.* (2018) doi:10.1073/pnas.1810927115.

39. Pettersen, E. F. *et al.* UCSF Chimera - A visualization system for exploratory research and analysis. *J. Comput. Chem.* (2004) doi:10.1002/jcc.20084.

40. Veit, M. & Schmidt, M. F. G. Timing of palmitoylation of influenza virus hemagglutinin. *FEBS Lett.* (1993) doi:10.1016/0014-5793(93)80812-9.

41. Linder, M. E. & Deschenes, R. J. Palmitoylation: Policing protein stability and traffic. *Nature Reviews Molecular Cell Biology* (2007) doi:10.1038/nrm2084.

42. Veit, M. & Schmidt, M. F. G. Palmitoylation of Influenza virus proteins. *Berliner und Munchener Tierarztliche Wochenschrift* (2006).

43. Kordyukova, L. *et al.* Influenza a Hemagglutinin C-terminal Anchoring Peptide: Identification and Mass Spectrometric Study. *Protein Pept. Lett.* (2005) doi:10.2174/0929866043406850.

44. Kordyukova, L. V., Serebryakova, M. V., Baratova, L. A. & Veit, M. S Acylation of the Hemagglutinin of Influenza Viruses: Mass Spectrometry Reveals Site-Specific Attachment of Stearic Acid to a Transmembrane Cysteine. *J. Virol.* (2008) doi:10.1128/jvi.00704-08.

45. Chlanda, P. *et al.* Palmitoylation Contributes to Membrane Curvature in Influenza A Virus Assembly and Hemagglutinin-Mediated Membrane Fusion. *J. Virol.* (2017) doi:10.1128/jvi.00947-17.

46. Chen, B. J., Takeda, M. & Lamb, R. A. Influenza Virus Hemagglutinin (H3 Subtype) Requires Palmitoylation of Its Cytoplasmic Tail for Assembly: M1 Proteins of Two Subtypes Differ in Their Ability To Support Assembly. *J. Virol.* (2005) doi:10.1128/jvi.79.21.13673-13684.2005.

47. Zurcher, T., Luo, G. & Palese, P. Mutations at palmitylation sites of the influenza virus hemagglutinin affect virus formation. *J. Virol.* (1994) doi:10.1128/jvi.68.9.5748-5754.1994.

48. Jin, H., Leser, G. P., Zhang, J. & Lamb, R. A. Influenza virus hemagglutinin and neuraminidase cytoplasmic tails control particle shape. *EMBO J.* (1997) doi:10.1093/emboj/16.6.1236.

49. Rayleigh. XXXI. Investigations in optics, with special reference to the spectroscope . *London, Edinburgh, Dublin Philos. Mag. J. Sci.* (1879) doi:10.1080/14786447908639684.

50. Shimomura, O., Johnson, F. H. & Saiga, Y. Extraction, Purification and Properties of Aequorin, a Bioluminescent Protein from the Luminous Hydromedusan,Aequorea. *J. Cell. Comp. Physiol.* (1962) doi:10.1002/jcp.1030590302.

51. Tsien, R. Y. THE GREEN FLUORESCENT PROTEIN. *Annu. Rev. Biochem.* (1998) doi:10.1146/annurev.biochem.67.1.509.

52. Chalfie, M., Tu, Y., Euskirchen, G., Ward, W. W. & Prasher, D. C. Green fluorescent protein as a marker for gene expression. *Science (80-.).* (1994) doi:10.1126/science.8303295.

53. Toseland, C. P. Fluorescent labeling and modification of proteins. *Journal of Chemical Biology* (2013) doi:10.1007/s12154-013-0094-5.

54. Pawley, J. B. *Handbook of biological confocal microscopy: Third edition*. *Handbook of Biological Confocal Microscopy: Third Edition* (2006). doi:10.1007/978-0-387-45524-2.

55. Thompson, R. E., Larson, D. R. & Webb, W. W. Precise nanometer localization analysis for individual fluorescent probes. *Biophys. J.* (2002) doi:10.1016/S0006-3495(02)75618-X.

56. Mortensen, K. I., Churchman, L. S., Spudich, J. A. & Flyvbjerg, H. Optimized localization analysis for single-molecule tracking and super-resolution microscopy. *Nat. Methods* (2010) doi:10.1038/nmeth.1447.

57. Hess, S. T., Girirajan, T. P. K. & Mason, M. D. Ultra-high resolution imaging by fluorescence photoactivation localization microscopy. *Biophys. J.* (2006) doi:10.1529/biophysj.106.091116.

58. Betzig, E. *et al.* Proteins at Nanometer Resolution. *Science (80-.).* (2006) doi:10.1126/science.1127344.

59. Rust, M. J., Bates, M. & Zhuang, X. Sub-diffraction-limit imaging by stochastic optical reconstruction microscopy (STORM). *Nat. Methods* (2006) doi:10.1038/nmeth929.

60. Gould, T. J., Verkhusha, V. V. & Hess, S. T. Imaging biological structures with fluorescence photoactivation localization microscopy. *Nat. Protoc.* (2009) doi:10.1038/nprot.2008.246.

61. Banterle, N., Bui, K. H., Lemke, E. A. & Beck, M. Fourier ring correlation as a resolution criterion for super-resolution microscopy. *J. Struct. Biol.* (2013) doi:10.1016/j.jsb.2013.05.004.

62. Pennacchietti, F., Gould, T. J. & Hess, S. T. The Role of Probe Photophysics in Localization-Based Superresolution Microscopy. *Biophys. J.* (2017) doi:10.1016/j.bpj.2017.08.054.

63. Gunewardene, M. S. *et al.* Superresolution imaging of multiple fluorescent proteins with highly overlapping emission spectra in living cells. *Biophys. J.* (2011) doi:10.1016/j.bpj.2011.07.049.

64. Bates, M., Huang, B., Dempsey, G. T. & Zhuang, X. Multicolor super-resolution imaging with photo-switchable fluorescent probes. *Science (80-.).* (2007) doi:10.1126/science.1146598.

65. Bossi, M. *et al.* Multicolor far-field fluorescence nanoscopy through isolated detection of distinct molecular species. *Nano Lett.* (2008) doi:10.1021/nl801471d.

66. Kim, D., Curthoys, N. M., Parent, M. T. & Hess, S. T. Bleed-through correction for rendering and correlation analysis in multi-colour localization microscopy. *J. Opt. (United Kingdom)* (2013) doi:10.1088/2040-8978/15/9/094011.

67. Pearson, K. LIII. *On lines and planes of closest fit to systems of points in space*. *London, Edinburgh, Dublin Philos. Mag. J. Sci.* (1901) doi:10.1080/14786440109462720.

68. Huang, B., Wang, W., Bates, M. & Zhuang, X. Three-dimensional super-resolution imaging by stochastic optical reconstruction microscopy. *Science (80-.).* (2008) doi:10.1126/science.1153529.

69. Lehmann, M. J., Sherer, N. M., Marks, C. B., Pypaert, M. & Mothes, W. Actin- and myosin-driven movement of viruses along filopodia precedes their entry into cells. *J. Cell Biol.* (2005) doi:10.1083/jcb.200503059.

70. Spear, M. & Wu, Y. Viral exploitation of actin: Force-generation and scaffolding functions in viral infection. *Virologica Sinica* (2014) doi:10.1007/s12250-014-3476-0.

71. Taylor, M. P., Koyuncu, O. O. & Enquist, L. W. Subversion of the actin cytoskeleton during viral infection. *Nature Reviews Microbiology* (2011) doi:10.1038/nrmicro2574.

72. Simpson-Holley, M. *et al.* A Functional Link between the Actin Cytoskeleton and Lipid Rafts during Budding of Filamentous Influenza Virions. *Virology* **301**, 212–225 (2002).

73. Gudheti, M. V. *et al.* Actin mediates the nanoscale membrane organization of the clustered membrane protein influenza hemagglutinin. *Biophys. J.* (2013) doi:10.1016/j.bpj.2013.03.054.

74. Avalos, R. T., Yu, Z. & Nayak, D. P. Association of influenza virus NP and M1 proteins with cellular

cytoskeletal elements in influenza virus-infected cells. *J. Virol.* (1997) doi:10.1128/jvi.71.4.2947-2958.1997.

75. Gujuluva, C. N., Kundu, A., Murti, K. G. & Nayak, D. P. Abortive Replication of Influenza Virus A/WSN/33 in HeLa229 Cells: Defective Viral Entry and Budding Processes. *Virology* (1994) doi:10.1006/viro.1994.1563.

76. Kumakura, M., Kawaguchi, A. & Nagata, K. Actin-myosin network is required for proper assembly of influenza virus particles. *Virology* (2015) doi:10.1016/j.virol.2014.12.016.

77. Sharma, S. *et al.* Influenza A viral nucleoprotein interacts with cytoskeleton scaffolding protein α-actinin-4 for viral replication. *FEBS J.* (2014) doi:10.1111/febs.12828.

78. Avilov, S. V., Moisy, D., Naffakh, N. & Cusack, S. Influenza A virus progeny vRNP trafficking in live infected cells studied with the virus-encoded fluorescently tagged PB2 protein. *Vaccine* (2012) doi:10.1016/j.vaccine.2012.09.077.

79. Morone, N. *et al.* Three-dimensional reconstruction of the membrane skeleton at the plasma membrane interface by electron tomography. *J. Cell Biol.* (2006) doi:10.1083/jcb.200606007.

80. Zigmond, S. H. Formin-induced nucleation of actin filaments. *Current Opinion in Cell Biology* (2004) doi:10.1016/j.ceb.2003.10.019.

81. Pring, M., Evangelista, M., Boone, C., Yang, C. & Zigmond, S. H. Mechanism of formin-induced nucleation of actin filaments. *Biochemistry* (2003) doi:10.1021/bi026520j.

82. Paul, A. S. & Pollard, T. D. Energetic requirements for processive elongation of actin filaments by FH1FH2-formins. *J. Biol. Chem.* (2009) doi:10.1074/jbc.M808587200.

83. Otomo, T. *et al.* Structural basis of actin filament nucleation and processive capping by a formin homology 2 domain. *Nature* (2005) doi:10.1038/nature03251.

84. Higgs, H. N., Blanchoin, L. & Pollard, T. D. Influence of the C terminus of Wiskott-Aldrich syndrome protein (WASp) and the Arp2/3 complex on actin polymerization. *Biochemistry* (1999) doi:10.1021/bi991843+.

85. Mullins, R. D., Heuser, J. A. & Pollard, T. D. The interaction of Arp2/3 complex with actin: Nucleation, high affinity pointed end capping, and formation of branching networks of filaments. *Proc. Natl. Acad. Sci. U. S. A.* (1998) doi:10.1073/pnas.95.11.6181.

86. Ahuja, R. *et al.* Cordon-Bleu Is an Actin Nucleation Factor and Controls Neuronal Morphology. *Cell* (2007) doi:10.1016/j.cell.2007.08.030.

87. Chereau, D. *et al.* Leiomodin is an actin filament nucleator in muscle cells. *Science (80-.).* (2008) doi:10.1126/science.1155313.

88. Kerkhoff, E. Cellular functions of the Spir actin-nucleation factors. *Trends in Cell Biology* (2006) doi:10.1016/j.tcb.2006.07.005.

89. Carlsson, L., Nyström, L. E., Sundkvist, I., Markey, F. & Lindberg, U. Actin polymerizability is influenced by profilin, a low molecular weight protein in non-muscle cells. *J. Mol. Biol.* (1977) doi:10.1016/0022-2836(77)90166-8.

90. Ichetovkin, I., Han, J., Pang, K. M., Knecht, D. A. & Condeelis, J. S. Actin filaments are severed by both native and recombinant Dictyostelium cofilin but to different extents. *Cell Motil. Cytoskeleton* (2000) doi:10.1002/(SICI)1097-0169(200004)45:4<293::AID-CM5>3.0.CO;2-1.

91. Ichetovkin, I., Grant, W. & Condeelis, J. Cofilin produces newly polymerized actin filaments that are preferred for dendritic nucleation by the Arp2/3 complex. *Curr. Biol.* (2002) doi:10.1016/S0960-9822(01)00629-7.

92. Andrianantoandro, E. & Pollard, T. D. Mechanism of Actin Filament Turnover by Severing and Nucleation at Different Concentrations of ADF/Cofilin. *Mol. Cell* (2006) doi:10.1016/j.molcel.2006.08.006.

93. Xu, J., Wirtz, D. & Pollard, T. D. Dynamic cross-linking by α-actinin determines the mechanical properties of actin filament networks. *J. Biol. Chem.* (1998) doi:10.1074/jbc.273.16.9570.

94. Khurana, S. & George, S. P. The role of actin bundling proteins in the assembly of filopodia in epithelial cells. *Cell Adhesion and Migration* (2011) doi:10.4161/cam.5.5.17644.

95. Lee Sweeney, H. & Holzbaur, E. L. F. Motor proteins. *Cold Spring Harb. Perspect. Biol.* (2018) doi:10.1101/cshperspect.a021931.

96. DePina, A. S. & Langford, G. M. Vesicle transport: The role of actin filaments and myosin motors. *Microsc. Res. Tech.* (1999) doi:10.1002/(SICI)1097-0029(19991015)47:2<93::AID-JEMT2>3.0.CO;2-P.

97. Soares E Silva, M. *et al.* Active multistage coarsening of actin networks driven by myosin motors. *Proc. Natl. Acad. Sci. U. S. A.* (2011) doi:10.1073/pnas.1016616108.

98. Pollard, T. D. Actin and actin-binding proteins. *Cold Spring Harb. Perspect. Biol.* (2016) doi:10.1101/cshperspect.a018226.

99. Curthoys, N. M. *et al.* Influenza Hemagglutinin Modulates Phosphatidylinositol 4,5-Bisphosphate Membrane Clustering. *Biophys. J.* (2019) doi:10.1016/j.bpj.2019.01.017.

100. Guerriero, C. J., Weixel, K. M., Bruns, J. R. & Weisz, O. A. Phosphatidylinositol 5-kinase stimulates apical biosynthetic delivery via an Arp2/3-dependent mechanism. *J. Biol. Chem.* (2006) doi:10.1074/jbc.M601239200.

101. Rozelle, A. L. *et al.* Phosphatidylinositol 4,5-bisphosphate induces actin-based movement of raft-enriched vesicles through WASP-Arp2/3. *Curr. Biol.* (2000) doi:10.1016/S0960-9822(00)00384-5.

102. Singer, S. J. & Nicolson, G. L. The fluid mosaic model of the structure of cell membranes. *Science (80-.).* (1972) doi:10.1126/science.175.4023.720.

103. SINGER, S. J. THE MOLECULAR ORGANIZATION OF BIOLOGICAL MEMBRANES. in *Structure and Function of Biological Membranes* (1971). doi:10.1016/b978-0-12-598650-2.50009-0.

104. Moore, B. M., Lentz, B. R. & Meissner, G. Effects of Sarcoplasmic Reticulum Ca2+-ATPase on Phospholipid Bilayer Fluidity: Boundary Lipid. *Biochemistry* (1978) doi:10.1021/bi00617a026.

105. Karnovsky, M. J., Kleinfeld, A. M., Hoover, R. L. & Klausner, R. D. The concept of lipid domains in membranes. *J. Cell Biol.* (1982) doi:10.1083/jcb.94.1.1.

106. Simons, K. & Van Meer, G. Lipid Sorting in Epithelial Cells. *Biochemistry* (1988) doi:10.1021/bi00417a001.

107. Simons, K. & Wandinger-Ness, A. Polarized sorting in epithelia. *Cell* (1990) doi:10.1016/0092-8674(90)90357-K.

108. Brown, D. A. & Rose, J. K. Sorting of GPI-anchored proteins to glycolipid-enriched membrane subdomains during transport to the apical cell surface. *Cell* (1992) doi:10.1016/0092-8674(92)90189-J.

109. Finkelstein, A. & Cass, A. Effect of cholesterol on the water permeability of thin lipid membranes [42]. *Nature* (1967) doi:10.1038/216717a0.

110. Brown, D. A. & London, E. Structure and origin of ordered lipid domains in biological membranes. *Journal of Membrane Biology* (1998) doi:10.1007/s002329900397.

111. Simons, K. & Gerl, M. J. Revitalizing membrane rafts: New tools and insights. *Nature Reviews Molecular Cell Biology* (2010) doi:10.1038/nrm2977.

112. Honerkamp-Smith, A. R., Veatch, S. L. & Keller, S. L. An introduction to critical points for biophysicists; observations of compositional heterogeneity in lipid membranes. *Biochimica et Biophysica Acta - Biomembranes* (2009) doi:10.1016/j.bbamem.2008.09.010.

113. Veatch, S. L. *et al.* Critical fluctuations in plasma membrane vesicles. *ACS Chem. Biol.* (2008) doi:10.1021/cb800012x.

114. Tanford, C. The hydrophobic effect and the organization of living matter. *Science* (1978) doi:10.1126/science.653353.

115. Veatch, S. L., Gawrisch, K. & Keller, S. L. Closed-loop miscibility gap and quantitative tie-lines in ternary membranes containing diphytanoyl PC. *Biophys. J.* (2006) doi:10.1529/biophysj.105.080283.

116. Veatch, S. L. & Keller, S. L. A closer look at the canonical 'raft mixture' in model membrane studies. *Biophysical Journal* (2003) doi:10.1016/S0006-3495(03)74891-7.

117. Veatch, S. L., Polozov, I. V., Gawrisch, K. & Keller, S. L. Liquid Domains in Vesicles Investigated by NMR and Fluorescence Microscopy. *Biophys. J.* (2004) doi:10.1016/S0006-3495(04)74342-8.

118. Veatch, S. L. & Keller, S. L. Miscibility phase diagrams of giant vesicles containing sphingomyelin. *Phys. Rev. Lett.* (2005) doi:10.1103/PhysRevLett.94.148101.

119. Veatch, S. L. & Keller, S. L. Separation of Liquid Phases in Giant Vesicles of Ternary Mixtures of Phospholipids and Cholesterol. *Biophys. J.* (2003) doi:10.1016/S0006-3495(03)74726-2.

120. Baumgart, T., Hunt, G., Farkas, E. R., Webb, W. W. & Feigenson, G. W. Fluorescence probe partitioning between Lo/Ld phases in lipid membranes. *Biochim. Biophys. Acta - Biomembr.* (2007) doi:10.1016/j.bbamem.2007.05.012.

121. Dietrich, C. *et al.* Lipid rafts reconstituted in model membranes. *Biophys. J.* (2001) doi:10.1016/S0006-3495(01)76114-0.

122. Korlach, J., Schwille, P., Webb, W. W. & Feigenson, G. W. Characterization of lipid bilayer phases by confocal microscopy and fluorescence correlation spectroscopy. *Proc. Natl. Acad. Sci. U. S. A.* (1999) doi:10.1073/pnas.96.15.8461.

123. Almeida, P. F. F., Pokorny, A. & Hinderliter, A. Thermodynamics of membrane domains. *Biochimica et Biophysica Acta - Biomembranes* (2005) doi:10.1016/j.bbamem.2005.12.004.

124. Bagatolli, L. A. & Gratton, E. Two-photon fluorescence microscopy observation of shape changes at the phase transition in phospholipid giant unilamellar vesicles. *Biophys. J.* (1999) doi:10.1016/S0006-3495(99)77050-5.

125. Bagatolli, L. A. & Gratton, E. Two photon fluorescence microscopy of coexisting lipid domains in giant unilamellar vesicles of binary phospholipid mixtures. *Biophys. J.* (2000) doi:10.1016/S0006-3495(00)76592-1.

126. Bagatolli, L., Gratton, E., Khan, T. K. & Chong, P. L. G. Two-photon fluorescence microscopy studies of bipolar tetraether giant liposomes from thermoacidophilic archaebacteria Sulfolobus acidocaldarius. *Biophys. J.* (2000) doi:10.1016/S0006-3495(00)76303-X.

127. Baumgart, T. *et al.* Large-scale fluid/fluid phase separation of proteins and lipids in giant plasma membrane vesicles. *Proc. Natl. Acad. Sci. U. S. A.* (2007) doi:10.1073/pnas.0611357104.

128. Bagatolli, L. A., Sanchez, S. A., Hazlett, T. & Gratton, E. Giant vesicles, laurdan, and two-photon fluorescence microscopy: Evidence of lipid lateral separation in bilayers. *Methods Enzymol.* (2003) doi:10.1016/S0076-6879(03)60124-2.

129. Baumgart, T., Hess, S. T. & Webb, W. W. Imaging coexisting fluid domains in biomembrane models coupling curvature and line tension. *Nature* (2003) doi:10.1038/nature02013.

130. Sevcsik, E. *et al.* GPI-anchored proteins do not reside in ordered domains in the live cell plasma membrane. *Nat. Commun.* (2015) doi:10.1038/ncomms7969.

131. Anderson, R. G. W. & Jacobson, K. Cell biology: A role for lipid shells in targeting proteins to caveolae, rafts, and other lipid domains. *Science* (2002) doi:10.1126/science.1068886.

132. Kusumi, A. & Sako, Y. Cell surface organization by the membrane skeleton. *Curr. Opin. Cell Biol.* (1996) doi:10.1016/S0955-0674(96)80036-6.

133. Sako, Y. & Kusumi, A. Compartmentalized structure of the plasma membrane for receptor movements as revealed by a nanometer-level motion analysis. *J. Cell Biol.* (1994) doi:10.1083/jcb.125.6.1251.

134. Kusumi, A. *et al.* Dynamic Organizing Principles of the Plasma Membrane that Regulate Signal Transduction: Commemorating the Fortieth Anniversary of Singer and Nicolson's Fluid-Mosaic Model. *Annu. Rev. Cell Dev. Biol.* (2012) doi:10.1146/annurev-cellbio-100809-151736.

135. Fujiwara, T., Ritchie, K., Murakoshi, H., Jacobson, K. & Kusumi, A. Phospholipids undergo hop diffusion in compartmentalized cell membrane. *J. Cell Biol.* (2002) doi:10.1083/jcb.200202050.

136. Sadegh, S., Higgins, J. L., Mannion, P. C., Tamkun, M. M. & Krapf, D. Plasma membrane is compartmentalized by a self-similar cortical actin meshwork. *Phys. Rev. X* (2017) doi:10.1103/PhysRevX.7.011031.

137. Heinemann, F., Vogel, S. K. & Schwille, P. Lateral membrane diffusion modulated by a minimal actin cortex. *Biophys. J.* (2013) doi:10.1016/j.bpj.2013.02.042.

138. Sharma, P. *et al.* Nanoscale Organization of Multiple GPI-Anchored Proteins in Living Cell Membranes. *Cell* (2004) doi:10.1016/S0092-8674(04)00167-9.

139. Goswami, D. *et al.* Nanoclusters of GPI-Anchored Proteins Are Formed by Cortical Actin-Driven Activity. *Cell* (2008) doi:10.1016/j.cell.2008.11.032.

140. Gowrishankar, K. *et al.* Active remodeling of cortical actin regulates spatiotemporal organization of cell surface molecules. *Cell* (2012) doi:10.1016/j.cell.2012.05.008.

141. Gurskaya, N. G. *et al.* Engineering of a monomeric green-to-red photoactivatable fluorescent protein induced by blue light. *Nat. Biotechnol.* (2006) doi:10.1038/nbt1191.

142. Szentpetery, Z., Balla, A., Kim, Y. J., Lemmon, M. A. & Balla, T. Live cell imaging with protein domains capable of recognizing phosphatidylinositol 4,5-bisphosphate; a comparative study. *BMC Cell Biol.* (2009) doi:10.1186/1471-2121-10-67.

143. Flesch, F. M., Yu, J. W., Lemmon, M. A. & Burger, K. N. J. Membrane activity of the phospholipase C-δ1 pleckstrin homology (PH) domain. *Biochem. J.* (2005) doi:10.1042/BJ20041721.

144. Kavran, J. M. *et al.* Specificity and promiscuity in phosphoinositide binding by pleckstrin homology domains. *J. Biol. Chem.* (1998) doi:10.1074/jbc.273.46.30497.

145. Ji, C., Zhang, Y., Xu, P., Xu, T. & Lou, X. Nanoscale landscape of phosphoinositides revealed by specific pleckstrin homology (PH) domains using single-molecule superresolution imaging in the plasma membrane. *J. Biol. Chem.* (2015) doi:10.1074/jbc.M115.663013.

146. Irvine, R. Inositol lipids: To PHix or not to PHix? *Current Biology* (2004)

doi:10.1016/j.cub.2004.03.051.

147. Sternberg, S. R. Biomedical Image Processing. *Computer (Long. Beach. Calif).* (1983) doi:10.1109/MC.1983.1654163.

148. Hoogendoorn, E. *et al.* The fidelity of stochastic single-molecule super-resolution reconstructions critically depends upon robust background estimation. *Sci. Rep.* (2014) doi:10.1038/srep03854.

149. Stout, A. L. & Axelrod, D. Evanescent field excitation of fluorescence by epi-illumination microscopy. *Appl. Opt.* (1989) doi:10.1364/ao.28.005237.

150. Axelrod, D. Total internal reflection fluorescence microscopy in cell biology. *Traffic* (2001) doi:10.1034/j.1600-0854.2001.21104.x.

151. Mlodzianoski, M. J. *et al.* Sample drift correction in 3D fluorescence photoactivation localization microscopy. *Opt. Express* (2011) doi:10.1364/oe.19.015009.

152. Van De Linde, S. *et al.* Direct stochastic optical reconstruction microscopy with standard fluorescent probes. *Nat. Protoc.* (2011) doi:10.1038/nprot.2011.336.

153. MANDERS, E. M. M., VERBEEK, F. J. & ATEN, J. A. Measurement of co-localization of objects in dual-colour confocal images. *J. Microsc.* (1993) doi:10.1111/j.1365-2818.1993.tb03313.x.

154. Dunn, K. W., Kamocka, M. M. & McDonald, J. H. A practical guide to evaluating colocalization in biological microscopy. *American Journal of Physiology - Cell Physiology* (2011) doi:10.1152/ajpcell.00462.2010.

155. Baddeley, D., Cannell, M. B. & Soeller, C. Visualization of localization microscopy data. *Microsc. Microanal.* (2010) doi:10.1017/S143192760999122X.

156. Kriegel, H. P., Kröger, P., Sander, J. & Zimek, A. Density-based clustering. *Wiley Interdiscip. Rev. Data Min. Knowl. Discov.* (2011) doi:10.1002/widm.30.

157. Kittel, C. *Introduction to Solid State Physics*. (John Wiley & Sons, Inc, 2005).

158. Cheng, X. & Smith, J. C. Biological Membrane Organization and Cellular Signaling. *Chemical Reviews* (2019) doi:10.1021/acs.chemrev.8b00439.

159. Mañes, S., Del Real, G. & Martínez-A, C. Pathogens: Raft hijackers. *Nature Reviews Immunology* (2003) doi:10.1038/nri1129.

160. Kraft, M. L. Sphingolipid organization in the plasma membrane and the mechanisms that influence it. *Frontiers in Cell and Developmental Biology* (2017) doi:10.3389/fcell.2016.00154.

161. Frisz, J. F. *et al.* Direct chemical evidence for sphingolipid domains in the plasma membranes of fibroblasts. *Proc. Natl. Acad. Sci. U. S. A.* (2013) doi:10.1073/pnas.1216585110.

162. Frisz, J. F. *et al.* Sphingolipid domains in the plasma membranes of fibroblasts are not enriched

with cholesterol. *J. Biol. Chem.* (2013) doi:10.1074/jbc.M113.473207.

163. Gambhir, A. *et al.* Electrostatic Sequestration of PIP2 on Phospholipid Membranes by Basic/Aromatic Regions of Proteins. *Biophys. J.* (2004) doi:10.1016/S0006-3495(04)74278-2.

164. Won, D. H. *et al.* PI(3,4,5)P3 and PI(4,5)P2 lipids target proteins with polybasic clusters to the plasma membrane. *Science (80-.).* (2006) doi:10.1126/science.1134389.

165. McLaughlin, S. & Murray, D. Plasma membrane phosphoinositide organization by protein electrostatics. *Nature* (2005) doi:10.1038/nature04398.

166. Yin, H. L. & Janmey, P. A. Phosphoinositide Regulation of the Actin Cytoskeleton. *Annu. Rev. Physiol.* (2003) doi:10.1146/annurev.physiol.65.092101.142517.

167. Balla, T. Phosphoinositides: Tiny lipids with giant impact on cell regulation. *Physiological Reviews* (2013) doi:10.1152/physrev.00028.2012.

168. Raucher, D. *et al.* Phosphatidylinositol 4,5-bisphosphate functions as a second messenger that regulates cytoskeleton-plasma membrane adhesion. *Cell* (2000) doi:10.1016/S0092-8674(00)81560-3.

169. Van Den Bogaart, G. *et al.* Membrane protein sequestering by ionic protein-lipid interactions. *Nature* (2011) doi:10.1038/nature10545.

170. Wang, J. & Richards, D. A. Segregation of PIP2 and PIP3 into distinct nanoscale regions within the plasma membrane. *Biol. Open* (2012) doi:10.1242/bio.20122071.

171. Van Rheenen, J., Achame, E. M., Janssen, H., Calafat, J. & Jalink, K. PIP2 signaling in lipid domains: A critical re-evaluation. *EMBO J.* (2005) doi:10.1038/sj.emboj.7600655.

172. Haidari, M., Zhang, W., Ganjehei, L., Ali, M. & Chen, Z. Inhibition of MLC phosphorylation restricts replication of influenza virus-a mechanism of action for anti-influenza agents. *PLoS One* (2011) doi:10.1371/journal.pone.0021444.

173. Shaw, M. L., Stone, K. L., Colangelo, C. M., Gulcicek, E. E. & Palese, P. Cellular proteins in influenza virus particles. *PLoS Pathog.* (2008) doi:10.1371/journal.ppat.1000085.

174. Botelho, R. J. *et al.* Localized biphasic changes in phosphatidylinositol-4,5-bisphosphate at sites of phagocytosis. *J. Cell Biol.* (2000) doi:10.1083/jcb.151.7.1353.

175. Bentz, J. Minimal aggregate size and minimal fusion unit for the first fusion pore of influenza hemagglutinin-mediated membrane fusion. *Biophys. J.* (2000) doi:10.1016/S0006-3495(00)76587-8.

176. Clague, M. J., Schoch, C. & Blumenthal, R. Delay time for influenza virus hemagglutinin-induced membrane fusion depends on hemagglutinin surface density. *J. Virol.* (1991) doi:10.1128/jvi.65.5.2402-2407.1991.

177. Hammond, G. R. V. Does PtdIns(4,5)P2 concentrate so it can multi-task? *Biochem. Soc. Trans.* (2016) doi:10.1042/BST20150211.

178. Veit, M., Serebryakova, M. V. & Kordyukova, L. V. Palmitoylation of influenza virus proteins. in *Biochemical Society Transactions* (2013). doi:10.1042/BST20120210.

179. M., B., K., J. & R.V., S. Investigating phospholipid binding residues in the C terminus of ebola virus matrix protein, VP40. *FASEB J.* (2017).

180. Gc, J. B., Gerstman, B. S., Stahelin, R. V. & Chapagain, P. P. The Ebola virus protein VP40 hexamer enhances the clustering of PI(4,5)P2 lipids in the plasma membrane. *Phys. Chem. Chem. Phys.* (2016) doi:10.1039/c6cp03776c.

181. Johnson, K. A., Taghon, G. J. F., Scott, J. L. & Stahelin, R. V. The Ebola Virus matrix protein, VP40, requires phosphatidylinositol 4,5-bisphosphate (PI(4,5)P 2) for extensive oligomerization at the plasma membrane and viral egress. *Sci. Rep.* (2016) doi:10.1038/srep19125.

182. Chukkapalli, V., Hogue, I. B., Boyko, V., Hu, W.-S. & Ono, A. Interaction between the Human Immunodeficiency Virus Type 1 Gag Matrix Domain and Phosphatidylinositol-(4,5)-Bisphosphate Is Essential for Efficient Gag Membrane Binding. *J. Virol.* (2008) doi:10.1128/jvi.01614-07.

183. Chukkapalli, V. & Ono, A. Molecular determinants that regulate plasma membrane association of HIV-1 Gag. *Journal of Molecular Biology* (2011) doi:10.1016/j.jmb.2011.04.015.

184. Yandrapalli, N. *et al.* Self assembly of HIV-1 Gag protein on lipid membranes generates PI(4,5)P2/Cholesterol nanoclusters. *Sci. Rep.* (2016) doi:10.1038/srep39332.

185. Ono, A., Ablan, S. D., Lockett, S. J., Nagashima, K. & Freed, E. O. Phosphatidylinositol (4,5) bisphosphate regulates HIV-1 Gag targeting to the plasma membrane. *Proc. Natl. Acad. Sci. U. S. A.* (2004) doi:10.1073/pnas.0405596101.

186. Rocha-Perugini, V., Gordon-Alonso, M. & Sánchez-Madrid, F. PIP2: Choreographer of actin-adaptor proteins in the HIV-1 dance. *Trends in Microbiology* (2014) doi:10.1016/j.tim.2014.03.009.

187. Nobusawa, E. *et al.* Comparison of complete amino acid sequences and receptor-binding properties among 13 serotypes of hemagglutinins of influenza A viruses. *Virology* (1991) doi:10.1016/0042-6822(91)90588-3.

188. Brett, K. *et al.* Site-specific S-acylation of influenza virus hemagglutinin: The location of the acylation site relative to the membrane border is the decisive factor for attachment of stearate. *J. Biol. Chem.* (2014) doi:10.1074/jbc.M114.586180.

189. Veit, M. *et al.* Site-specific mutagenesis identifies three cysteine residues in the cytoplasmic tail as acylation sites of influenza virus hemagglutinin. *J. Virol.* (1991) doi:10.1128/jvi.65.5.2491-2500.1991.

190. Duncan, J. A. & Gilman, A. G. Autoacylation of G protein α subunits. *J. Biol. Chem.* (1996) doi:10.1074/jbc.271.38.23594.

191. Veit, M. *et al.* Palmitoylation of rhodopsin with S-protein acyltransferase: enzyme catalyzed reaction versus autocatalytic acylation. *Biochim. Biophys. Acta - Lipids Lipid Metab.* (1998) doi:10.1016/S0005-2760(98)00097-6.

192. Sobocinska, J., Roszczenko-Jasinska, P., Ciesielska, A. & Kwiatkowska, K. Protein palmitoylation and its role in bacterial and viral infections. *Frontiers in Immunology* (2018) doi:10.3389/fimmu.2017.02003.

193. Ali, A., Avalos, R. T., Ponimaskin, E. & Nayak, D. P. Influenza Virus Assembly: Effect of Influenza Virus Glycoproteins on the Membrane Association of M1 Protein. *J. Virol.* (2000) doi:10.1128/jvi.74.18.8709-8719.2000.

194. Zhang, J., Pekosz, A. & Lamb, R. A. Influenza Virus Assembly and Lipid Raft Microdomains: a Role for the Cytoplasmic Tails of the Spike Glycoproteins. *J. Virol.* (2000) doi:10.1128/jvi.74.10.4634-4644.2000.

195. Paules, C. I., Sullivan, S. G., Subbarao, K. & Fauci, A. S. Chasing seasonal influenza - The need for a universal influenza vaccine. *New England Journal of Medicine* (2018) doi:10.1056/NEJMp1714916.

196. Bijlmakers, M. J. & Marsh, M. The on-off story of protein palmitoylation. *Trends in Cell Biology* (2003) doi:10.1016/S0962-8924(02)00008-9.

197. Ponimaskin, E. & Schmidt, M. F. G. Domain-structure of cytoplasmic border region is main determinant for palmitoylation of influenza virus hemagglutinin (H7). *Virology* (1998) doi:10.1006/viro.1998.9303.

198. Di Paolo, G. & De Camilli, P. Phosphoinositides in cell regulation and membrane dynamics. *Nature* (2006) doi:10.1038/nature05185.

199. Saarikangas, J., Zhao, H. & Lappalainen, P. Regulation of the actin cytoskeleton-plasma membrane interplay by phosphoinositides. *Physiological Reviews* (2010) doi:10.1152/physrev.00036.2009.

200. Zhao, H., Hakala, M. & Lappalainen, P. ADF/cofilin binds phosphoinositides in a multivalent manner to act as a PIP(2)-density sensor. *Biophys. J.* (2010) doi:10.1016/j.bpj.2010.01.046.

201. Kumar, N., Zhao, P., Tomar, A., Galea, C. A. & Khurana, S. Association of Villin with Phosphatidylinositol 4,5-Bisphosphate Regulates the Actin Cytoskeleton. *J. Biol. Chem.* (2004) doi:10.1074/jbc.M308878200.

202. Mücksch, F., Laketa, V., Müller, B., Schultz, C. & Kräusslich, H. G. Synchronized HIV assembly by tunable PIP2 changes reveals PIP2 requirement for stable gag anchoring. *Elife* (2017) doi:10.7554/eLife.25287.

203. Veatch, S. L. *et al.* Correlation functions quantify super-resolution images and estimate apparent clustering due to over-counting. *PLoS One* (2012) doi:10.1371/journal.pone.0031457.

204. Melkonian, K. A., Ostermeyer, A. G., Chen, J. Z., Roth, M. G. & Brown, D. A. Role of lipid modifications in targeting proteins to detergent-resistant membrane rafts. Many raft proteins are

acylated, while few are prenylated. *J. Biol. Chem.* (1999) doi:10.1074/jbc.274.6.3910.

205. Leser, G. P. & Lamb, R. A. Influenza virus assembly and budding in raft-derived microdomains: A quantitative analysis of the surface distribution of HA, NA and M2 proteins. *Virology* (2005) doi:10.1016/j.virol.2005.09.049.

206. Schmitt, A. P. & Lamb, R. A. Influenza Virus Assembly and Budding at the Viral Budozone. *Advances in Virus Research* (2005) doi:10.1016/S0065-3527(05)64012-2.

207. Chen, B. J., Leser, G. P., Morita, E. & Lamb, R. A. Influenza Virus Hemagglutinin and Neuraminidase, but Not the Matrix Protein, Are Required for Assembly and Budding of Plasmid-Derived Virus-Like Particles. *J. Virol.* (2007) doi:10.1128/jvi.00361-07.

208. Chlanda, P. *et al.* Structural Analysis of the Roles of Influenza A Virus Membrane-Associated Proteins in Assembly and Morphology. *J. Virol.* (2015) doi:10.1128/jvi.00592-15.

209. Nikolaus, J. *et al.* Hemagglutinin of influenza virus partitions into the nonraft domain of model membranes. *Biophys. J.* (2010) doi:10.1016/j.bpj.2010.04.027.

210. Simpson, D. A. & Lamb, R. A. Alterations to influenza virus hemagglutinin cytoplasmic tail modulate virus infectivity. *J. Virol.* (1992) doi:10.1128/jvi.66.2.790-803.1992.

211. Catimel, B. *et al.* The PI(3,5)P2 and PI(4,5)P2 interactomes. *J. Proteome Res.* (2008) doi:10.1021/pr800540h.

212. Debye, P. & Hückel, E. On the Theory of Electrolytes. I. Freezing Point Depression and Related Phenomena. *Phys. Zeitschrift* (1923).

213. Copeland, C. S., Doms, R. W., Bolzau, E. M., Webster, R. G. & Helenius, A. Assembly of influenza hemagglutinin trimers and its role in intracellular transport. *J. Cell Biol.* (1986) doi:10.1083/jcb.103.4.1179.

214. Chu, C. H. *et al.* Beyond the Debye length in high ionic strength solution: Direct protein detection with field-effect transistors (FETs) in human serum. *Sci. Rep.* (2017) doi:10.1038/s41598-017-05426-6.

215. Alberts, B. *et al. Molecular Biology of the Cell, Sixth Edition*. (Garland Science, 2014).

216. Sekikawa, K. & Lai, C. J. Defects in functional expression of an influenza virus hemagglutinin lacking the signal peptide sequences. *Proc. Natl. Acad. Sci. U. S. A.* (1983) doi:10.1073/pnas.80.12.3563.

217. Abdul Jabbar, M. & Nayak, D. P. Signal processing, glycosylation, and secretion of mutant hemagglutinins of a human influenza virus by Saccharomyces cerevisiae. *Mol. Cell. Biol.* (1987) doi:10.1128/mcb.7.4.1476.

218. Finidori, J. *et al.* The influenza hemagglutinin insertion signal is not cleaved and does not halt translocation when presented to the endoplasmic reticulum membrane as part of a translocating polypeptide. *J. Cell Biol.* (1987) doi:10.1083/jcb.104.6.1705.

219. Su, Y., Zhang, B., Shen, Y. & Huang, J. Effects of signal peptide sequence of hemagglutinin on the expression of green fluorescent protein and hemagglutinin fusion gene. *Wei Sheng Wu Xue Bao* (2009).

220. Los, G. V. *et al.* HaloTag: A novel protein labeling technology for cell imaging and protein analysis. *ACS Chem. Biol.* (2008) doi:10.1021/cb800025k.

221. Downes, C. P., Gray, A. & Lucocq, J. M. Probing phosphoinositide functions in signaling and membrane trafficking. *Trends in Cell Biology* (2005) doi:10.1016/j.tcb.2005.03.008.

222. Ohkura, T., Momose, F., Ichikawa, R., Takeuchi, K. & Morikawa, Y. Influenza A Virus Hemagglutinin and Neuraminidase Mutually Accelerate Their Apical Targeting through Clustering of Lipid Rafts. *J. Virol.* (2014) doi:10.1128/jvi.00586-14.

223. Barman, S., Ali, A., Hui, E. K. W., Adhikary, L. & Nayak, D. P. Transport of viral proteins to the apical membranes and interaction of matrix protein with glycoproteins in the assembly of influenza viruses. *Virus Res.* (2001) doi:10.1016/S0168-1702(01)00266-0.

224. Niggli, V. & Keller, H. The phosphatidylinositol 3-kinase inhibitor wortmannin markedly reduces chemotactic peptide-induced locomotion and increases in cytoskeletal actin in human neutrophils. *Eur. J. Pharmacol.* (1997) doi:10.1016/S0014-2999(97)01169-2.

225. Niggli, V. A membrane-permeant ester of phosphatidylinositol 3,4,5-trisphosphate (PIP3) is an activator of human neutrophil migration. *FEBS Lett.* (2000) doi:10.1016/S0014-5793(00)01534-9.

226. Derman, M. P. *et al.* The lipid products of phosphoinositide 3-kinase increase cell motility through protein kinase C. *J. Biol. Chem.* (1997) doi:10.1074/jbc.272.10.6465.

227. Fujioka, Y. *et al.* A Ca2+-dependent signalling circuit regulates influenza A virus internalization and infection. *Nat. Commun.* (2013) doi:10.1038/ncomms3763.

228. Wen, Y., Vogt, V. M. & Feigenson, G. W. Multivalent Cation-Bridged PI(4,5)P2 Clusters Form at Very Low Concentrations. *Biophys. J.* (2018) doi:10.1016/j.bpj.2018.04.048.

229. Laux, T. *et al.* GAP43, MARCKS, and CAP23 modulate PI(4,5)P2 at plasmalemmal rafts, and regulate cell cortex actin dynamics through a common mechanism. *J. Cell Biol.* (2000) doi:10.1083/jcb.149.7.1455.

230. Rauch, M. E., Ferguson, C. G., Prestwich, G. D. & Cafiso, D. S. Myristoylated alanine-rich C kinase substrate (MARCKS) sequesters spin-labeled phosphatidylinositol 4,5-bisphosphate in lipid bilayers. *J. Biol. Chem.* (2002) doi:10.1074/jbc.M109572200.

231. Parent, M. & Hess, S. T. Quantification of Mitochondrial Membrane Curvature by Three-Dimensional Localization Microscopy. *Isc. Notes* **4**, 1–3 (2019).

232. Chan, D. C. Mitochondrial Fusion and Fission in Mammals. *Annu. Rev. Cell Dev. Biol.* **22**, 79–99 (2006).

233. Mlodzianoski, M. J., Juette, M. F., Beane, G. L. & Bewersdorf, J. Experimental characterization of 3D localization techniques for particle-tracking and super-resolution microscopy. *Opt. Express* (2009) doi:10.1364/oe.17.008264.

234. Kirkpatrick, D. G. & Seidel, R. On the Shape of a Set of Points in the Plane. *IEEE Trans. Inf. Theory* (1983) doi:10.1109/TIT.1983.1056714.

235. Jülicher, F. & Lipowsky, R. (CUL-ID:1658853) Shape transformations of vesicles with intramembrane domains. *Phys. Rev. E* (1996) doi:10.1103/PhysRevE.53.2670.

236. Lipowsky, R. Budding of membranes induced by intramembrane domains. *J. Phys. II* **2**, 1825–1840 (1992).

237. Hess, S. T., Gudheti, M. V., Mlodzianoski, M. & Baumgart, T. Shape analysis of giant vesicles with fluid phase coexistence by laser scanning microscopy to determine curvature, bending elasticity, and line tension. *Methods Mol. Biol.* (2007) doi:10.1385/1-59745-519-9:367.

APPENDIX A: PLASMID SEQUENCES

Dendra2-HA plasmid sequence: Color Key: Dendra2 HA X-31B

CCCATTGACGTCAATGGGAGTTTGTTTTGGCACCAAAATCAACGGGACTTTCCAAAATGTCGTAACAACT
CCGCCCCATTGACGCAAATGGGCGGTAGGCGTGTACGGTGGGAGGTCTATATAAGCAGAGCTGGTTTAGT
GAACCGTCAGATCCGCTAGCGCTACCGGTCGCCACCATGAACACCCCGGGAATTAACCTGATCAAGGAGG
ACATGCGCGTGAAGGTGCACATGGAGGGCAACGTGAACGGCCACGCCTTCGTGATCGAGGGCGAGGGCAA
GGGCAAGCCCTACGAGGGCACCCAGACCGCCAACCTGACCGTGAAGGAGGGCGCCCCCCTGCCCTTCAGC
TACGACATCCTGACCACCGCCGTGCACTACGGCAACCGGGTGTTCACCAAGTACCCCGAGGACATCCCCG
ACTACTTCAAGCAGAGCTTCCCCGAGGGCTACAGCTGGGAGCGCACCATGACCTTCGAGGACAAGGGCAT
CTGCACCATCCGCAGCGACATCAGCCTGGAGGGCGACTGCTTCTTCCAGAACGTGCGCTTCAAGGGCACC
AACTTCCCCCCCAACGGCCCCGTGATGCAGAAGAAGACCCTGAAGTGGGAGCCCAGCACCGAGAAGCTGC
ACGTGCGCGACGGCCTGCTGGTGGGCAACATCAACATGGCCCTGCTGCTGGAGGGCGGCGGCCACTACCT
GTGCGACTTCAAGACCACCTACAAGGCCAAGAAGGTGGTGCAGCTGCCCGACGCCCACTTCGTGGACCAC
CGCATCGAGATCCTGGGCAACGACAGCGACTACAACAAGGTGAAGCTGTACGAGCACGCCGTGGCCCGCT
ACAGCCCCCTGCCCAGCCAGGTGTGGTCCGGCGACAGCGGCGTGTACAAGTCCGGAATGAAGACCATCAT
TGCTTTGAGCTACATTTTCTGTCTGGCTCTCGGCCAAGACCTTCCAGGAAATGACAACAGCACAGCAACG
CTGTGCCTGGGACATCATGCGGTGCCAAACGGAACACTAGTGAAAACAATCACAGATGATCAGATTGAAG
TGACTAATGCTACTGAGCTAGTTCAGAGCTCCTCAACGGGGAAAATATGCAACAATCCTCATCGAATCCT
TGATGGAATAGACTGCACACTGATAGATGCTCTATTGGGGGACCCTCATTGTGATGTTTTTCAAAATGAG
ACATGGGACCTTTTCGTTGAACGCAGCAAAGCTTTCAGCAACTGTTACCCTTATGATGTGCCAGATTATG
CCTCCCTTAGGTCACTAGTTGCCTCGTCAGGCACTCTGGAGTTTATCACTGAGGGTTTCACTTGGACTGG
GGTCACTCAGAATGGGGGAAGCAATGCTTGCAAAAGGGGACCTGGTAGCGGTTTTTTCAGTAGACTGAAC
TGGTTGACCAAATCAGGAAGCACATATCCAGTGCTGAACGTGACTATGCCAAACAATGACAATTTTGACA
AACTATACATTTGGGGGATTCACCACCCGAGCACGAACCAAGAACAAACCAGCCTGTATGTTCAAGCATC
AGGGAGAGTCACAGTCTCTACCAGGAGAAGCCAGCAAACTATAATCCCGAATATCGGGTCCAGACCCTGG
GTAAGGGGTCTGTCTAGTAGAATAAGCATCTATTGGACAATAGTTAAGCCGGGAGACGTACTGGTAATTA
ATAGTAATGGGAACCTAATCGCTCCTCGGGGTTATTTCAAAATGCGCACTGGGAAAAGCTCAATAATGAG
GTCAGATGCACCCATTGATACCTGTATTTCTGAATGCATCACTCCAAATGGAAGCATTCCCAATGACAAG
CCCTTTCAAAACGTAAACAAGATCACATATGGAGCATGCCCCAAGTATGTTAAGCAAAACACCCTGAAGT
TGGCAACAGGGATGCGGAATGTACCAGAGAAACAAACTAGAGGCCTATTCGGCGCAATAGCAGGTTTCAT
AGAAAATGGTTGGGAGGGAATGATAGACGGTTGGTACGGTTTCAGGCATCAAAATTCTGAGGGCACAGGA
CAAGCAGCAGATCTTAAAAGCACTCAAGCAGCCATCGACCAAATCAATGGGAAATTGAACAGGGTAATCG
AGAAGACGAACGAGAAATTCCATCAAATCGAAAAGGAATTCTCAGAAGTAGAAGGGAGAATTCAGGACCT
CGAGAAATACGTTGAAGACACTAAAATAGATCTCTGGTCTTACAATGCGGAGCTTCTTGTCGCTCTGGAG
AATCAACATACAATTGACCTGACTGACTCGGAAATGAACAAGCTGTTTGAAAAAACAAGGAGGCAACTGA
GGGAAAATGCTGAAGACATGGGCAATGGTTGCTTCAAAATATACCACAAATGTGACAACGCTTGCATAGA
GTCAATCAGAAATGGGACTTATGACCATGATGTATACAGAGACGAAGCATTAAACAACCGGTTTCAGATC
AAAGGTGTTGAACTGAAGTCTGGATACAAAGACTGGATCCTGTGGATTTCCTTTGCCATATCATGCTTTT
TGCTTTGTGTTGTTTTGCTGGGGTTCATCATGTGGGCCTGCCAGAGAGGCAACATTAGGTGCAACATTTG
CATTTGAGTGTATTAGTAATTAAAAACACCCTTGTTTCTACTGCTAGGTCGACGGTACCGCGGGCCCGGG
ATCCACCGGATCTAGATAACTGATCATAATCAGCCATACCACATTTGTAGAGGTTTTACTTGCTTTAAAA
AACCTCCCACACCTCCCCCTGAACCTGAAACATAAAATGAATGCAATTGTTGTTGTTAACTTGTTTATTG
CAGCTTATAATGGTTACAAATAAAGCAATAGCATCACAAATTTCACAAATAAAGCATTTTTTTCACTGCA
TTCTAGTTGTGGTTTGTCCAAACTCATCAATGTATCTTAAGGCGTAAATTGTAAGCGTTAATATTTTGTT
AAAATTCGCGTTAAATTTTTGTTAAATCAGCTCATTTTTTAACCAAT

APPENDIX B: MATLAB CODE FOR RDFS AND CLUSTER PROPERTIES

The following code was written and executed to calculate both radial distribution functions and cluster properties for HA and HA mutant clusters using MATLAB 2018a or higher.

ClusterRDFGrid_v4.m

```
%% Find Cluster RDFs v4 (2color) GRID VERSION
% ** Requires 'alpha' appended to each file
% [MP]

clear; clc;

%% User options
% defaultpath='D:\Local Mutant Data\2018-2019 RB6 HA Mutants & PH\';
savepath='K:\PhD\2019 HAmutants & PH\Rolling Ball ND50\RDF\'; %
Default save path
% -------
% Cluster identification settings
binsize=.02; % Grid size in microns
kernal=5;    % Kernal sized
rad=0.05;    % Radius in um40nm
thresh=3;    % How far above the mean density to be considered a
cluster?
bleedthrough=[0.07 0.07]; % Bleedthrough correction []
useCellmask=0; % Use whole cell or individual channel mask to
calculate density (1=cell mask, 0=channel mask)
% -------
% RDF Settings
rmax=1;    % Max distance for RDF calculation
ncor=10;   % Number of elements at end of RDF used for correction
% CLUSTER limits:
minarea=25*(binsize^2);% min area per cluster (um^2)
maxdensity=16000;  % max cluster density in mol/um^2 (Ausborn et al,
'Role of Hemagglutinin Surface Density in the Initial Stages of
Influenza Virus Fusion: Lack of Evidence for Cooperativity', 2000)
% CELL limits:
minreddensity=200;   % minimum cell density (Red channel)
mingreendensity=200; % minimum cell density (Green channel)
minexp=0.10;         % minimum cell expression ratio

fpath={'K:\PhD\2019 HAmutants & PH\Rolling Ball ND50\HAMAY\',...
    'K:\PhD\2019 HAmutants & PH\Rolling Ball ND50\HARE\',...
    'K:\PhD\2019 HAmutants & PH\Rolling Ball ND50\HAREMAY\',...
    'K:\PhD\2019 HAmutants & PH\Rolling Ball ND50\HARREQ\',...
    'K:\PhD\2019 HAmutants & PH\Rolling Ball ND50\HATailless\',...
    'K:\PhD\2019 HAmutants & PH\Rolling Ball ND50\HAwt\'};
% fpath={'D:\Local Mutant Data\2018-2019 TMF2 HA Mutants &
PH\HAMAY\ND50nm\',...
%     'D:\Local Mutant Data\2018-2019 TMF2 HA Mutants &
PH\HARE\ND50nm\',...
```

```
%     'D:\Local Mutant Data\2018-2019 TMF2 HA Mutants &
PH\HAREMAY\ND50nm\',...
%     'D:\Local Mutant Data\2018-2019 TMF2 HA Mutants &
PH\HAwt\ND50nm\',...
%     'D:\Local Mutant Data\2018-2019 TMF2 HA Mutants &
PH\RREQ\ND50nm\',...
%     'D:\Local Mutant Data\2018-2019 TMF2 HA Mutants &
PH\Tailless\ND50nm\'};

% [inputfile,fpath]=uigetfile('','',defaultpath,'Multiselect','on');
% if iscell(inputfile)
%     fend=numel(inputfile);
% else
%     fend=1;
%     inputfile=cellstr(inputfile);
% end
% fpath=cellstr(fpath);

%% Loop through all folders
for bb=1:numel(fpath)
    % Reset file variables on each pass, keeping settings
    clearvars -except useCellmask minexp ncor savepath bb fpath
binsize kernal rad thresh maxdensity minarea rmax minreddensity
mingreendensity bleedthrough steps maskringfull maskring maskringsum

    directory=fpath{bb};
    inputfile=dir([directory,'*.mat']);
    fend=numel(inputfile);

    disp('Batching:')
    disp('...')

    % Initialize variables
    gor_green_all=[]; gor_red_all=[];
    gor_red_all_adj=[]; gor_green_all_adj=[];
    dr=binsize;  % dr must equal bin size
    ncells=0; % Number of cells that passed the checks

%% Generate appropriate ring masks for RDF calculation on first pass
    % ----------------------------------------
    if bb==1
        steps=round(rmax./binsize);
        seed=zeros(1+steps*2,1+steps*2);
        cmrx=ceil(size(seed,2)/2);
        cmry=ceil(size(seed,1)/2);
        seed(cmry,cmrx)=1;

        maskouter=seed;
        maskinner=zeros(size(seed));
        maskring=zeros([size(seed),steps+1]);
        maskringfull=zeros(size(seed));
```

```
        for k=1:steps+1
            if k~=1
                maskouter=imdilate(seed,strel('disk',k-1,0));
                maskinner=imdilate(seed,strel('disk',k-2,0));
            end

            maskring(:,:,k)=maskouter-maskinner;
            maskringfull=maskring(:,:,k)+maskringfull;
        end
        maskring=logical(maskring);
        maskringsum=sum(maskringfull(:));
    end
    % ---------------------------

%% Loop through all files, calculate cluster g(r), and find cluster
properties
    for ii=1:fend
        disp([num2str(ii),'/',num2str(fend),': ',inputfile(ii).name])
%         load([fpath,inputfile{i}])
        load([fpath{bb},inputfile(ii).name])

        % Find size to use for gridding

sxsy=[ceil(max(yf_all*q)/binsize)+2*kernal,ceil(max(xf_all*q)/binsize)
+2*kernal];

        % Split data into channels
        xf_all_green=xf_all(nrat>=alpha(1) & nrat<=alpha(2));
        yf_all_green=yf_all(nrat>=alpha(1) & nrat<=alpha(2));
        xf_all_red=xf_all(nrat>=alpha(3) & nrat<=alpha(4));
        yf_all_red=yf_all(nrat>=alpha(3) & nrat<=alpha(4));
        xf_um_green=xf_all_green*q;
        yf_um_green=yf_all_green*q;
        xf_um_red=xf_all_red*q;
        yf_um_red=yf_all_red*q;

        % Grid red and green data
%         % Gaussian convolution
%
grid_green=fDeltaGauss(xf_all_green,yf_all_green,kernal,rad,binsize,q,
sxsy);
%
grid_red=fDeltaGauss(xf_all_red,yf_all_red,kernal,rad,binsize,q,sxsy);

%         % Circle convolution

[grid_green,grid_green_conv]=fDeltaCircleConv2(xf_all_green,yf_all_gre
en,kernal,rad,binsize,q,sxsy);

[grid_red,grid_red_conv]=fDeltaCircleConv2(xf_all_red,yf_all_red,kerna
l,rad,binsize,q,sxsy);
```

```
%% Bleedthrough correct data
        grid_green_copy=grid_green_conv;
        grid_red_copy=grid_red_conv;
        grid_green_conv=(grid_green_copy-
bleedthrough(1)*grid_green_copy-bleedthrough(1)*grid_red_copy)./(1-
bleedthrough(1)-bleedthrough(2));
        grid_red_conv=(grid_red_copy-bleedthrough(2)*grid_red_copy-
bleedthrough(2)*grid_green_copy)./(1-bleedthrough(1)-bleedthrough(2));
        grid_green_conv(grid_green_conv<0)=0;
        grid_red_conv(grid_red_conv<0)=0;

        nred=sum(grid_red_conv(:));
        ngreen=sum(grid_green_conv(:));
%% Find cluster properties
        grid_sum=grid_green_conv+grid_red_conv; % Grid of all the
molecules

        % Approximate cell area

init_mask=imdilate(grid_sum>0,strel('disk',round(rad/binsize)));
        init_mask=imfill(init_mask,'holes'); % Fill holes in the mask

        % Find largest connected component to use as cell area
        connect=bwconncomp(init_mask);
        numpix = cellfun(@numel,connect.PixelIdxList);
        [~,idx]=max(numpix);
        cell_mask=zeros(size(init_mask));
        cell_mask(connect.PixelIdxList{idx})=1;
        cell_mask=logical(cell_mask);
        cell_area(ii)=sum(cell_mask(:))*binsize^2;

        % Use cell mask or individual channel mask?
        if useCellmask

cell_density_red(ii)=sum(grid_red_conv(cell_mask))./(sum(cell_mask(:))
.*binsize^2);

cell_density_green(ii)=sum(grid_green_conv(cell_mask))./(sum(cell_mask
(:)).*binsize^2);
        else
%
red_mask=imdilate(grid_red>0,strel('disk',round(rad/binsize)));
%             red_mask=imfill(grid_red>0,'holes'); % Fill holes in the
mask
            red_mask=grid_red_conv>0;
            red_mask=red_mask&cell_mask;
%
green_mask=imdilate(grid_green>0,strel('disk',round(rad/binsize)));
%             green_mask=imfill(grid_green>0,'holes');
            green_mask=grid_green_conv>0;
            green_mask=green_mask&cell_mask;
```

```
cell_density_red(ii)=sum(grid_red_conv(red_mask))./(sum(red_mask(:)).*
binsize^2);

cell_density_green(ii)=sum(grid_green_conv(green_mask))./(sum(green_ma
sk(:)).*binsize^2);
        end

    % Red channel
        % Threshold above the average and find cluster stats
%         grid_norm=grid_red./mean(grid_red(cell_mask));
        grid_norm=grid_red_conv./(cell_density_red(ii).*binsize^2);
        grid_bw_red=grid_norm>thresh;

stats_red=regionprops(grid_bw_red,grid_red_conv,'PixelIdxList','Area',
'MinorAxisLength','MajorAxisLength','WeightedCentroid','PixelValues','
Eccentricity','Perimeter');

    % Green Channel
        % Threshold above the average and find cluster stats
%         grid_norm=grid_green./mean(grid_green(cell_mask));

grid_norm=grid_green_conv./(cell_density_green(ii).*binsize^2);
        grid_bw_green=grid_norm>thresh;

stats_green=regionprops(grid_bw_green,grid_green_conv,'PixelIdxList','
Area','MinorAxisLength','MajorAxisLength','WeightedCentroid','PixelVal
ues','Eccentricity','Perimeter');

 %% Apply CELL density limit
        if cell_density_green(ii)<mingreendensity ||
cell_density_red(ii)<minreddensity || nred/(nred+ngreen)<minexp ||
ngreen/(nred+ngreen)<minexp
            disp([' *Skipping cell ',num2str(ii),':','
G:',num2str(cell_density_green(ii)),'
R:',num2str(cell_density_red(ii)),'
Gr:',num2str(ngreen/(nred+ngreen),3),'
Rr:',num2str(nred/(nred+ngreen),3)])

%         subplot(1,3,1)
%         imagesc(cell_mask)
%         axis image
%         subplot(1,3,2)
%         imagesc(green_mask)
%         axis image
%         subplot(1,3,3)
%         imagesc(red_mask)
%         axis image
% %         waitforbuttonpress
%         drawnow

            % Record variables in fail instances
```

```
            adj_red(ii)=0;
            adj_green(ii)=0;

            R_all(ii)=NaN;
            MandersG(ii)=NaN;
            MandersR(ii)=NaN;

            % Store cell variables
            gor_green_cell{ii}=NaN;
            gor_red_cell{ii}=NaN;
            stats_green_cell{ii}=stats_green;
            stats_red_cell{ii}=stats_red;

            % Store cluster properties
            clusterdensity_green_cell{ii}=NaN;
            area_green_cell{ii}=NaN;
            perimeter_green_cell{ii}=NaN;
            eccentricity_green_cell{ii}=NaN;

            clusterdensity_red_cell{ii}=NaN;
            area_red_cell{ii}=NaN;
            perimeter_red_cell{ii}=NaN;
            eccentricity_red_cell{ii}=NaN;

            success_all{ii}=NaN;

            continue % Skip further calculations for cells that didn't
pass the checks
        else
            ncells=ncells+1; % Count number of cells we've
successfully included
        end

 %% Find RDFs for all clusters
        % -------------------------
        f=0; gor_green=[]; gor_red=[]; % Initialize g(r) variables
        redUnder=[]; redUnder_norm=[];
        success=zeros(numel(stats_green),1); % Flag clusters that pass
the checks
        success=logical(success); % Make logical

        % Calculate RDF for each cluster found
        for jj=1:numel(stats_green)
            % Calculate cluster densities and areas in real space

stats_green(jj).ClusterArea=stats_green(jj).Area*binsize^2;

stats_green(jj).ClusterDensity=sum(stats_green(jj).PixelValues)./stats
_green(jj).ClusterArea;

            % Apply CLUSTER limits
```

```
            if stats_green(jj).ClusterArea>=minarea &&
stats_green(jj).ClusterDensity<=maxdensity
                % Find center of mass grid coordinate
                cmx=round(stats_green(jj).WeightedCentroid(1));
                cmy=round(stats_green(jj).WeightedCentroid(2));

                if cmy-steps>=1 && cmy+steps<=sxsy(1) && cmx-steps>=1
&& cmx+steps<=sxsy(2)
                    success(jj)=1; % Flag cluster as succeeding the
checks

                    % Grab data around the CoM coordinate
                    grab_green=grid_green_conv(cmy-
steps:cmy+steps,cmx-steps:cmx+steps);
                    grab_red=grid_red_conv(cmy-steps:cmy+steps,cmx-
steps:cmx+steps);
                    cell_mask_grab=cell_mask(cmy-steps:cmy+steps,cmx-
steps:cmx+steps);

                    f=f+1;


redUnder_norm(f)=sum(grid_red_conv(stats_green(jj).PixelIdxList)./(cel
l_density_red(ii).*binsize^2*numel(stats_green(jj).PixelIdxList)));

redUnder(f)=sum(grid_red_conv(stats_green(jj).PixelIdxList));
                    % Calculate RDF of cluster
                    for k=1:steps+1
                        maskring_grab=maskring(:,:,k)&cell_mask_grab;
% Find components of the maskring that are within the cell mask

gor_green(f,k)=sum(grab_green(maskring_grab))./(sum(sum(maskring_grab>
0))*binsize*binsize*cell_density_green(ii));

gor_red(f,k)=sum(grab_red(maskring_grab))./(sum(sum(maskring_grab>0))*
binsize*binsize*cell_density_red(ii));
                    end
                end
            end
        end

        for jj=1:numel(stats_red)
            stats_red(jj).ClusterArea=stats_red(jj).Area*binsize^2;

stats_red(jj).ClusterDensity=sum(stats_red(jj).PixelValues)./stats_red
(jj).ClusterArea;
        end

        % Remove NaN values from RDF
        gor_green(isnan(gor_green))=0;
        gor_red(isnan(gor_red))=0;
```

```
        % Calculate Manders Correlation Coefficients and Pearson
Coefficients
        grid_green_masked=grid_green_conv(cell_mask);
        grid_red_masked=grid_red_conv(cell_mask);
%         grid_green_masked=grid_green(cell_mask);
%         grid_red_masked=grid_red(cell_mask);
        [R,P]=corrcoef(grid_green_masked,grid_red_masked);
        R_all(ii)=R(1,2);

MandersG(ii)=sum(grid_green_masked(grid_red_masked>0))/sum(grid_green_
masked(:));

MandersR(ii)=sum(grid_red_masked(grid_green_masked>0))/sum(grid_red_ma
sked(:));

        % Save stuff:
        % Record g(r)
        gor_green_all=vertcat(gor_green_all,gor_green);
        gor_red_all=vertcat(gor_red_all,gor_red);

        % Record g(r) (correct for cell density estimate)
        adj_red(ii)=mean(mean(gor_red(1:end,end-ncor:end)));
        adj_green(ii)=mean(mean(gor_green(1:end,end-ncor:end)));
        gor_red_all_adj=vertcat(gor_red_all_adj,gor_red./adj_red(ii));

gor_green_all_adj=vertcat(gor_green_all_adj,gor_green./adj_green(ii));

        redUnder_all_adj{ii}=redUnder_norm./adj_red(ii);
        redUnder_all{ii}=redUnder;
        redUnder_norm_all{ii}=redUnder_norm;

        % Store cell variables
        gor_green_cell{ii}=gor_green;
        gor_red_cell{ii}=gor_red;
        stats_green_cell{ii}=stats_green;
        stats_red_cell{ii}=stats_red;

        % Store cluster properties

clusterdensity_green_cell{ii}=vertcat(stats_green(success).ClusterDens
ity);
        area_green_cell{ii}=vertcat(stats_green(success).ClusterArea);

perimeter_green_cell{ii}=vertcat(stats_green(success).Perimeter)*binsi
ze;

eccentricity_green_cell{ii}=vertcat(stats_green(success).Eccentricity)
;

        clusterdensity_red_cell{ii}=vertcat(stats_red.ClusterDensity);
        area_red_cell{ii}=vertcat(stats_red.ClusterArea);
        perimeter_red_cell{ii}=vertcat(stats_red.Perimeter)*binsize;
```

```
        eccentricity_red_cell{ii}=vertcat(stats_red.Eccentricity);

        success_all{ii}=success;
    end

%% Calculate standard errors
    err_green=std(gor_green_all)./sqrt(size(gor_green_all,1));  %
Standard Error
    err_red=std(gor_red_all)./sqrt(size(gor_red_all,1));

err_green_adj=std(gor_green_all_adj)./sqrt(size(gor_green_all_adj,1));
% Standard Error Adjusted
    err_red_adj=std(gor_red_all_adj)./sqrt(size(gor_red_all_adj,1));

%% Extract commonly used cluster properties
    % Save results

savevars={'gor_green_all','gor_red_all','binsize','kernal','rad','thre
sh','minarea','maxdensity',...

'dr','rmax','err_green','err_red','cell_density_red','cell_density_gre
en','cell_area'...

'stats_red_cell','stats_green_cell','maskring','adj_red','adj_green',.
..

'gor_green_all_adj','gor_red_all_adj','err_green_adj','err_red_adj','g
or_green_cell',...

'gor_red_cell','ncells','ncor','clusterdensity_green_cell','area_green
_cell',...

'perimeter_green_cell','eccentricity_green_cell','clusterdensity_red_c
ell','area_red_cell',...

'perimeter_red_cell','eccentricity_red_cell','success_all','MandersG',
'MandersR','R_all',...

'inputfile','redUnder_all','redUnder_norm_all','redUnder_all_adj'};
    save([savepath,inputfile(1).name(1:end-
4),'_RDFgrid.mat'],savevars{:})
    disp(['Completed ',num2str(ncells),'/',num2str(fend),'
succcessfully.'])
end

% % Debug
% disp(['Mean green adj: ',num2str(mean(adj_green(adj_green>0)))])
% disp(['Mean red adj: ',num2str(mean(adj_red(adj_red>0)))])
```

fDeltaCircleConv2.m

```
% Convolve a delta function with a circle to grid molecules with conv2
% Inputs:
%     xf_all  - X Coordinates
%     yf_all  - Y coordinates
%     kernal  - Kernal size for circle
%     rad     - Radius of circle for convolution
%     binsize - Size of bins for grid
%     q       - Pixel size
%     sxsy    - Size of grid (pass empty matrix to automatically
calculate size)
% Outputs:
%     grid    - Projected grid data
% [MP]
function
[grid,gridconv]=fDeltaCircleConv2(xf_all,yf_all,kernal,rad,binsize,q,s
xsy)
    if isempty(sxsy)

sxsy=[ceil(max(yf_all*q)/binsize)+2*kernal,ceil(max(xf_all*q)/binsize)
+2*kernal];
    end
    % Set up grid to hold data
    grid=zeros(sxsy);

    % Bin data
    xbin=ceil((xf_all*q)/binsize)+kernal;
    ybin=ceil((yf_all*q)/binsize)+kernal;

    for i=1:numel(xbin)
        grid(ybin(i),xbin(i))=grid(ybin(i),xbin(i))+1;
    end

    xdata=meshgrid(-kernal:kernal); % Kernal grid
    ydata=meshgrid(-kernal:kernal)';
    z=(xdata).^2+(ydata).^2<=(rad./binsize)^2;
    z=z./sum(z(:));

    gridconv=conv2(grid,z,'same');
end
```

APPENDIX C: 3D MEMBRANE CURVATURE

Preface:

This paper was originally published under the title "Quantification of Mitochondrial Membrane Curvature by Three-Dimensional Localization Microscopy" by authors Matthew Parent and Samuel T Hess in iScienceNotes, Volume 4, Issue 3, 2019.[231]

Mitochondrial morphologies are essential to their function, and significant changes to mitochondrial membrane curvature have been implicated in a number of neurodegenerative diseases.[232] Mitochondria are often too small to properly resolve with conventional fluorescence microscopy techniques. However, the advent of super-resolution methods, such as FPALM[57], PALM[58], and STORM[59], have opened new opportunities for noninvasive observation at the nanoscale. Here we present a method for estimating the curvature of super-resolved mitochondrial membranes in three dimensions. In addition to its specific application to mitochondria presented here, this method can be useful for quantification of membrane curvature in a variety of cellular contexts, such as other intracellular organelles, viral protein clustering and budding in the plasma membrane, and modulation of membrane curvature by cytoskeletal elements.

In this case, we used astigmatic FPALM[68,233] to image mitochondria in C2C12 mouse myotubes expressing pTOM20-Dendra2, a marker for the outer mitochondrial membrane fused with a photoswitchable fluorescent protein. Individual molecules were localized by fitting point spread functions to a 2D Gaussian, whose x and y radii vary according the molecules z position. Then, from coordinates of localized molecules, the local membrane curvature could be determined through a 3-step process: mitochondrial identification, edge detection, and curve fitting.

To identify mitochondria (i.e. clusters of localized points), the data is passed through single linkage cluster analysis (SLCA) which iteratively links points within R_{max} of each other (here R_{max}=75nm) and is

based on a previously published algorithm.[73] Any clusters reaching a minimum of 150 points were considered individual mitochondria and saved for further analysis.

Once each mitochondrion has been identified, the cluster edges need to be determined prior to fitting. To do this, we find an appropriate alpha shape which describes the set of points that lie along the boundary of each cluster. Alpha shapes are a generalization of the convex hull that contain a tunable parameter, the alpha radius, which describes how closely boundary points are followed.[234] To best describe the details of the surface, the alpha radius should be chosen such that it is as small as possible while still producing contiguous shapes. If an alpha shape is found with multiple regions, only the region with the largest volume should be used, as this represents the outermost boundary of the shape. Since the ideal alpha radius depends, in part, on the sampling density and localization precision, it should be chosen empirically.

Within each alpha shape, we further select a subset of points within a sampling radius, R_s=200nm, of each point which are used for curve fitting. To reduce errors from fitting, R_s is chosen so that it is smaller than the size of any individual mitochondrion but larger than the localization precision of the individual molecules. Principle component analysis (PCA)[67] is then used to rotate this subset of points and the Z-axis is set as the principal component with the least variance. Rotated sections are fitted by least squares to a paraboloid of the form:

$$z = C_x(x - x_0)^2 + C_y(y - y_0)^2 + z_0$$

where the sum of the absolute values of C_x and C_y represent the commonly reported mean curvature[235,236] (μm^{-1}), $C_{mean} = C_x + C_y$, and where x_0, y_0, and z_0 are position offsets. This process is repeated for each point in each alpha shape and a colormap is applied to visually represent various degrees of curvature along the mitochondrial membrane.

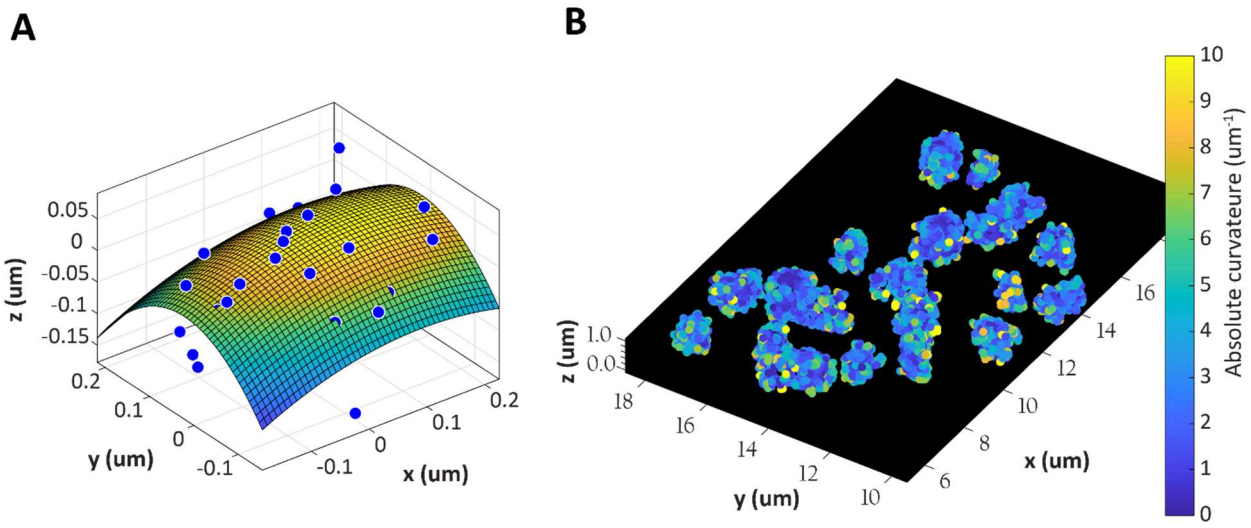

Figure A1. Example of mitochondrial membrane curvature fitting. (A) A sampled region of localized points on the surface of a mitochondrion with the best fit paraboloid surface overlaid. (B) Plotted points from the alpha shapes of super-resolved mitochondria, where each point is mapped to a different color according to the local curvature identified through curve fitting.

Figure A1 A shows an example of local membrane curvature fitting from pTOM20-Dendra2 labeled mitochondria in fixed C2C12 cells. From the local curvature obtained at each location, a map of the magnitude of local curvature can be made throughout the sample (Figure A1 B). Note the variation in curvature over the surface of the mitochondria, as reflected in the changes in color within the image. Based on fitting to simulated data with known curvature and simulated localization precision, we estimate the error in the mean curvature, C_{mean}, to be $\sigma_C \sim \pm 0.25\ \mu m^{-1}$ (see supplement for further details) which will in general depend on the localization uncertainties for molecular coordinates in x, y, and z, as well as on the localization sampling density.[62]

While other work has established methods for measurement of membrane curvature using diffraction-limited microscopy,[129,237] this methodology can employ super-resolution localization microscopy to determine membrane curvature at far smaller length scales than are accessible by conventional fluorescence imaging. Because of the pervasiveness and importance of lipid bilayers in cellular organization, we expect this capability to be useful for a variety of biological applications.

ACKNOWLEDGEMENTS

The authors thank Roger Sher, Greg Cox, and Andrew Nelson for useful discussions, and Patricia Byard for technical assistance. This work was funded by National Institutes of Health grants R01AR054170, R15GM116002 and R15GM094713, by Maine Technology Institute grants MTAF 1106 and 2061, by the University of Maine Office of the Vice President for Research, and by the Maine Economic Improvement Fund.

SUPPLEMENTARY MATERIAL

Cells were cultured using standard media in 5% CO2, passaged once every 3 days, and grown to 80% confluency. Cells were then plated on ibidi μ-Dishes, transfected with pTOM20-Dendra2 plasmids using Lipofectamine 3000 after 24 hours of growth and were then differentiated using serum reduced media (2% horse serum), which was replaced every 24 hours. Once most of the cells differentiated to

myotubes (typically 72-120 hours post-transfection), they were fixed in 4% paraformaldehyde. Fixed cells were then imaged in an FPALM microscope with 1.4 NA 60X oil objective under 561nm widefield illumination (I~3-5 kW/cm^2), with low levels of 405 nm light (~10 W/cm^2) applied as needed for photoactivation. Three-dimensional position was calibrated by imaging fluorescent beads in conjunction with a piezo-controlled axial translator for the objective lens. Axial translations of ~100-1000nm were applied using the piezo controller, and the resulting images were acquired for each objective axial position. The measured bead PSFs were then fitted using a two-dimensional Gaussian with separate widths in X and Y:

$$I = I_0 \exp\left[-\frac{(x-x_0)^2}{r_x^2} - \frac{(y-y_0)^2}{r_y^2}\right] + C$$

The dependencies of r_x and r_y on the objective position were then analyzed and used to create a conversion function for z-position based on the values of r_x and r_y.[68,233]

To test the precision of our method, we simulated a set of points describing a sphere with known curvature and applied our edge detection and curve fitting analysis. Localization precision was accounted for by applying a spatial offset to each coordinate. These offsets were generated using a normally distributed random number generator, with a Gaussian radius of 40 nm for x and y and 80 nm for z, based on our average experimental localization precisions. Using fluctuations from the known curvature values, the estimated error was approximately $\pm$0.25 μm-1 for a sphere of radius 1μm, with a sampling radius of 0.5 μm, and minimum sampling density of 50 molecules/μm^2. However, this error will rapidly increase when the size of the object or the sampling radius approaches the localization precision of the molecules and sets a lower limit on the usefulness of this method.

BIOGRAPHY OF THE AUTHOR

Matthew Parent was born in Waterville, Maine on June 21, 1986. He was raised in China, Maine and graduated from Waterville Senior High School in 2004. He attended University of Maine and graduated with a Bachelor's of Science degree in Physics in 2011. Matthew is a candidate for the Doctor of Philosophy degree in Physics from the University of Maine in May 2020.